WASHINGTON UNIVERSITY IN ST. LOUIS
DEPARTMENT OF PHYSICS

Dissertation Examination Committee:
Kater W. Murch, Chair
Kade Head-Marsden
Erik Henriksen
Yogesh N. Joglekar
Alexander Seidel

Experimental Investigation of Non-Hermiticity in Quantum Systems

by
Maryam Abbasi

A dissertation presented to
Washington University in St. Louis
in partial fulfillment of the
requirements for the degree
of Doctor of Philosophy

St. Louis, Missouri
May, 2023

Table of Contents

List of Figures

Acknowledgements

As one journey draws to a close and another begins, I am filled with immense gratitude for the unwavering support, guidance, and encouragement I have received throughout my graduate studies. This significant milestone would not have been possible without the invaluable contributions of those who have helped me along the way.

First and foremost, I extend my deepest appreciation to my advisor, Kater Murch. His unwavering support, enthusiasm, and insight have been instrumental in shaping my research and academic development. The opportunities he provided have allowed me to thrive and succeed in my field, turning this accomplishment into a reality. Kater truly embodies the qualities of an exceptional mentor.

I am thankful to Erik Henriksen and Alexander Seidel for their indispensable insights and assistance during my studies. A special acknowledgment goes to Yogesh Joglekar, whose dedication to my research significantly contributed to the success of my Ph.D. and opened doors to new opportunities. Learning from him has been a true delight. I also express my gratitude to Kade Head-Marsden for serving on my committee, and eagerly anticipate joining her group for my post-doctoral position. Furthermore, I am grateful to my Master's advisor, Ahmad Ghodsi, for his encouragement and support that made this journey feasible.

The camaraderie and mentorship within the Murch lab have been indispensable. I extend my heartfelt appreciation to my mentor, Mahdi Naghiloo, for his support and guidance. I hold special gratitude for Serra Erdamar, an exceptional friend and colleague with whom I have shared numerous stimulating discussions and engaging challenges. I am also thankful to Weijian Chen for our shared experiences in the lab, filled with captivating challenges and thought-provoking conversations. Furthermore, I treasure the friendships I have forged with my labmates: Daria Kowsari, Chandrashekar Chaiwad, Patrick Harrington, Jonathan Mon-

roe, Xingrui Song, and Zoe Wang. It was a delight working alongside Alexandria Udenkwo, Dian Tan, and Kaiwen Zheng. The enlightening discussions and collaborations with undergraduate students Scott Hershburger, Byung Ha, and Easter Chen have been genuinely rewarding. I am also deeply grateful for the valuable collaboration with Judith Hoeller, who contributed significantly to the theoretical framework and calculations for the Non-Hermitian project outlined in Sec. 4.4. Furthermore, I am grateful for the productive discussion with Jack Harris' Group, whose insight contributed to the progress of our work presented in Ch. 4.

I am eternally indebted to my parents for their love, sacrifices, and mentorship, which have empowered me to pursue my passion for physics abroad. My heartfelt appreciation goes to my sisters, Ladan, for her love and support in the US that filled the void of being far from home, and Golsa, for her unwavering encouragement and love. I am deeply grateful to Jonah Hoffman, whose love, understanding, and patience have been a constant source of strength in this journey.

The Physics Department at Washington University has provided an extraordinary environment for a journey filled with joy, growth, and lifelong friendships. I wholeheartedly thank Yashika Kapoor for her unwavering love and support throughout my Ph.D. journey and a deep friendship I could always rely on. I would also like to express my appreciation to Elham Ghazizade, and Fateme Taherasghari for their warm and encouraging presence. Additionally, I extend special thanks to Andrew West for his friendship, making my journey to the US both welcoming and enjoyable. I would also like to extend my gratitude to all the friends, fellow graduate students, faculty, and staff in the Physics Department at WashU, in particular Professor Mark Alford (Department Chair), Sarah Akin, Mary Sullivan, Shirley McTigue and Sai Iyer, who have contributed to creating a lively, dynamic, and enjoyable atmosphere.

Maryam Abbasi

Washington University in St. Louis

May, 2023

ABSTRACT OF THE DISSERTATION

Experimental Investigation of Non-Hermiticity in Quantum Systems

by

Maryam Abbasi

Doctor of Philosophy in Physics

Washington University in St.Louis, 2023

Professor Kater W. Murch (Chair)

The investigation of quantum systems in experimental setups involves interaction with the environment, which introduces channels of dissipation. These systems can be described by a non-Hermitian Hamiltonian, capturing the effect of gain and loss. Realizing these systems in classical cases demonstrates interesting phenomena such as topological features in the optical and mechanical domain, energy transfer, and enhancement in sensing. The primary focus of this thesis is the realization of the non-Hermiticity in a quantum system. To accomplish this, we harness multiple energy levels of an anharmonic superconducting circuit with coupling to an engineered bath to investigate the static and dynamic features of the system. The static features of our system provide us with detail about the energy landscape and its corresponding eigenstate. The unique energy landscape is investigated further by using a time-dependent drive to study the adiabatic limit. In dissipative dynamics, the role of quantum jumps becomes crucial in studying adiabatic processes. Further study of the non-Hermiticity with decoherence processes exhibits unique topology and energy landscape which will help us understand more complex open quantum systems. These studies provide insight into open quantum system dynamics and how to harness their unique characteristics in a fully quantum regime.

Chapter 1

Open Quantum systems

1.1 Review of key concepts in quantum mechanics

In this section, I provide an overview of the fundamental concepts of quantum mechanics that are essential to the work presented in this thesis. First, I introduce the representation of quantum states on the Bloch sphere, which offers a powerful visual tool for understanding the behavior of qubits. Next, I discuss the density matrix operator and its evolution under unitary transformations for a system coupled to an external environment or bath. This evolution is described by the Kraus representation, which effectively captures the dynamics of the subsystem of interest. Lastly, I outline the derivation of the master equation, and provide an example for clarity. The content in this section is primarily based on references [1, 2, 3], and Qiskit textbook [4], where interested readers can find more in-depth information on these topics.

Let's start by understanding observables and measurements. We can describe any quantum states by some linear combination of the basis states of some observable operator A.

Let's consider a generic state of the form:

$$|\alpha\rangle = \sum_{a'} |a'\rangle\langle a'|\alpha\rangle, \tag{1.1}$$

where $|a'\rangle$ is the eigenstate of the observable A. Born's rule tells us if a measurement takes place, the state $|\alpha\rangle$ will collapse to one of the eigenstates of the observable A. Moreover, we can see from this equation that unless the system is in the eigenstates of the observable, we don't know with certainty what would result from the measurement. However, we can find the probability of collapsing to each eigenstate by calculating the following inner product:

$$P_{a'} = |\langle a'|\alpha\rangle|^2. \tag{1.2}$$

This probability cannot be negative, and the sum over all eigenstates of Eq. 1.2 should be 1. By performing measurements, we can measure the eigenvalues of our observable. So we can define a measurement operator that projects the quantum state on eigenstates of the observable operator. Looking at Eq. 1.1, the outer product $|a'\rangle\langle a'|$ in the sum is the measurement operator on the state $|\alpha\rangle$. So we define our projection operator as:

$$\Lambda_a' = |a'\rangle\langle a'|. \tag{1.3}$$

By applying this operator to any state, we can project the quantum state on the observable's basis and acquire the probabilities. However, we must repeat the same measurement many times to achieve the probabilities. In experimental systems, it is useful to discuss the expectation value of an observable with respect to a given state. In Sec. 1.3, I will discuss the density matrix and observables measured in experimental systems.

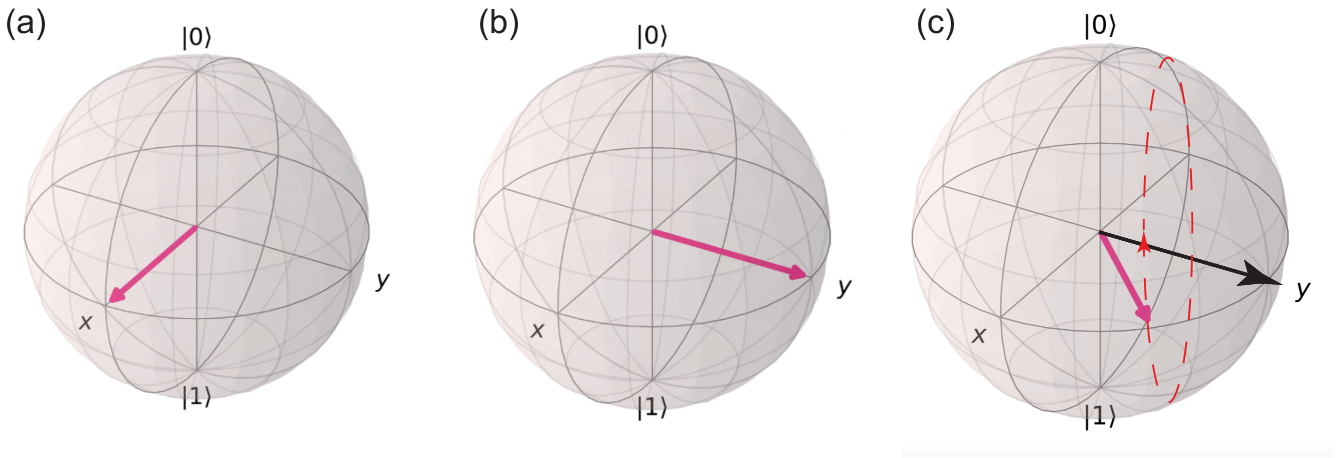

Fig. 1.1: (a) State $|X+\rangle$ on the Bloch sphere. (b) State $|Y-\rangle$ on the Bloch sphere. (c) Evolution of an arbitrary state under a constant drive. Qiskit [4] is used to represent Bloch spheres.

1.2 Bloch sphere representation

In the classical world, information is stored using binary values 0 and 1. Bits are used to represent the objects, data, and any software on classical computers. In the quantum world, however, the concept of bits transforms into quantum states that not only can be in 0 or 1 state but also in an arbitrary superposition of these two values. This concept is a little bit more complicated because what we can measure are still 0s and 1s, but the process these states can undergo is only possible with the rules of quantum mechanics. The operations on qubits in quantum mechanics are completely different, and in order for us to understand these operations, it's useful to have an intuitive visualization of the quantum states.

Let's start by assigning 0's and 1's to the two states of the quantum system:

$$|0\rangle = [0, 1], \ |1\rangle = [1, 0]. \tag{1.4}$$

The measurement outcome of these states are 0 and 1, respectively. Moreover, these two states are orthogonal, meaning they can span the space of any superposition of these two states. The case becomes more interesting when the state of the qubit is a superposition of these two states, which we can write as follows:

$$|\psi\rangle = \alpha|0\rangle + \beta|1\rangle, \tag{1.5}$$

where α and β are some complex number, with constraint $\alpha^2 + \beta^2 = 1$.

The state $|\psi\rangle$ tells us all the information we need to determine the state of a qubit. The measurement output for this case are still 0s and 1s. But α and β can be defined by performing many measurements. After many measurements on these states, we can achieve a probability that tells us the qubit's state. These two values can take a complex value. To describe them, we need at least two parameters—given that the state is a unit vector. Now, the way we want to represent the measured states can be simply understood by using the two angles defining a unit vector on a surface of a sphere. To understand this, first, we need to simplify the state $|\psi\rangle$, we know that $|0\rangle$ and $|1\rangle$ can each be a complex number. However, since we only measure the relative phase between the two, we can assign a phase to one of them. Finally we can change variables and write $\alpha = \sin\theta/2$ and $\beta = \cos\theta/2\exp\{i\phi\}$ – remember that $\alpha^2 + \beta^2 = 1$. Now we can see that these two variables can be the spherical coordinates on a sphere. Let's consider the two cases:

- $|x+\rangle = 1/2(|0\rangle + |1\rangle) \rightarrow \{\theta = \pi/2, \phi = 0\}$,
- $|y-\rangle = 1/2(|0\rangle - i|1\rangle) \rightarrow \{\theta = \pi/2, \phi = \pi/2\}$,

where $|x+\rangle$ and $|y-\rangle$ are the eigenstates of σ_x and σ_y Pauli matrices, respectively. In Fig. 1.1, you can see the representation of these states on Bloch sphere—where Fig. 1.1a is

$|X+\rangle$ and Fig. 1.1b is $|Y-\rangle$. In this section, we have learned that we can represent all qubit states on the Bloch sphere. Moreover, this picture is useful because it can give clear pictures of quantum processes. Let's look at how qubit states evolve under a constant driving Hamiltonian:

$$H = J\sigma_y, \tag{1.6}$$

where J is a real value. An arbitrary state evolving under Eq. 1.6 can be understood by decomposing the state into the σ_y eigenvalues:

$$\psi(t) = a_+ e^{E_+} |y+\rangle + a_- e^{E_-} |y-\rangle, \tag{1.7}$$

where $a_\pm$ are determined by the initial state. In Fig. 1.1c, an arbitrary state is shown that evolves around the Y–axis following the dashed red line. This means that the system goes through oscillation as it revolves around the Y–axis. This is called Rabi oscillation. We can describe the evolution of quantum states on the Bloch sphere, which is a great tool for visualizing quantum systems.

1.3 Density operators

We use density operators to represent an ensemble of quantum states. This ensemble can consist of many quantum systems in a pure state. This is an important concept in experimental quantum systems when we want to describe and measure the state of our qubit. If we perform a measurement on our quantum system at state $|\psi_i\rangle$ and make a measurement with a measurement operator M_i. The resulting measured state wil be $\frac{M_i|\psi_i\rangle}{\langle\psi_i|M_i^\dagger M_i|\psi_i\rangle}$. Based on this, we define an operator that represents the density state:

$$\rho = \sum_i p_i |\psi_i\rangle\langle\psi_i|, \tag{1.8}$$

where p_i is the probability of the state $|\psi_i\rangle$.

The density operator has the following properties:

1. The trace of the density matrix is unity:

   $$\mathrm{Tr}\{\rho\} = 1, \tag{1.9}$$

2. The density operator is Hermitian, guaranteed by the fact that the matrix elements of the density matrix are probabilities that are always positive:

   $$\rho^\dagger = \rho, \tag{1.10}$$

3. The density matrix is positive definite. i.e.

   $$\langle\nu|\rho|\nu\rangle = \sum_i p_i |\langle\psi_i|\nu\rangle|^2 \geq 0, \tag{1.11}$$

   for all states $|\nu\rangle \in \mathcal{H}$.

The density matrix evolution can be obtained using the time-evolution operator. If we write the density matrix in terms of the pure states' time evolution, we have:

$$|\psi_i(t)\rangle = U(t)|\psi_i\rangle \rightarrow \rho(t) = \sum_i p_i |\psi_i(t)\rangle\langle\psi_i(t)| = U(t)\rho(0)U^\dagger(t). \tag{1.12}$$

We can find the result of a measurement on the system by finding the trace of the density operator and the measurement operator as follows:

$$p_i = \mathrm{Tr}\Big[\rho M_i^\dagger M_i\Big], \tag{1.13}$$

and the expectation value of an observable A in the density operator picture would be $\langle A\rangle = \mathrm{Tr}(\rho A)$.

Moreover, we can simply use our density operator's matrix elements to visualize the state on the Bloch sphere:

$$\rho = \frac{1}{2}\begin{pmatrix} 1+v_z & v_x - iv_y \\ v_x + iv_y & 1 - v_z \end{pmatrix}., \tag{1.14}$$

where v_x, v_y and v_z are the expectation values of the Pauli matrices and determine the location of the qubit state on the Bloch sphere. The magnitude of the Bloch sphere is related to the purity of the state. For example, if the density state is $\rho = I/2$, the Bloch vector is at the center, which is a maximally mixed state.

1.4 System and a bath

A quantum system coupled to a bath is a critical topic to study due to the role of the bath in the dynamics of experimental quantum systems. The bath can be designed to give us desired dynamics for the quantum systems. An example of this is the study of non-Markovianity and non-Hermiticity. There has been significant research on studying quantum heat engines by engineering the bath coupled to the qubit. Depending on the experiment, the bath can comprise the transmission lines, the entire lab, and many degrees of freedom of the environment. These couplings to the quantum systems are generally detrimental in nature and result in decoherence. However, we can also harness them by carefully engineering the density of states of the bath.

Let's consider a system A coupled with a bath B and the evolution of the combined system can be described by a unitary evolution e^{-iHt}. The combined system can be described by the direct product of both system's Hilbert space:

$$\mathcal{H} = \mathcal{H}_A \otimes \mathcal{H}_B. \tag{1.15}$$

Because the system of interest is A, we trace out the bath degrees of freedom. The partial trace on the bath will map the Hilbert space to the Hilbert space of A ($\mathcal{H} \rightarrow \mathcal{H}_A$):

$$\rho_A = \mathrm{Tr}_B[\rho] = \sum_{\mu} = \langle\mu|U(t)\rho(0)U^\dagger(t)|\mu\rangle, \tag{1.16}$$

where the trace is taken over the orthogonal basis of the bath $|\mu\rangle$ and $U(t)$ is the unitary time evolution operator of the combined system. Now if we assume that the initial states are decoupled:

$$\rho(0) = \rho(0)_A \otimes \rho(0)_B. \tag{1.17}$$

Then the system evolution can be written in terms of the time operator of the combined system:

$$\rho_A(t) = \sum_{\mu\nu} K(t)_{\mu\nu}\rho_A(0)K^\dagger(t)_{\mu\nu}, \tag{1.18}$$

where $K(t)_{\mu\nu}$ is the Kraus operator defined as:

$$K(t)_{\mu\nu} = \sqrt{\lambda_\nu}\langle\mu|U(t)|\nu\rangle. \tag{1.19}$$

Here $U(t)$ is the time evolution operator of the combined system and the bath. We can replace $\mu\nu$ subscript into one α and reach the $K_\alpha(t)$ Kraus operator representation. This is explained further in the examples below.

1.4.1 Amplitude damping

The decay process from the excited state to the ground state of a quantum system by spontaneously emitting a photon is amplitude damping. Let's consider an excited state $|1\rangle_S$ and ground state $|0\rangle_S$ of an atom coupled to an electromagnetic field. The system will decay into the environment with some probability p by emitting a photon after a while. Then we have:

$$|1\rangle_S |0\rangle_E \rightarrow \sqrt{p}\, |0\rangle_S |1\rangle_E + \sqrt{1-p}\, |1\rangle_S |0\rangle_E . \tag{1.20}$$

By tracing over the environment, the Kraus operator will be:

$$K_0 = \langle 0| U_{SE} |0\rangle = \begin{pmatrix} 1 & 0 \\ 0 & \sqrt{1-p} \end{pmatrix}, \; K_1 = \langle 1| U_{SE} |0\rangle = \begin{pmatrix} 0 & \sqrt{p} \\ 0 & 0 \end{pmatrix}, \tag{1.21}$$

where K_0 is the evolution with no quantum jump and K_1 represents the quantum jump from $|1\rangle_S$ to $|0\rangle_S$. Then the evolution of the system can be described by:

$$\rho_S(t) = K_0 \rho_S(0) K_0^\dagger + K_1 \rho_S(0) K_1^\dagger = \begin{pmatrix} \rho_{00} + p\rho_{11} & \sqrt{1-p}\rho_{01} \\ \sqrt{1-p}\rho_{10} & (1-p)\rho_{11} \end{pmatrix}. \tag{1.22}$$

If we apply this operator n times in time, $\rho_{11} \rightarrow \rho_{11}(1-p)^n$, where $p = \Gamma t$, which results in exponential damping $\rho_{11} \rightarrow \rho_{11}(1-p)^n = \rho_{11}(1-\Gamma\delta t)^n \approx \rho_{11} e^{-\Gamma t}$. The off-diagonal elements will vanish in the same way. So the final result is:

$$\rho_S(t) = K_0 \rho_S(0) K_0^\dagger + K_1 \rho_S(0) K_1^\dagger = \begin{pmatrix} \rho_{00} + \rho_{11} & 0 \\ 0 & 0 \end{pmatrix}. \tag{1.23}$$

1.4.2 Phase damping

If our system interacts with small parts of the environment weakly, then the state of the system does not change but it is likely that it undergoes some change due to the presence of many of these interactions, which in turn changes something about the environment subsystem but not our system's state. To represent this behavior, let's consider a case where a photon interacts with a system [3]. The system can be either in the ground or first excited state. If the photon interacts with this system but doesn't change the system state, it will only go to its first or second excited state as a result of this collision. So we represent this change in the environment as follows:

$$|0\rangle_S |0\rangle_E \rightarrow \sqrt{1-p}\,|0\rangle_S |0\rangle_E + \sqrt{p}\,|0\rangle_S |1\rangle_E \,, \tag{1.24}$$

$$|1\rangle_S |0\rangle_E \rightarrow \sqrt{p}\,|1\rangle_S |0\rangle_E + \sqrt{1-p}\,|1\rangle_S |2\rangle_E \,. \tag{1.25}$$

With regard to the above equation, a possible unitary is:

$$U = \begin{pmatrix} \sqrt{1-p} & \sqrt{p} & 0 & 0 & 0 & 0 \\ \sqrt{p} & \sqrt{1-p} & 0 & 0 & 0 & 0 \\ 0 & 0 & 1 & 0 & 0 & 0 \\ 0 & 0 & 0 & \sqrt{1-p} & 0 & \sqrt{p} \\ 0 & 0 & 0 & 0 & 1 & 0 \\ 0 & 0 & 0 & \sqrt{p} & 0 & \sqrt{1-p} \end{pmatrix} \tag{1.26}$$

where the basis is $\{\left|0\right\rangle_S \left|0\right\rangle_E, \left|1\right\rangle_S \left|0\right\rangle_E, \left|2\right\rangle_S \left|0\right\rangle_E, \left|0\right\rangle_S \left|1\right\rangle_E, \left|1\right\rangle_S \left|1\right\rangle_E, \left|1\right\rangle_S \left|2\right\rangle_E\}$. The Kraus operator is given by partial trace of U over the environment state:

$$K_0 = \left\langle 0\right| U \left|0\right\rangle = \sqrt{1-p}\mathrm{I},\ K_1 = \left\langle 1\right| U \left|0\right\rangle = \sqrt{p}\left|0\right\rangle\left\langle 0\right|,\ K_2 = \left\langle 2\right| U \left|0\right\rangle = \sqrt{p}\left|1\right\rangle\left\langle 1\right|, \tag{1.27}$$

which gives the system's evolution:

$$\rho_S(t) = \begin{pmatrix} \rho_{00} & \sqrt{1-p}\rho_{01} \\ \sqrt{1-p}\rho_{10} & \rho_{11} \end{pmatrix}, \tag{1.28}$$

when this happens n times over the evolution with the rate Γ_2, the density matrix becomes:

$$\rho_S(t) = \begin{pmatrix} \rho_{00} & e^{-\Gamma_2 t}\rho_{01} \\ e^{-\Gamma_2 t}\rho_{10} & \rho_{11} \end{pmatrix}, \tag{1.29}$$

and at long time, the phase coherence is lost:

$$\rho_S(t) = \begin{pmatrix} \rho_{00} & 0 \\ 0 & \rho_{11} \end{pmatrix}. \tag{1.30}$$

1.5 Master equation

Since we want to characterize the dynamics of the system as it evolves in time in infinitesimal steps, we need a tool that allows us to describe the system's behavior in the form of a differential equation in the presence of decoherence. In this section, I introduce the master equations that describe the dynamics of open quantum systems in a differential form. I will focus on the master equation formalism which is Markovian. First, the Liouville master equation is introduced, and then I will derive the Lindblad master equation using the Liouville equation.

1.5.1 Liouville Master equation

For a closed system with state vector $|\psi_i\rangle$, time evolution according to the Schrödinger equation is:

$$i\frac{d}{dt}\left|\psi(t)\right\rangle = H(t)\left|\psi(t)\right\rangle. \tag{1.31}$$

The solution to the Eq. 1.31 can be written in terms of the unitary time-evolution $U(t, t_0)$:

$$\left|\psi(t)\right\rangle = U(t, t_0)\left|\psi(t_0)\right\rangle, \tag{1.32}$$

where we can show that $U(t, t_0)U^\dagger(t, t_0) = U^\dagger(t, t_0)U(t, t_0) = I$. For a closed, isolated system, the form of the time-evolution operator is independent of time, and we have:

$$U(t, t_0) = e^{-iH(t-t_0)}, \tag{1.33}$$

while the presence of some external drive makes the Hamiltonian time-dependent, and $U(t, t_0)$ will be in the following form:

$$U(t, t_0) = \mathcal{T} e^{-i \int_{t_0}^{t} H(t')dt'}, \tag{1.34}$$

where $\mathcal{T}$ is the time-ordered operator which takes into account the order of the product in the increasing order.

When the system is not closed and isolated, the state can be a mixed state, and the density operator is used to describe the state:

$$\rho(t_0) = \sum_i P_i \left|\psi_i(t_0)\right\rangle \left\langle\psi_i(t_0)\right|, \tag{1.35}$$

where $|\psi(t_0)\rangle$ evolves under Shrödinger equation. The evolution of the density operator can then be written in terms of $|\psi(t_0)\rangle \langle\psi(t_0)|$ evolution:

$$\rho(t) = U(t, t_0)\rho(t_0)U^{\dagger}(t, t_0), \tag{1.36}$$

and the time derivative of this Eq. 1.36, gives the equation of motion for $\rho(t)$:

$$\frac{d}{dt}\rho(t) = -i[H(t), \rho(t)]. \tag{1.37}$$

This Eq.1.37 is known as Liouville-von Neumann equation. This equation is written in the following form to emphasize its analogy to the Liouville equation in classical statistical mechanics:

$$\frac{d}{dt}\rho(t) = \mathcal{L}(t)\rho(t), \tag{1.38}$$

where the i is absorbed into $\mathcal{L}$. $\mathcal{L}$ is the Liouville super-operator—where the word "superoperator" is chosen to emphasize its action on another operator rather than a state vector. The solution to Eq. 1.38 can be written as:

$$\rho(t) = e^{\int_{t_0}^{t} \mathcal{L}(t')dt'} \rho(t_0). \tag{1.39}$$

Now, to understand the dynamics of open quantum system, we start by writing the Hamiltonian of the system and a bath:

$$H(t) = H_S \otimes I_B + I_S \otimes H_B + H_I(t), \tag{1.40}$$

where H_B and H_S are the bath and the system Hamiltonian and $H_I(t)$ is the interaction Hamiltonian. The bath or reservoir typically has many degrees of freedom, which form a continuum and result in irreversible dynamics of open quantum systems. The presence of many degrees of freedom coupled to a system makes the solution to the system's evolution difficult, especially if these degrees of freedom are unknown—which is true for most reservoirs. So we try to find solutions by finding descriptions that restrict the dynamics to relevant variables. The desired dynamics is the reduced density matrix of the system $\rho_S = \mathrm{Tr}_B\, \rho$. So we want to use the total evolution dynamics:

$$\rho(0) = \rho_S(0) \otimes \rho_B \xrightarrow{\textbf{time evolution}} \rho(t) = U(t, t_0)\rho_S(0) \otimes \rho_B U^\dagger(t, t_0), \tag{1.41}$$

into the following form for the desired part of the system:

$$\rho_S(t) = \mathrm{Tr}_B\{U(t, t_0)\rho_{t_0} U^\dagger(t, t_0)\} \equiv V(t)\rho_S(0), \tag{1.42}$$

where $V(t)$ defines a map of the space of the reduced density matrix to itself. If we write the bath degree of freedom in terms of its basis in the following spectral decomposition form:

$$\rho_B = \sum_{\alpha} \lambda_\alpha \left|\psi_\alpha\right\rangle \left\langle\psi_\alpha\right| . \tag{1.43}$$

We can see that Eq. 1.42 takes the form:

$$V(t)\rho_S = \sum_{\alpha,\beta} W_{\alpha,\beta}(t)\rho_S W^{\dagger}_{\alpha,\beta}(t), \tag{1.44}$$

where:

$$W_{\alpha,\beta}(t) = \sqrt{\lambda_\beta} \left\langle\psi_\alpha\right| U(t,0) \left|\psi_\beta\right\rangle , \tag{1.45}$$

describes a generalized quantum measurement in Eq. 1.18—a Kraus operator. $V(t)$ is a completely positive and trace-preserving quantum operation. If the reservoir correlation function decays much faster than the system evolution time, then we can ignore the effect of memory. This category of systems are Markovian and can be formalized as follows:

$$V(t_1)V(t_2) = V(t_1 + t_2), \quad t_1, t_2 \geq 0. \tag{1.46}$$

So we will investigate a semigroup with the property in Eq. 1.46. The generator for this semigroup can be written as:

$$V(t) = e^{\mathcal{L}t}, \tag{1.47}$$

with reduced density matrix of the form:

$$\frac{d}{dt}\rho_S(t) = \mathcal{L}\rho_S(t), \tag{1.48}$$

which is the Liouville super-operator. We can show that the most general form of this generator $\mathcal{L}$ can be constructed in the following form:

$$\mathcal{L}\rho_S = -i[H, \rho_S] + \sum_{k=1}^{N^2-1} \gamma_k (A_k \rho_S A_k^\dagger - \frac{1}{2} A_k^\dagger A_k \rho_S - \frac{1}{2} \rho_S A_k^\dagger A_k), \tag{1.49}$$

where the first term in this equation is the unitary evolution. Operators A_k are constructed by the Liouville basis operators F_i, where:

$$(F_i, F_j) \equiv \mathrm{Tr}_S\{F_i^\dagger F_j\} = \delta_{ij}, \tag{1.50}$$

which are the complete orthonormal basis of Liouville space of complex N^2 dimensions. This basis defines the action of the dynamical map $V(t)$:

$$V(t)\rho_S = \sum_{i,j=1}^{N^2} c_{ij}(t) F_i \rho_S F_j^\dagger. \tag{1.51}$$

Where c_{ij} is the coefficient matrix. The detailed derivation of Eq.1.49 can be found in [1]. Operators A_k are referred to as Lindblad operators, which correspond to the different channels of dissipations to the environment with the rates γ_k. We can introduce dissipators with this form:

$$\mathcal{D}(\rho_S) \equiv \sum_{k=1}^{N^2-1} \gamma_k (A_k \rho_S A_k^\dagger - \frac{1}{2} A_k^\dagger A_k \rho_S - \frac{1}{2} \rho_S A_k^\dagger A_k), \tag{1.52}$$

and write down the Lindblad equation in terms of the dissipators for convenience:

$$\frac{d}{dt}\rho_S(t) = -i[H, \rho_S] + \mathcal{D}(\rho_S(t)). \tag{1.53}$$

1.5.1.1 An example

To understand the terms in Eq. 1.53, we can consider a case that will be used in future chapters of this thesis. Here, we want to acquire the dynamics of a superconducting circuit with three energy levels $|g\rangle$, $|e\rangle$ and $|f\rangle$ with a coupling rate J and frequency detuning Δ between the $|e\rangle$–$|f\rangle$ transition. The Hamiltonian is described with the following form:

$$H = \begin{pmatrix} 0 & 0 & 0 \\ 0 & \Delta & J \\ 0 & J & 0 \end{pmatrix}, \tag{1.54}$$

since this is a circuit inside a cavity and is coupled to a Markovian bath, there is coupling to the environment and as a result, dissipation channels. These are the relaxation rates from $|e\rangle$ to $|g\rangle$ and from $|f\rangle$ to $|e\rangle$ shown with γ_e and γ_f. The corresponding Lindblad operators are $\mathcal{L}_e = \sqrt{\gamma_e}\,|g\rangle\langle e|$ and $\mathcal{L}_f = \sqrt{\gamma_f}\,|e\rangle\langle f|$:

$$\mathcal{L}_e = \begin{pmatrix} 0 & \sqrt{\gamma_e} & 0 \\ 0 & 0 & 0 \\ 0 & 0 & 0 \end{pmatrix}, \tag{1.55}$$

$$\mathcal{L}_f = \begin{pmatrix} 0 & 0 & 0 \\ 0 & 0 & \sqrt{\gamma_f} \\ 0 & 0 & 0 \end{pmatrix}, \tag{1.56}$$

There is also dephasing associated with these transitions with the Lindblad operators:

$$\mathcal{L}_{2e} = \begin{pmatrix} 0 & 0 & 0 \\ 0 & \sqrt{\gamma_{2e}/2} & 0 \\ 0 & 0 & 0 \end{pmatrix}, \tag{1.57}$$

$$\mathcal{L}_{2f} = \begin{pmatrix} 0 & 0 & 0 \\ 0 & 0 & 0 \\ 0 & 0 & \sqrt{\gamma_{2f}/2} \end{pmatrix}, \tag{1.58}$$

where γ_{2e} and γ_{2f} are dephasing rates. Now, the master equation we want to solve gets the following form:

$$\begin{aligned} \frac{d}{dt}\rho(t) = -i[H, \rho(t)] + \gamma_e(\mathcal{L}_e \rho \mathcal{L}_e^\dagger - \frac{1}{2}\mathcal{L}_e^\dagger \mathcal{L}_e \rho - \frac{1}{2}\rho \mathcal{L}_e^\dagger \mathcal{L}_e) + \\ \gamma_f(\mathcal{L}_f \rho \mathcal{L}_f^\dagger - \frac{1}{2}\mathcal{L}_f^\dagger \mathcal{L}_f \rho - \frac{1}{2}\rho \mathcal{L}_f^\dagger \mathcal{L}_f) + \\ \gamma_{2e}/2(\mathcal{L}_{2e} \rho \mathcal{L}_{2e}^\dagger - \frac{1}{2}\mathcal{L}_{2e}^\dagger \mathcal{L}_{2e} \rho - \frac{1}{2}\rho \mathcal{L}_{2e}^\dagger \mathcal{L}_{2e}) + \\ \gamma_{2f}/2(\mathcal{L}_{2f} \rho \mathcal{L}_{2f}^\dagger - \frac{1}{2}\mathcal{L}_{2f}^\dagger \mathcal{L}_{2f} \rho - \frac{1}{2}\rho \mathcal{L}_{2f}^\dagger \mathcal{L}_{2f}) \end{aligned} \tag{1.59}$$

Chapter 2

Parity-Time symmetry

2.1 Basics of PT-symmetry

The field of PT-symmetry originated with a seminal paper by Bender in 1998 [5], which introduced a unique type of non-Hermitian system characterized by real spectra. In subsequent years there have been considerable experimental efforts towards realizing PT-symmetric systems [6, 7, 8, 9, 10, 11, 12]. In this section, I provide the fundamental concepts of PT-symmetry to understand the core of this thesis. This chapter follows the book on PT-symmetry [13]—this book offers an excellent resource for further understanding of this topic.

Quantum systems can be classified as either closed or open quantum systems. Closed systems are described by Hermitian Hamiltonians with real eigenvalues and unitary time evolution. The norm of the state or probability is conserved for these systems. These systems do not interact with the external environment which makes them impossible to be observed in the experimental setting where measurement is applied. The experimental setups are quantum systems that interact with the environment and are open quantum systems. In the case of open quantum systems, we have a flow of probability, and the system is not in equilibrium, Fig. 2.1a.

It should be noted that, in the field of superconducting circuits, dispersive approximation

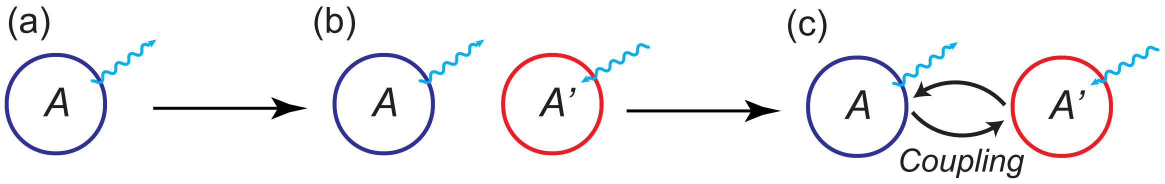

Fig. 2.1: (a) A system with loss. (b) A PT-symmetric version of panel (a) by adding a time-reverse copy of the original. (c) Coupling added to the panel (b) case.

is commonly employed. This approximation emerges due to the significant detuning of frequencies between the system (i.e., the qubit) and its interacting environment (i.e., the cavity), leading to a relatively weak interaction. As a consequence, the qubit and the cavity do not directly exchange energy. Instead, this minimal interaction merely induces a slight shift in the cavity frequency.

However, there is a way to construct a non-isolated system that does not have a flow of probability in and out of the system. This can be done by adding a copy of the system with the opposite flow of probability, Fig. 2.1b. The second part is the time reversal of the original copy. If the original has a loss, the second part has a gain. The two parts together have zero flow of probability in or out of the system. This system has a symmetry called parity-time (PT)-symmetry because if we reverse the time $\mathcal{T}$ in this system, then gain and loss parts will reverse, which reverses the parity $\mathcal{P}$ of the system.

The system is still different from a closed system because it is not in equilibrium, where one part's probability increases and the other decreases. However, by coupling the two parts, they can exchange probability, Fig. 2.1c. If the dynamics is at equilibrium after the coupling, then the system is in the PT-symmetric phase. The system is in the broken PT-symmetric phase when this equilibrium is not acquired after introducing the coupling. The PT-symmetric phase is similar to closed systems, while the broken PT-symmetric phase is similar to open quantum systems. The transition from equilibrium to non-equilibrium is an abrupt point with a certain value of the coupling rate. This transition is known as the PT phase transition.

Let's look at an example of a PT-symmetric system. The system is a simple physical system described by the following Hamiltonian:

$$H = [a + ib], \tag{2.1}$$

with real a and b. This represents a single state with energy $a + ib$. Solving the Schrödinger equation for this Hamiltonian gives the following solution:

$$\psi(t) = Ce^{(-ai+b)t}. \tag{2.2}$$

This system is non-Hermitian for $b \neq 0$, and probability grows or decreases with time:

$$P = \psi^\dagger \psi = |C|^2 e^{2bt}. \tag{2.3}$$

This system is an open system with the flow of probability. Now, we can add a copy of this system by applying the time reversal operator which is by converting i to $-i$. So the second system will be:

$$H' = \mathcal{T} H \mathcal{T}^{-1} = [a - ib], \tag{2.4}$$

with the Schrödinger solution $\psi(t) = Ce^{(-ai-b)t}$. Here the probability is:

$$P' = \psi^\dagger \psi = |C|^2 e^{-2bt}. \tag{2.5}$$

Now the composite system can be described by the following Hamiltonian:

$$H_{Interaction} = \begin{pmatrix} a+ib & 0 \\ 0 & a-ib \end{pmatrix}. \tag{2.6}$$

The parity operator for this system is:

$$\mathcal{P} = \begin{pmatrix} 0 & 1 \\ 1 & 0 \end{pmatrix}, \tag{2.7}$$

which exchanges the two parts. We can show that this Hamiltonian is symmetric under the combined operation of $\mathcal{T}$ and $\mathcal{P}$:

$$\mathcal{PT}H_{\text{interaction}}(\mathcal{PT})^{-1} = H_{\text{interaction}}. \tag{2.8}$$

Now we couple the two parts to allow the system to achieve the equilibrium:

$$H_{interaction} = \begin{pmatrix} a+ib & g \\ g & a-ib \end{pmatrix}, \tag{2.9}$$

where g is the coupling rate. This Hamiltonian is PT-symmetric but not Hermitian. However, this system can have real energies if g is larger than a certain value. The eigenvalues of this Hamiltonian are:

$$E_{\pm} = a \pm \sqrt{g^2 - b^2}. \tag{2.10}$$

For $g^2 > b^2$, the combined system is at equilibrium and in the unbroken PT-symmetric phase, while for $g^2 < b^2$, the system is in the broken PT-symmetric phase. The eigenvalues of this system is shown in Fig. 2.2, where the dashed lines are real and solid lines are imaginary

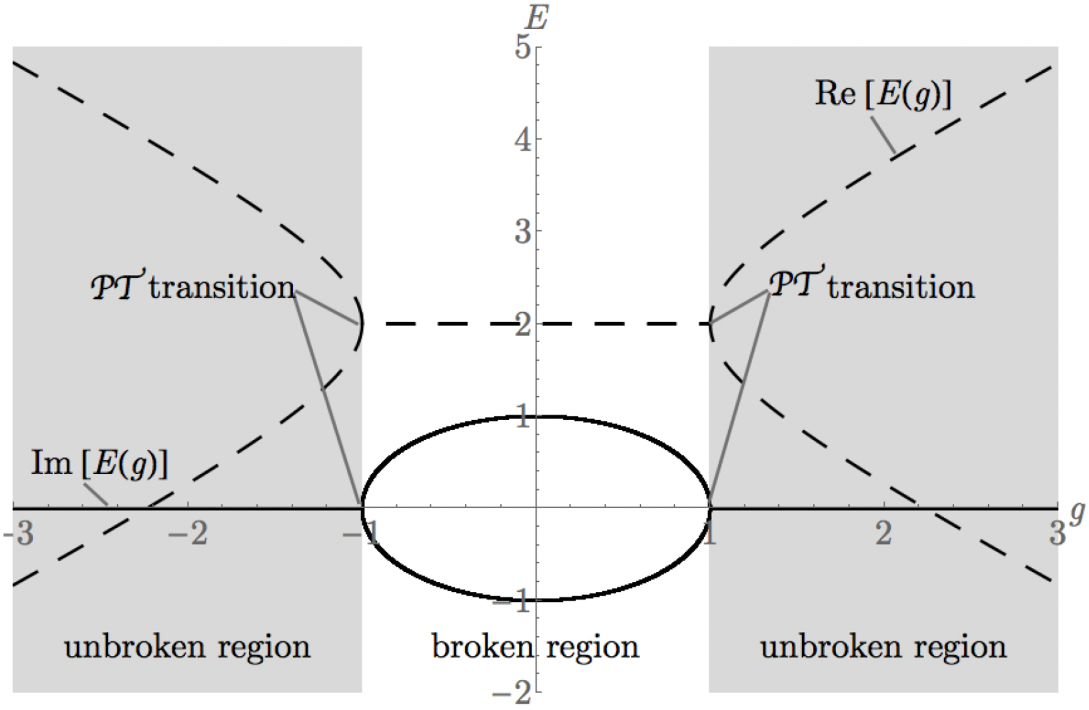

Fig. 2.2: The eigenvalues of the Hamiltonian in Eq. 2.11, for $a = 2$ and $b = 1$ as a function of g. The dashed lines are the real parts, and the solid lines are the imaginary parts. Figure from the book in reference [13].

parts of the eigenvalues. We can see that the transition occurs at $g = \pm b$ where the real eigenvalues coalesce at this point and become imaginary for $g^2 < b^2$.

2.1.1 Complex number theory and PT-symmetry

There is a connection between the complex number theory and PT-symmetry. Typically, the PT-symmetric systems have imaginary eigenvalues, i.e., if we consider a Hermitian system where b (in Eq. 2.11) is zero, then if we change the Hamiltonian by allowing b to be nonzero in the complex domain, then the system is not Hermitian anymore. In this section, we investigate the relation between complex number theory and PT-symmetric Hamiltonians.

Historically, Complex numbers have had an important role in understanding real equations. For example, equations that do not have roots in the real spectrum have roots in the complex domain—the equation $x^4 + 1 = 0$ is an example of complex roots: $e^{\pm\pi/4}, e^{\pm 3\pi/4}$. Finding the roots of these equations helped us understand the functions that had singularities in their denominators in the complex domains.

In order to explore the complex analysis of the PT-symmetric system, let's start with a two-dimensional Hermitian matrix:

$$H = \begin{pmatrix} a & g \\ g & b \end{pmatrix}. \tag{2.11}$$

This is a Hamiltonian of a coupled system with eigenvalues of each part being a and b in the absence of coupling. The secular equation of this Hamiltonian is:

$$0 = \det(H - IE) = E^2 - (a+b)E + ab - g^2 \tag{2.12}$$

, and the eigenvalues are:

$$E_{\pm}(g) = \frac{1}{2}a + \frac{1}{2}b \pm \frac{1}{2}\sqrt{(a-b)^2 + g^2}. \tag{2.13}$$

There is no degeneracy in the real domain. Let's take $a = 1$ and $b = 2$:

$$E_{\pm}(g) = \frac{3}{2} + \pm\frac{1}{2}\sqrt{1 + g^2}. \tag{2.14}$$

At $g = \pm i$, $E_{\pm}(g)$ has square root branch points in the complex domain. This point is called an exceptional point, where the eigenvalues typically coalesce. In this case, two eigenvalues merge, making the branch point an order two degeneracy. By extending this eigenvalue problem to the complex domain, we gain insight into the quantization of energy. That means

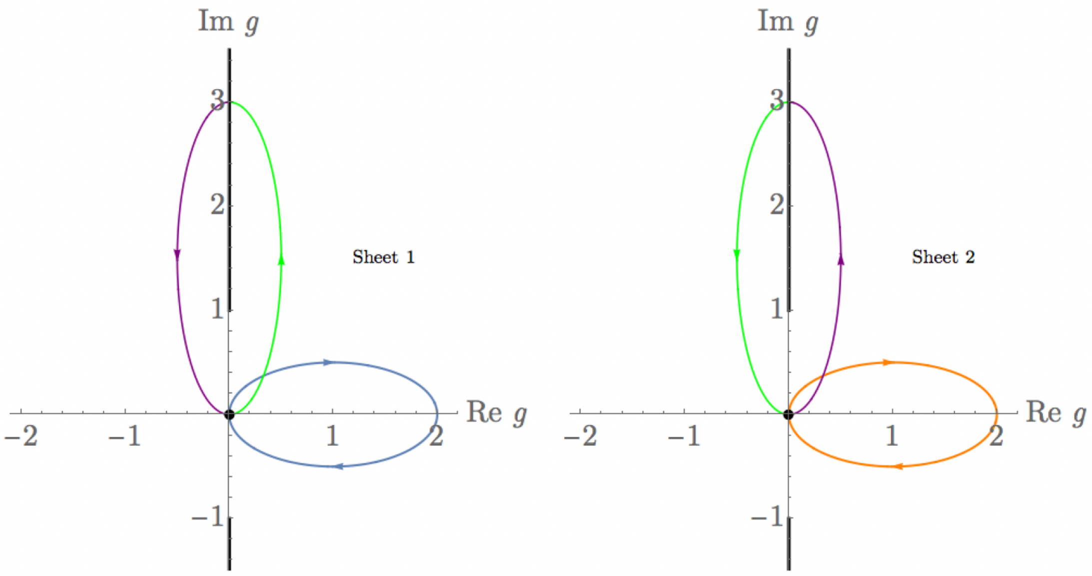

Fig. 2.3: Orange and blue paths are closed loops that do not encircle the exceptional point. While green and purple paths encircle the exceptional point and result in the exchange of identity of the two eigenvalues. Figure is from reference [13]

the function $E(g) = \frac{3}{2} + \frac{1}{2}\sqrt{1+g^2}$ is, in fact, continuous in complex energy as a function of g. The two eigenvalues are continuously connected through a two-sheeted Riemann surface, Fig. 2.3. Moreover, the quantization has a topological interpretation, which can be understood by considering a closed path with or without the exceptional point, Fig. 2.3. As it's shown in Fig. 2.3, for the closed path that does not encircle the exceptional point, the energy spectrum also follows a closed path and returns to itself. However, if we encircle an exceptional point at the branch cut, the two energies exchange their identities, which is because in the complex domain they are the analytical continuation of each other.

The experimental realization of PT-symmetric systems can lead to unique phenomena in different platforms such as electrical systems [7, 14], optical systems [7, 9, 15, 16, 17, 18], and mechanical systems [19]. It is important to note that achieving a balanced gain and loss is not the sole criterion for realizing PT-symmetry. In fact, there has been research involving systems with overall loss [6, 10, 20, 12], where, for example, one channel is lossless while the other experiences loss. These systems are known as passive systems and they are related to PT-symmetric case with a gauge transformation. The following chapter will explore the experimental realization of PT-symmetric systems.

Chapter 3

Experimental probes of non-Hermitian systems

3.1 Classical examples

3.1.1 Mechanics

Carl Bender, a founder of theoretical Parity-Time symmetry, and his team demonstrated PT-symmetry in a simple experiment using two pendula [19], Fig. 3.1a. Two pendula are coupled via a horizontal rope, while each of them are hanging from the ceiling. There is an electromagnet for each pendulum that is turned on for a short time to add or subtract energy depending on when the magnet is applied. To ensure that the electromagnet is applied properly, the experiment uses an optical sensor that monitors the pendula. Finally, they record the displacements of the pendula, which are labeled as x and y for each oscillator. They perform the experiment for three different cases:

- The electromagnet is off, so we observe Rabi power oscillation, Fig. 3.1b. The exchange of energy between the pendula corresponds to PT-symmetry unbroken region.

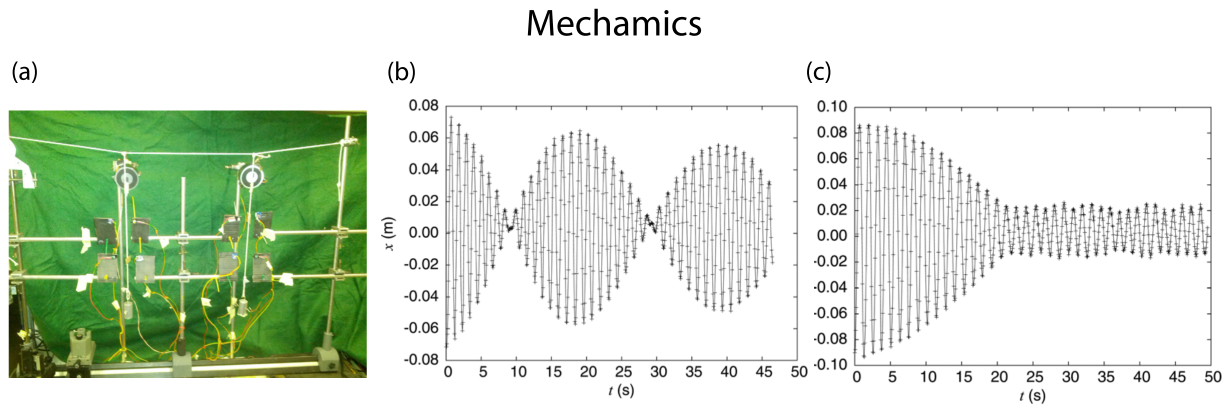

Fig. 3.1: Mechanics: (a) The experimental setup comprises two pendula coupled by a horizontal string with adjustable weight to change the coupling. There is electromagnet to apply field on an iron nail on top of each pendula pulley and sensors to monitor the motion of the pendula. Oscillation of pendulum x when, (b) Electromagnet is off. (c) Electromagnet is strongly turned on and the mass on the coupling string is increased. Figure from [19].

- When the electromagnet is on, and coupling is weakened by increasing the mass on the horizontal string. We observe the oscillation has disappeared and we are at the PT-symmetry broken region Fig. 3.1c.

3.1.2 Optomechanics

This section gives a summary of the work done on an optomechanical system [21], which is a silicon nitride membrane inside an optical cavity. Two vibrational modes of this membrane which are nearly degenerate are chosen to demonstrate PT-symmetric phenomena, Fig. 3.2a. When the two modes are driven by a laser light, the coupling rates introduced to the system create an effective PT-symmetric Hamiltonian. The power P and the frequency Ω_L of the laser light that drives these modes can be varied to realize energy transfer between the two modes. The system undergoes a change in two parameters of this system in a closed loop to demonstrate the asymmetric mode switch and energy transfer between the two modes.

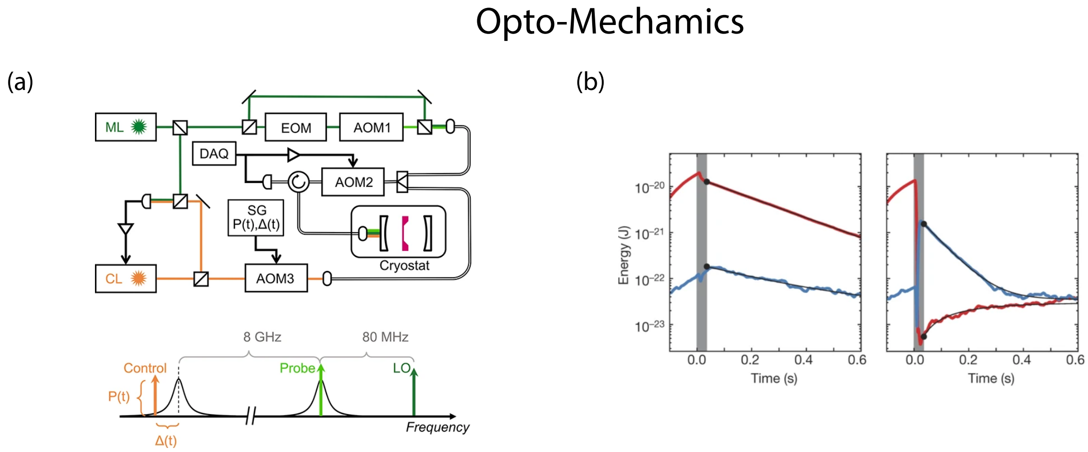

Fig. 3.2: Optomechanics: (a) Optomechanical setup including the membrane, lasers, splitters and etc. (b) The amplitude of the two modes $|c_{a,b}|$, when the EP is not encircled (left) and encircled (right). The grey area is when the closed parameter loop is implemented. Figure from [21].

When comparing the amplitude of the motion of the normal modes $|c_a|$ and $|c_b|$, before and after the control loop, two situation was observed:

- If the control loop does not encircle the exceptional point, 99% of the energy stays in the initial mode c_a, Fig. 3.2b (left).
- If the loop encircles the exceptional point the energy transfers from mode a to mode b, shown in Fig. 3.2b (right), where 99% of the energy is in mode a before starting the loop and 99% of energy is in mode b after the loop.

3.1.3 Optics

There are many instances of the realization of PT-symmetry in optical setup, typically these were achieved by controlling the main ingredient of the optical setups, refractive index — hence the imaginary part can be gain or loss. Here I explain a summary of the paper [14] that realizes PT-symmetry in temporal domain in an optical network shown in Fig. 3.3a.

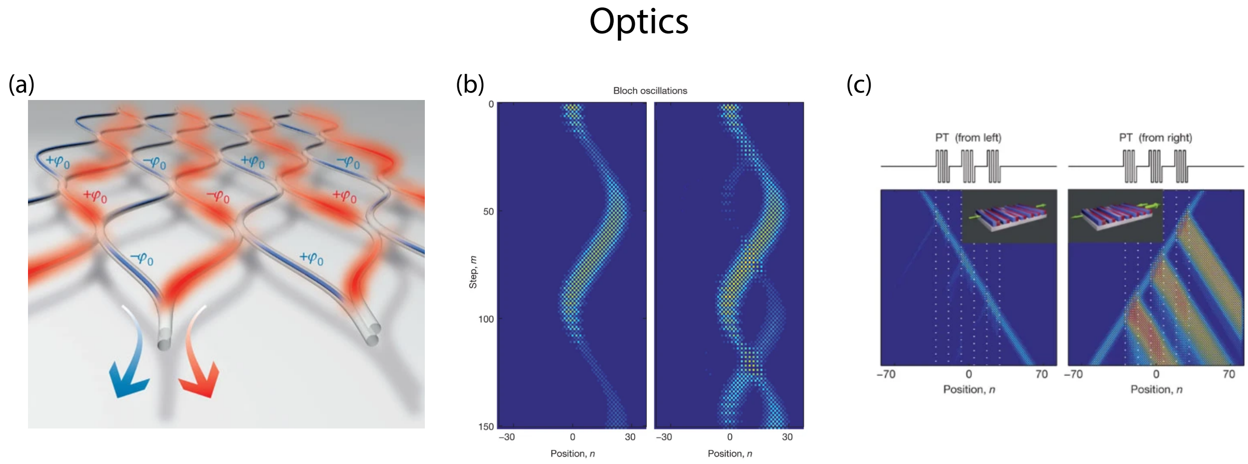

Fig. 3.3: Optics: (a) schematics of the optical fibre. (b) Emission of a secondary wave. (c) Unidirectional light scattering. Figure from [14].

They shape laser pulses through fibre loops connected by a coupler. The resulted interfered pulses acquire different phases. The PT-symmetry arises in this system by introducing optical amplifiers and amplitude modulators. In this setup, they observed the emission of a secondary beam, every time the eigenvalues are imaginary, Fig. 3.3b. Moreover, the unidirectional light scattering was observed in this system by imposing periodic phase modulation $\phi(n)$ that creates a temporal Bragg scatterer. The incident light in one direction does not experience reflection while in the opposite direction, the reflection coefficient is bigger than one, Fig. 3.3c.

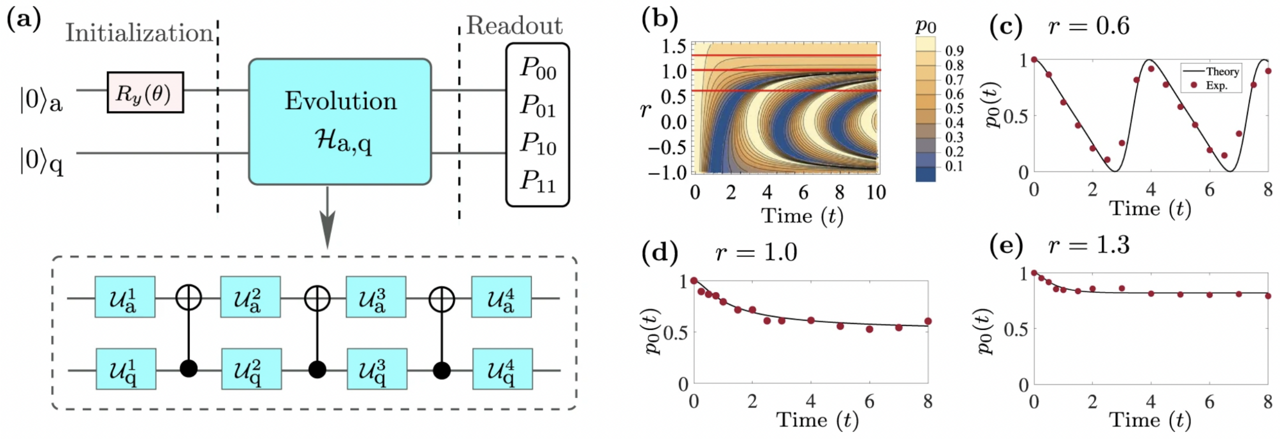

Fig. 3.4: (a) Schematics of the gate sequence applied on the qubit and ancilla. $R_y(\theta)$ is the rotation along y-axis of the ancilla qubit. The evolution is implemented by a set of single qubit rotations and three CNOT gates. (b) The evolution of the system is shown in a color plot as r varies. (c) A cut from panel (b) in the unbroken PT-symmetry phase, showing asymmetric oscillatory evolution. (d) A cut from panel (b) at the exceptional point. (e) A cut from panel (b) in the broken PT-symmetry phase, showing decaying evolution. Figure from [22].

3.2 Non-Hermiticity in quantum experiments

3.2.1 Dilation

In this part, I explain the basics of the dilation method to simulate PT-symmetric systems. The dilation method harnesses the unitary gates by increasing the dimension of Hilbert space [23, 24, 25]. By including an ancillary qubit, we can decompose non-unitary pulses into unitary gates, which is more desirable since quantum computers work in Hermitian limits with unitary operators. We can simulate the PT-symmetric Hamiltonian by post-selecting on the evolutions where the ancillary qubit is at a certain state. Realizing gain and loss in a quantum system is challenging because gain introduces noise, and loss makes the measurement challenging. The dilation method can be used to simulate PT symmetry digitally. Here, I follow the work done in reference [22].

The PT-symmetric Hamiltonian to simulate is:

$$H_q = \sigma_x + ir\sigma_z, \tag{3.1}$$

with eigenvalues:

$$\lambda_{\pm} = \pm\sqrt{1 - r^2}, \tag{3.2}$$

where r is a parameter with real values. At $r = 1$ there is an exceptional point where the two eigenvalues and eigenstates coalesce. For $r > 1$ the eigenvalues are imaginary and for $r < 1$ the eigenvalues are real.

The Hamiltonian in equation 3.1 can be realized with the help of an ancillary qubit. The Naimark dilation method is harnessed with an operator $\mathcal{H}_{a,q}(t)$. Ancillary qubit and target qubit follow the Schrödinger equation as follows:

$$i\frac{d}{dt}\left|\Psi_{a,q}(t)\right\rangle = H_{a,q}\left|\Psi_{a,q}(t)\right\rangle, \tag{3.3}$$

where the solution is:

$$\left|\Psi_{a,q}(t)\right\rangle = \left|0\right\rangle_a \left|\psi(t)\right\rangle_q + \left|1\right\rangle_a \left|\bar{\psi}(t)\right\rangle_q, \tag{3.4}$$

where $i\frac{d}{dt}\left|\Psi_q(t)\right\rangle = H_q\left|\Psi_q(t)\right\rangle$ gives the state $\left|\Psi_q(t)\right\rangle$. $\left|\bar{\psi}(t)\right\rangle_q = \eta(t)\left|\Psi_q(t)\right\rangle$ with $\eta(t) = [(1+\eta_0^2)e^{-iH_q^\dagger t}e^{-iH_q t} - I]^{1/2}$ and $\eta(0) = \eta_0 I$. Initially, both qubit and ancilla are in ground state $\left|0\right\rangle$, then we apply a Y-rotation on the ancilla qubit with an angle θ. Then we implement unitary $U_{a,q}(t) = \mathcal{T}\exp\left[-i\int_0^t \mathcal{H}_{a,q}(\tau)d\tau\right]$ in order to implement different values of r. For an arbitrary value of r and t this unitary can be found by decomposition into single $\mathcal{U}_q^j(a)$—where j represents the three degrees of freedom for the rotation—and two-qubit gates (CNOT). After the unitary implementation, the qubit and ancilla are measured in qubit-ancilla basis

$\{|00\rangle, |11\rangle, |01\rangle, |11\rangle\}$. The gate sequence is shown in Fig. 3.4a. Then we post-select on the population that has ancilla qubit at state $|0\rangle$.

After constructing the dilation method to realize the PT-symmetric Hamiltonian, we can vary r and observe the evolution of the post-selected states. Figure 3.4b shows the PT transition from the unbroken PT-symmetry phase to the broken PT-symmetry phase at $r = 1$. The cut from the oscillatory behavior in the unbroken region is shown in Fig. 3.4c where $r = 0.6$ and undergoes asymmetric oscillation due to the interplay between drive and the gain and loss effect near EP. Figure 3.4d shows the behavior of the system at the EP with $r = 1$, and at $r = 1.3$ the system is in the broken region with decaying evolution.

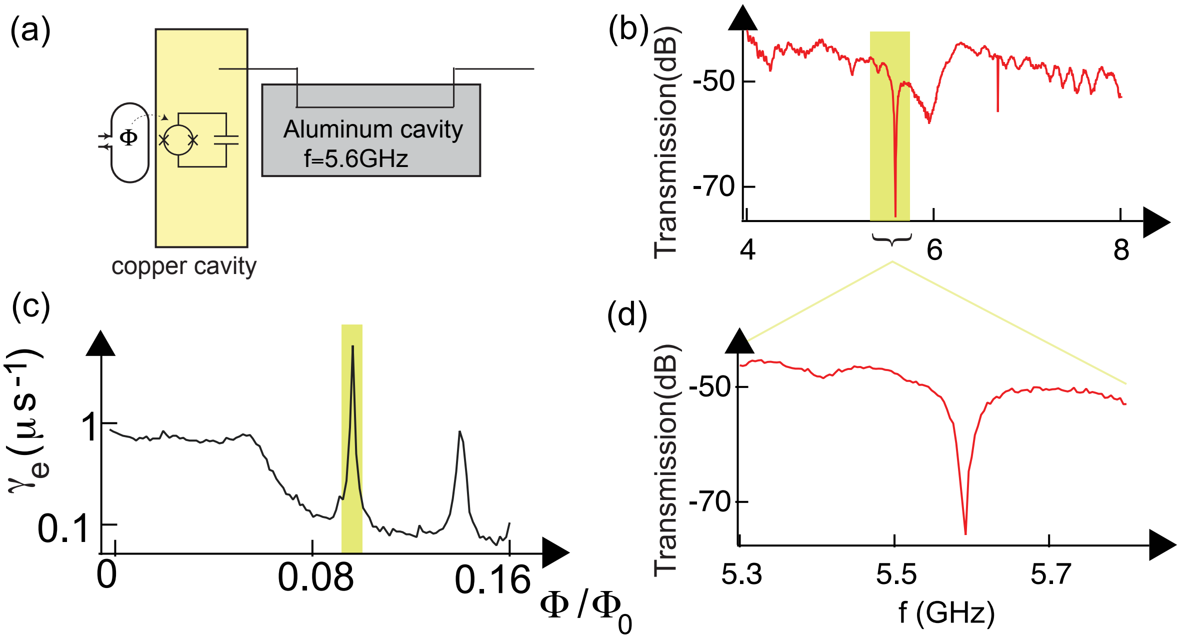

Fig. 3.5: (a) Schematic of the qubit-cavity system with the filter cavity at the output. (b) The reflection off of the cavity to observe the filter cavity resonance. (c) The relaxation rate of the state $|e\rangle$ as a function of the relative flux change.

3.3 Experimental setup

In this section, I introduce our setup in detail and explain how we achieve non-Hermiticity in superconducting circuits [26, 27]. Generally, we use anharmonic systems formed from a nonlinear circuit, which have many discrete states, from which we can pick the desired energy transitions—in the case of qubits, we only need one energy transition. In superconducting circuits, the higher states possess the same properties as the first two levels and can be addressed individually due to the anharmonicity that differentiates different transitions. However, as we go up to higher states, the system experiences higher decoherence rates which depends on the change in coupling and the local density of states at the transition frequency ($\Gamma_{i\to f} \propto \langle f|\, H\, |i\rangle^2 \rho(\omega_{fi})$). The density of states can be manipulated by bath engineering techniques [28, 29, 30], so that we increase the density of states available for $|e\rangle \leftrightarrow |g\rangle$ while reducing it for $|f\rangle \leftrightarrow |e\rangle$. Here, our goal is to design a system that allows us to have a mode-selective loss system with post-selection. This can be done by manipulating the bath to enhance the relaxation rate of the superconducting circuit at certain frequencies and impedes relaxation at other frequencies. In this experiment, a resonator with desired frequency was inserted at the output of the readout cavity, Fig. 3.5a, where the transmission line is coupled inductively to the cavity. Here, we utilized an aluminum cavity with frequency around 5.6 GHz—the reflection data from the cavity is shown in Fig. 3.5b. The filter has linewidth of about 6 MHz, which is clear in the zoomed area in Fig. 3.5d. The cavity acts as a filter when put on the output of the readout cavity. Due to the small linewidth of the cavity and the challenges in fabricating superconducting circuits, it's difficult to design a cavity-qubit system with the exact matching frequency. To overcome this challenge, instead, we use a tunable qubit to bring the $|g\rangle$–$|e\rangle$ transition to match the filter frequency. To have the ability to tune the qubit frequency we place the qubit inside a copper cavity and add coil around the cavity so that we can apply current through the SQUID loop of the qubit. For further information about qubit fabrication and setup please refer to [31].

Given a tunable qubit and a filter that increases the density of states at frequencies around 5.6 GHz, we can find the decay values corresponding to the qubit frequencies and realize a mode-selective loss system, which is also known as passive PT-symmetric system. To do so, we vary the current in the coil around the copper cavity, and measure the relaxation time T_1 at different frequencies—Fig. 3.5c shows how this decay depends on different values of the flux. The relaxation rate $\gamma_e = 1/T_{1e}$ of the $|g\rangle$–$|e\rangle$-transition peaks around $\Phi/\Phi_0 = 0.1$, corresponding $f = 5.7$ GHz and is slower around this peak. Moreover, Fig. 3.5c can be used to predict the effect of filter cavity on the $|g\rangle$–$|e\rangle$ transition since the anharmonicity of about 300 MHz, puts $|e\rangle$–$|f\rangle$ transition frequency 5.4 GHz at the flat region of the plot i.e. when the density of state is expressed. Based on the data, we choose $\gamma_e = 6\ \mu\mathrm{s}^{-1}$ and $\gamma_f = 0.2\ \mu\mathrm{s}^{-1}$, where γ_f is sufficiently small that it can be ignored, to realize a mode selective loss system.

The experimental setup inside a Bluefors dilution refrigerator is shown in Fig. 3.6a. The input line is microwave coax line with attenuators placed in each stage of the fridge. The Impedence Mismatch Element (IME)—which is the filter cavity—is placed immediately after the qubit-cavity system. This is followed by circulators to avoid the noise from the output line from entering the cavity. A Josephson parametric amplifier and HEMT amplifier are used to amplify the output signal.

We perform homodyne measurement to measure the state of the qubit. The qubit and cavity have a large detuning Δ, which results in weak coupling. This allows us to simplify the interaction Hamiltonian of the coupled system:

$$H = (\omega_c - \chi\sigma_z)a^\dagger a - \frac{1}{2}\omega_q\sigma_z, \tag{3.5}$$

where σ_z is the qubit basis, $a^\dagger$ and a are the cavity's creation and annihilation operator and $\chi = g^2/\Delta$. We measure the shift in cavity frequency to determine the state of the qubit, since the frequency is dependent on $\langle\sigma_z\rangle$. To distinguish the three states of the qubit, we use JPA (Josephson Parametric amplifier) [32, 33] in its phase-sensitive mode to amplify one quadrature of the cavity signal and de-amplify the other quadrature. The dispersive cavity shift for $\{|e\rangle, |f\rangle\}$ are $\chi_e/2\pi = -2$ MHz and $\chi_f/2\pi = -11$ MHz. In Fig. 3.6b, the two quadratures of the cavity signal are shown when there the qubit's state is at $|g\rangle$, $|e\rangle$, $|f\rangle$, and the corresponding histogram of the "I" quadrature is shown in Fig. 3.6c. This is done by sending a pulse with three points where the first point is no pulse corresponding to the ground state, the second pulse prepare the qubit at $|e\rangle$ and third pulse prepare the qubit at

$|f\rangle$.

3.4 Post-selection

The next step is to achieve a bipartite mode-selective loss system. We need to be able to separate the dynamics of the qubit and its dissipation to the environment. Utilizing the fact that we can separately access each transition in a qubit, we take the ground state $|g\rangle$ as our environment and $|e\rangle$ and $|f\rangle$ as the two-level system. As mentioned in the previous subsection, in order to have high fidelity single shot measurement, we use Josephson parametric amplifier. This will give us separation between the three states population as shown in Fig. 3.6. By post-selecting on the final states in $|f\rangle$ and $|e\rangle$, we eliminate experiments with jumps to $|g\rangle$. The population that started in $|e\rangle$–$|f\rangle$ manifold will decay to $|g\rangle$ with the rate γ_e. We can normalize the population of the $|e\rangle$–$|f\rangle$ manifold by dividing $|e\rangle$ or $|f\rangle$ population by the sum of the two states population, as follows:

$$P'_e(t) = \frac{P_{e/f}(t)}{P_e + P_f},\ P'_f(t) = \frac{P_{e/f}(t)}{P_e + P_f}. \tag{3.6}$$

where $P_{e/f}$ are the original populations and P' is the renormalized population after post-selection.

The mode-selective non-Hermitian qubit can be comprehended by formulating the Lindblad equation as follows:

$$\dot{\rho}(t) = -i[H, \rho] + \mathcal{L}_e \rho \mathcal{L}_e^\dagger - \frac{1}{2}\{\mathcal{L}_e^\dagger \mathcal{L}_e, \rho\} + \mathcal{L}_f \rho \mathcal{L}_f^\dagger - \frac{1}{2}\{\mathcal{L}_f^\dagger \mathcal{L}_f, \rho\}, \tag{3.7}$$

where $H = J(|f\rangle\langle e| + |e\rangle\langle f|)$ represents the Hamiltonian, and $\mathcal{L}_e$ and $\mathcal{L}_f$ are the Lindblad dissipators for the $|e\rangle$ and $|f\rangle$ states, respectively. If $\gamma_f << \gamma_e$, we can disregard the

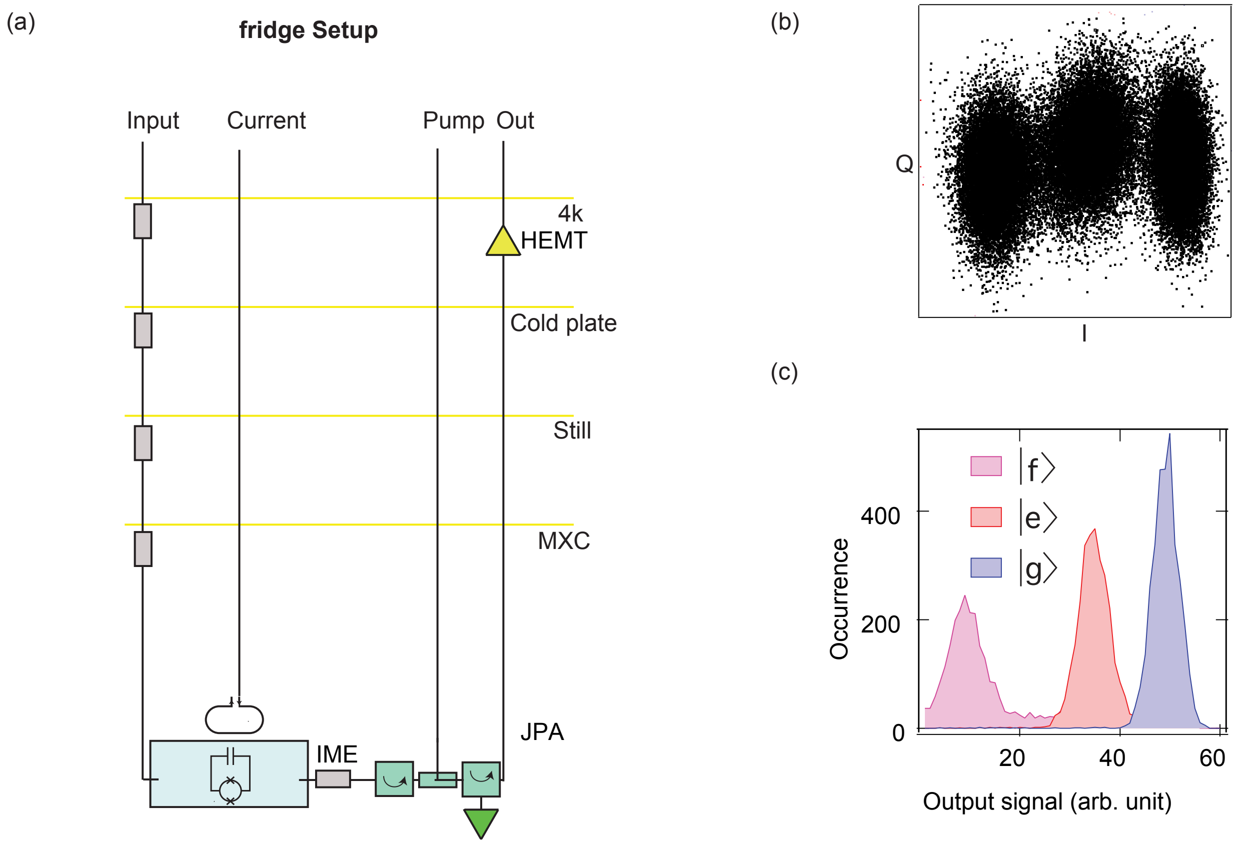

Fig. 3.6: (a) Schematic of the fridge setup: The schematic shows the different stages of the dilution fridge, with attenuators at the input line and amplifiers (JPA and HEMT) and circulators and IME (the filer cavity) at the output line. (b) I and Q quadrature of the readout signal showing separation between the three levels of the trasmon $\{|g\rangle, |e\rangle, |f\rangle\}$. (c) Histogram of the panel (b), projected on the I quadrature.

contribution of $\mathcal{L}_f$ and approximate Eq. 3.7 to:

$$\dot{\rho} = -i[H, \rho] + \mathcal{L}_e \rho \mathcal{L}_e^\dagger - \frac{1}{2}\{\mathcal{L}_e^\dagger \mathcal{L}_e, \rho\}, \tag{3.8}$$

where the first term characterizes the unitary evolution, the second term accounts for the quantum jumps due to measurement, and the last term represents the non-unitary evolution. By implementing post-selectionâeffectively eliminating the quantum jumps from $|e\rangle$ to $|g\rangle$âwe remove the second term and obtain the following equation of motion:

$$\dot{\rho} = -i[H - \frac{i}{2}\mathcal{L}_e^\dagger \mathcal{L}_e, \rho]. \tag{3.9}$$

The term $H - \frac{i}{2}\mathcal{L}_e^\dagger \mathcal{L}_e$ within the commutator in Eq. 3.9 constitutes the effective non-Hermitian Hamiltonian of interest [34].

3.5 Static EP

In this section, I explain the measurements performed on the system described above, which is an open quantum system with three anharmonic levels with the two higher levels undergoing dissipation to the ground state $|g\rangle$ [35]. We aim to investigate the non-Hermitian properties of our system, starting with the Parity-Time (PT)-symmetry transition from the unbroken to the broken regimes. The transition marks a location of the system's degeneracy known as an Exceptional Point 'EP'. Afterward, we explore other signatures of the EP by measuring the decoherence rate as a function of the frequency detuning and associated complex eigenvalues. Finally, we observe a significant signature of EP which is the non-orthogonality of the eigenstates.

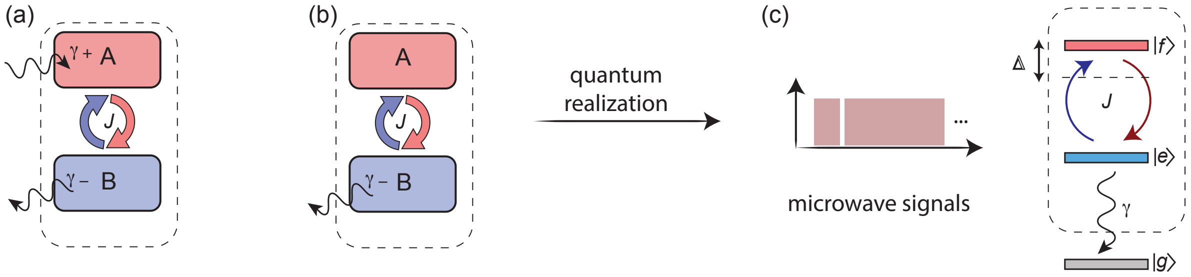

Fig. 3.7: (a) Balanced gain and loss bipartite system coupled with the rate J. (b) Mode-selective loss bipartite system. (c) Quantum equivalent of a mode-selective system in panel (b).

3.5.1 Parity-Time symmetry breaking transition

We discussed Hermitian quantum mechanics in Ch. 3.1. In this description, the physical system has purely real spectra and undergoes unitary time evolution. If the system is not closed, we cannot simply apply notions of Hermitian quantum mechanics to our experimental system. However, Hermiticity is not a fundamental requirement for quantum systems and different formalism have been developed to deal with non-Hermitian systems. PT-symmetric systems with balanced gain and loss are a well-known example of a non-Hermitian system that was discussed in Ch. 3. Here, we aim to realize a bipartite PT-symmetric system Fig. 3.7a. However, realizing gain is challenging for our superconducting circuit. In this experiment, we take an equivalent approach by taking only a lossy system that has PT-symmetric properties Fig. 3.7b. We set the frequency of the qutrit at the desired value, where the loss from $|e\rangle$ is considerably faster than $|f\rangle$, Fig. 3.7c. By post-selecting on the $\{|e\rangle$–$|f\rangle\}$ population, we can describe our quantum system by the following effective non-Hermitian Hamiltonian [36, 35]:

$$H_{NH} = J(|f\rangle\langle e| + |e\rangle\langle f|) + (\Delta - i\gamma_e/2)\,|e\rangle\langle e|\,, \tag{3.10}$$

where J is the coupling rate between the $|e\rangle$ and $|f\rangle$-states. This parameter is set by the strength of the microwave drive. Δ is the detuning of the microwave drive for the $|g\rangle$–$|e\rangle$-transition, and γ_e is the decay rate of the $|e\rangle$ state. In order to observe the transition between the PT-symmetric phase and PT-broken phase in the energy spectrum, we tune J from 0 to 10π MHz and examine the dynamics of the non-Hermitian qubit under constant drive for different values of J. Similar to a balanced gain-loss system, where the energy spectrum moves from purely real to purely imaginary, we can observe the energy difference going from purely real to purely imaginary. The energy difference is given by:

$$\delta\lambda = \lambda_+ - \lambda_- = \sqrt{4J^2 - (\Delta - i\gamma_e/2)^2}, \tag{3.11}$$

where $\lambda_\pm = i\gamma/4 \pm \sqrt{4J^2 - (\Delta - i\gamma_e/2)^2}$. There is an overall decay term for the eigenvalues in comparison to the balanced gain-loss system, which can be explained by the decomposition of the Hamiltonian:

$$H_{NH} = J(|f\rangle\langle e| + |e\rangle\langle f|) + (\Delta/2 - i\gamma_e/2)(|e\rangle\langle e| - |f\rangle\langle f|) - i\gamma_e/2(|e\rangle\langle e| + |f\rangle\langle f|). \tag{3.12}$$

The final term is an overall loss that the mode-selective loss system exhibits, which is absent in the PT-symmetric system with balanced gain and loss. The overall loss only shifts the location of the exceptional point from $J = \gamma/2$ to $J = \gamma/4$ for the eigenvalues difference. This equation makes the equivalence between Fig. 3.7a and Fig. 3.7b clear.

At $\Delta = 0$, the PT-transition from a purely real to a purely imaginary eigenvalue difference occurs. To observe the transition experimentally, we prepare our state by bringing it to the $\{|e\rangle\,,\ |f\rangle\}$ manifold via a π pulse. By looking at how the qubit state evolves under the constant drive over 4 μs with the strength J, we can find the location where the spectrum crosses imaginary values into real values. Since the $|e\rangle$ is more dissipative, we prepare the initial state at $|f\rangle$ with slower decay. During the evolution under this constant drive, we perform projective measurements in the Z-basis. The system undergoes damped Rabi oscillations. Extracting the oscillation frequency and damping rate gives the real and imaginary values of the spectrum, respectively. As we vary the coupling strength J, from 0 to $J = \gamma_e/4$, the quantum state undergoes purely damped evolution; while as we cross the exceptional point and move to J values that are larger than $\gamma/4$, we observe oscillatory behavior during evolution. The transition from damping to oscillation is the signature of the exceptional point. In Fig. 3.8, 2 μs evolution time of the system for J in the range [0,5] rad./μs is shown—this is a zoomed-in region of a 4 μs evolution for J range in [0,17] rad./μs this data is shown in Fig. 1 of [35]—where this transition happens at $J = \gamma/4$. Two cuts from Fig. 3.8a. show the damped evolution in the broken PT-symmetric region and oscillation in the unbroken PT-symmetric region Fig. 3.8b. The extracted frequency from the evolution in Fig. 3.8a is shown in Fig. 3.8d. Another unique feature which is present in Fig. 3.8a is the asymmetric oscillatory evolution near the EP owing to the strong interplay between loss and drive strength, Fig. 3.8c. The evolution has a steep positive slope on one side of the maximum and a slow change in the positive slope in the other direction. If we choose a point in the steep slope side, we can observe that the population changes starkly by slowly varying J. This behavior manifests the square root sensitivity of the energy spectrum to the system's parameters in proximity to the EP. This sensitivity might have application in quantum metrology and sensing—but the post-selection process may impose some constrains due to the low success rate at longer times.

So far we explored the energy spectrum on the $\Delta = 0$ line where it is either real or imaginary. However, if the detuning is set to nonzero values, we can study the complex

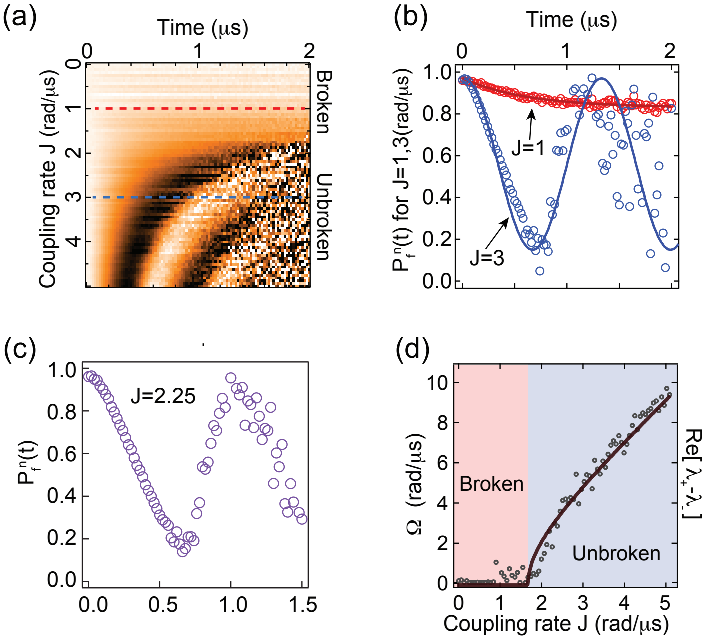

Fig. 3.8: (a) Color plot of the evolution under constant drive. (b) Two cuts from panel (a), where one is in the unbroken region (blue) and one is in broken region (red). (c) A cut from panel a, where J is near the EP, exhibiting asymmetric evolution. (d) Extracted oscillation frequency of the evolution from panel (a).

energies and their effect on the time evolution of the system. To observe the real and imaginary part of the spectrum, we need to extract the parameters of the damped oscillation while driving the system with fixed J and Δ. The evolution of a orbitrary state under this Hamiltonian looks like a damped oscillation. In order to understand that, we can mathematically show this correspondence:

$$U(t)|\psi(t)\rangle = e^{-iHt}\,|f\rangle = e^{-iHt}\alpha|+\rangle + e^{-iHt}\beta|-\rangle = e^{-iE_+t}\alpha|+\rangle + e^{-iE_-t}\beta|-\rangle = \\ e^{-i(Re(E_+)+iIm(E_+))t}\alpha|+\rangle + e^{-i(Re(E_-+iIm(E_-))t}\beta|-\rangle, \quad (3.13)$$

where E_+ and E_- are eigenvalues of the non-Hermitian Hamiltonian $|+\rangle$ and $|-\rangle$, and the imaginary part of these eigenvalues are the same for $\Delta = 0$ case. However, for non-zero detuning, the two states $|+\rangle$ and $|-\rangle$ have different imaginary parts which gives rise to a decaying profile of an oscillatory evolution—the oscillation arise from the real parts of the eigenvalues where $Re(E_+) = -Re(E_-)$. In this experiment we fixed the coupling rate $J = 6.9$ rad./μs and varied Δ. We let the system evolve for 4 μs where the system reaches the steady state (Fig. 3.9a) and then extract oscillation frequency Fig. 3.9b and damping rate Fig. 3.9c. Fig. 3.9c shows a sharp dependence of the decoherence rate on the detuning, which is part of the Reimann topology of this system. The steady state is also another property that can be studied in this system by letting the evolution settle on the final state. Here we performed quantum state tomography of all the Pauli expectation values at $t = 4$ μs to find the final state. We observed that the system reaches to the single eigenmode of the Hamiltonian at the exceptional point Fig. 3.9d.

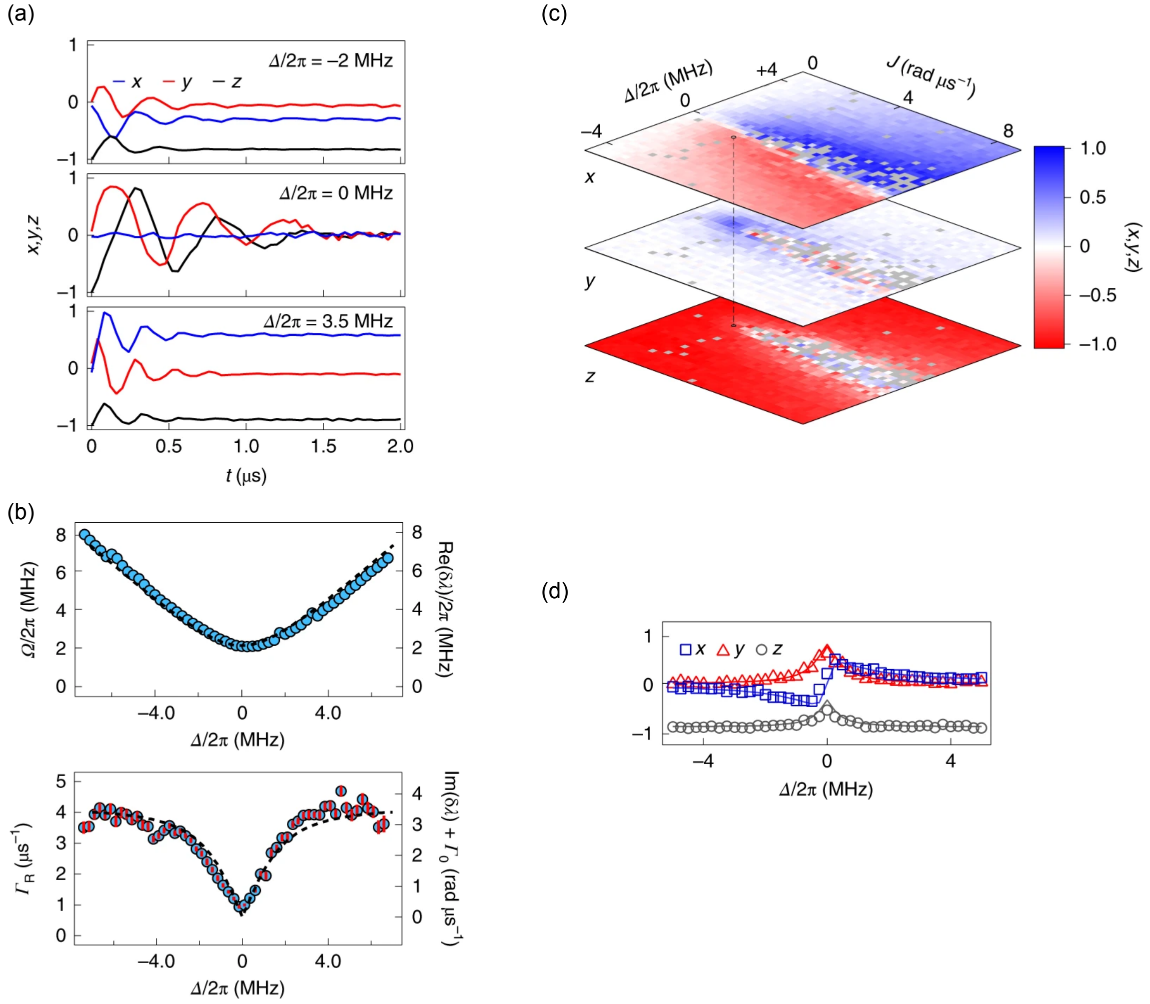

Fig. 3.9: (a) Time evolution of $|X-\rangle$ state as it reaches the steady state, when the detuning is $\{-2, 0, 3.5\}$ MHz. (b) The extracted oscillation frequency and decay rate from rabi oscillation with different detuning and fixed $J = 6.9$ rad./μs. (c) The tomography of the steady state for different values of J and Δ. (d) The steady state tomography shown for $J = \gamma/4$ as Δ is varied.

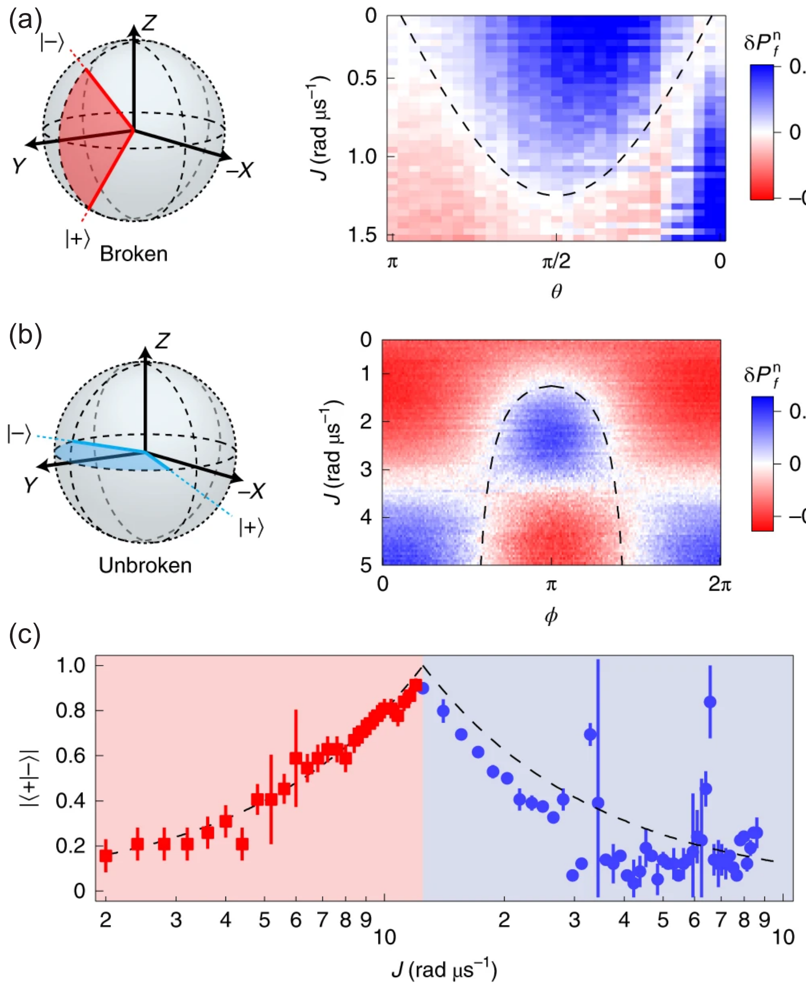

Fig. 3.10: (a) Varying the phase along Z–Y plane of the bloch sphere as J is changed in the broken PT-symmetry phase. (b) Varying the phase along X–Y plane of the bloch sphere as J is changed in the unbroken PT-symmetry phase. (c) Extracted eigenstate overlap as J is varied.

3.5.2 Non-orthogonality of the eigenstates

Another unique property of non-Hermitian systems is the dependence of the angle between the eigenstates to the proximity to EP. In a Hermitian system, the eigenstates are always orthogonal to each other, and the Hamiltonian is always diagonalizable. However, in our Hamiltonian, the two eigenstates overlap with each other and move closer to each other until they collapse at the EP, where the Hamiltonian is non-diagonalizable. We observe this effect by preparing the system at different initial states on the Bloch sphere and varying the drive strength. We can locate the eigenstates in the unbroken regime by looking at the oscillation under constant drive; if the axis of rotation is along the eigenstates, we observe no oscillation. In the broken regime, the eigenstate does not undergo decay and stays stationary. In Fig. 3.10, the color plot shows the difference between two points during the evolution $\delta P_f^n = P_f^n(t = 0) - P_f^n(t = 500ns)$ as the drive strength varies. We observed that the eigenstates stay on the X–Y plane Fig. 3.10a in the unbroken region and the Y–Z plane Fig. 3.10b in the broken region. The overlap between the eigenstates is shown in Fig. 3.10c.

3.5.3 Conclusion

We showed how the presence of an exceptional point in the energy spectrum of a system results in complex eigenvalues and enhanced decoherence rate near the EP. Many investigations have been done in the classical domain that offered applications in sensing, energy transfer, and topological control, which makes this study valuable [37, 38, 39]. We showed that many of the same behavior can be seen in quantum systems and discussed the limitations they face in these systems. This study offer an avenue for harnessing the PT-symmetric system as a novel setting for quantum information science.

3.6 Dynamical tuning of the non-Hermitian Hamiltonian

In this chapter, I introduce the extension of the static Hamiltonian to a time-dependent case, where we can study the unique topology of the non-Hermitian systems [40]. This will help us understand adiabatic processes and their limitations in dissipative systems. The role of quantum jumps becomes vital in these systems [41]. Finally, we introduce an alternative approach to understanding the dissipative dynamics of a system [42].

3.6.1 Riemann sheet topology

The energy landscape of the non-Hermitian Hamiltonian exhibits an interesting topology known as the Riemann topology owing to its complex spectrum. The imaginary part of the eigenvalues introduces an extra degree of freedom enabling exciting phenomena such as the mode switching of the eigenstates. In this section, I focus on our work on encircling the EP to explore this topology.

The energy landscape of the Hamiltonian is shown in Fig. 3.11(a, b) in terms of J the coupling rate and Δ, the detuning. The real and imaginary surfaces exhibit degeneracies at $J = \pm\gamma/4$ and $\Delta = 0$, shown in Fig. 3.11(a, b) as EPs. The real surfaces have a branch cut in the broken region where the two eigenvalue surfaces meet, while the imaginary surfaces have a branch cut in the unbroken region. The branch cut allows a smooth connection between the two sheets. We aim to show this smooth transition by allowing the system to evolve as we slowly vary the parameters in a closed loop. In the case, as the Adiabatic theorem states, the system follows the instantaneous eigenstates, if the parameters are varied sufficiently slowly. In order to move on to the instantaneous eigenstates, we need to implement the loop

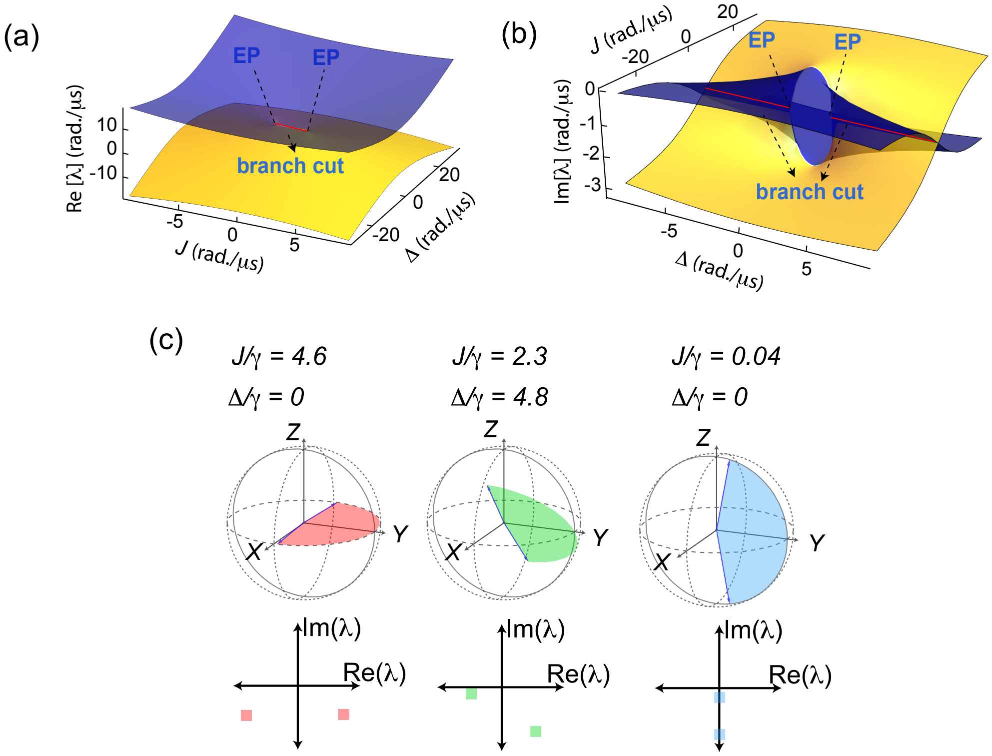

Fig. 3.11: (a) The real part of the eigenvalues in terms of J and Δ form the Riemann sheet topology. The two exceptional points of the system are shown. The branch cut where the two sheets meet is shown in red, where it is in between the two EPs. (b) The imaginary part of the eigenvalues in terms of J and Δ. The branch cut, in this case, is in the unbroken region. (c) Three different parameter values and their corresponding eigenstates (on the Bloch sphere) and eigenvalues are shown.

in an adiabatic process. The stark difference between the Hermitian and non-Hermitian cases is that the system does not bring the state back to its initial state; instead, it ends up in an orthogonal state. This difference is due to the presence of a branch cut that allows the instantaneous eigenvalues to continuously change into each other in the non-Hermitian case. The instantaneous eigenstates for three different parameters are shown in Fig. 3.11 on the Bloch sphere.

3.6.1.1 Encircling the exceptional point in a closed loop

We perform this experiment in the same setup introduced in Sec .4.3. While the Hamiltonian parameters were constant for a given evolution in that section, here, we dynamically control the Hamiltonian parameter during the evolution to observe chiral energy transfer and examine the accumulated phase during this evolution. We construct the closed loop by a variable drive with $\Delta(t)$, a time-dependent detuning, and, $J(t)$, a time-dependent coupling rate in a cosine form. We vary these parameters to encircle the exceptional point in a closed loop slowly. The forms of these parameters are:

$$J(t) = (J_{\max} - J_{\min}) \cos(\pi t/T) + J_{\min}, \tag{3.14}$$

$$\Delta(t) = \Delta_{\pm} \sin(2\pi t/T), \tag{3.15}$$

where $J_{\max} = 30$ rad./μs, T is the period of one loop and $\Delta_{\pm} = \pm 10\pi$ rad./μs^{-1}.

The state is prepared at $|-\rangle$ by applying a $\pi/2$ pulse; this pulse brings the state to the instantaneous eigenstate of the Hamiltonian at $t = 0$. After the preparation, we implement the loop. During the evolution, we pause at different points of the loop and perform measurements to determine the system's state. The measurement is the quantum state tomography where the system is projected on the three axes of measurement X, Y, and Z— with this information, we can construct the density matrix. The evolution is divided into 200 time points and state tomography is performed at each point—$x \equiv \langle \sigma_x \rangle$, $y \equiv \langle \sigma_y \rangle$, $z \equiv \langle \sigma_z \rangle$.

The evolution of the state $|-\rangle$ under the parameter change in a counterclockwise direction is shown in Fig. 3.12a. After a complete loop, the final state is in the $|+\rangle$, corresponding to the eigenenergy on the other Riemann surface. The evolution can be viewed as a walk through the real part of the Riemann sheets where the branch cut allows for the transition to the other Riemann surface, Fig. 3.12b. There are limitations in the duration of the evolution due to the presence of dissipation, which results in non-adiabatic coupling manifesting itself in oscillations shown in Fig. 3.12a. The evolution on the imaginary surface is shown in Fig. 3.12c, which shows small dissipation close to zero throughout the evolution. The experimental data shows good agreement with the simulated data shown in dashed lines in Fig. 3.12a. The simulation was done using Mathematica by solving the Lindblad master equation with $\gamma_e = 6.2$ rad./μs^{-1} and $\gamma_f = 0.32$rad./μs^{-1}.

Performing the same loop only in the clockwise direction does not produce the same result, as shown in Fig. 3.12d. If we walk through the real part of the Riemann sheet as we vary the parameters, the topology suggests the state transfer to $|+\rangle$. Instead, we observe that the system suddenly jumps to the other sheet without following the instantaneous eigenstates. We can explain this behavior by mapping the eigenvalues of the static Hamiltonian on the imaginary part of the Riemann surface; as shown in Fig. 3.12e, the parameter path undergoes an evolution that increases the dissipation. This results in the breakdown of adiabaticity and strong non-adiabatic coupling. After the jump to the other energy sheet, the system experiences less dissipation. For this case, the simulation data is shown with dashed lines and agrees well with the experimental data.

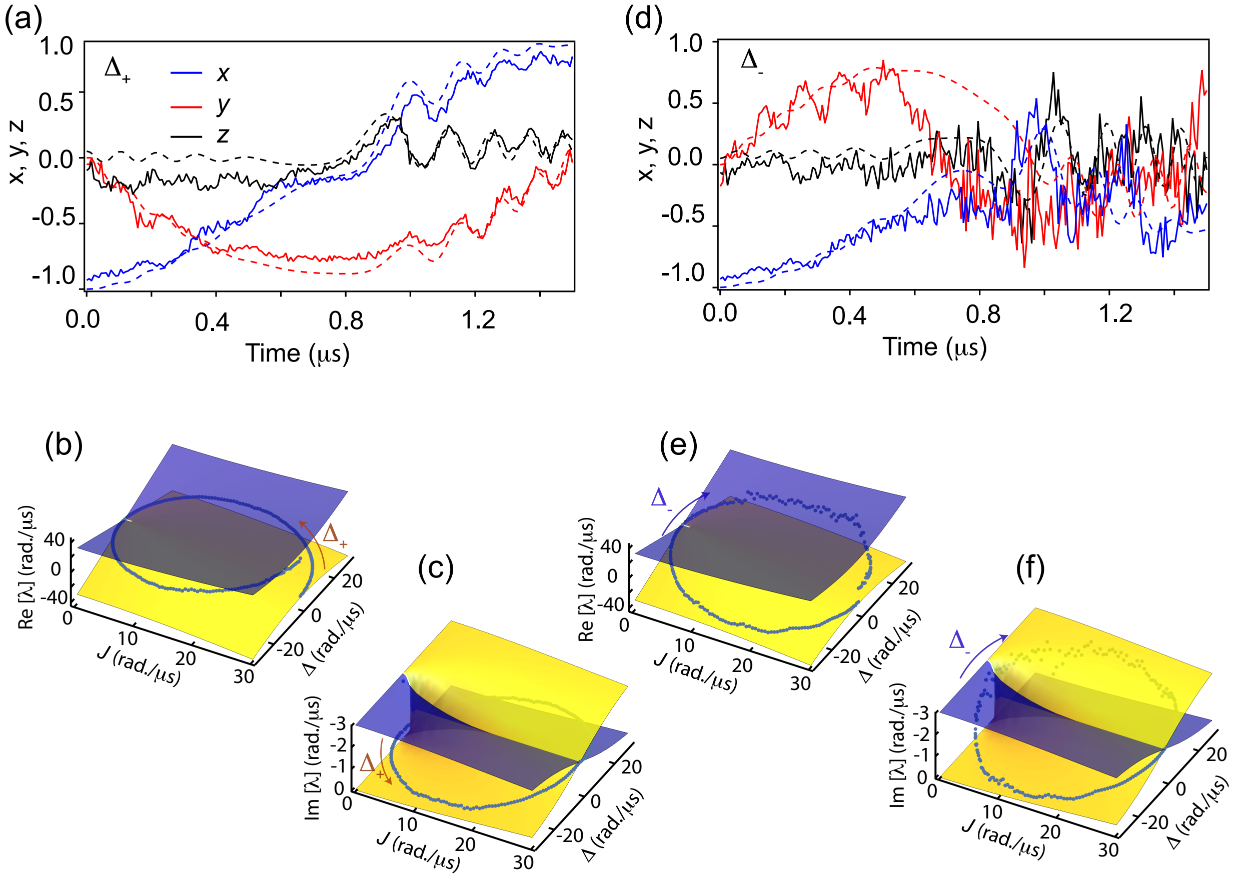

Fig. 3.12: (a) Encircling the EP in CCW direction. The evolution of the qubit under the closed loop is shown, where quantum state tomography is performed, and the simulation is overlaid on the evolution with dashed lines. (b) Evolution on the real part of the Riemann surfaces for CCW direction. (c) Evolution on the imaginary part of the Riemann surfaces for CCW direction. (d) Encircling the EP in CW direction and the simulation data (dashed lines). (e) Evolution on the real part of the Riemann surfaces for CW direction. (f) Evolution on the imaginary part of the Riemann surfaces for CW direction.

3.6.2 Phase measurement

To investigate the coherent nature of this state transfer, we look at the phase accumulation and its amplitude. We harness the higher levels of our transmon circuit as a phase reference. The geometric and dynamical phases are global phases that are not observable without a reference. To prepare such a phase interference experiment, we start with a superposition between $|h\rangle$ state and the eigenstate of the Hamiltonian $(1/\sqrt{2}\,|h\rangle + 1/\sqrt{2}\,|-\rangle)$. This pulse sequence is shown in Fig. 3.13a, where two rotation pulses one in $|g\rangle$–$|f\rangle$ and one in $|e\rangle$–$|f\rangle$ was applied to bring the state to $|h\rangle$. As the system evolves under the parameter loop in $|e\rangle$–$|f\rangle$ manifold, $|\psi_\pm\rangle$ acquires a dynamical and geometric phase. while the population in $|f\rangle$–$|h\rangle$ manifold does not undergo any drive and stays constant. The closed loop is the encircling loop in Eqs. 3.14 and 3.15.

Here, we keep $T = 800$ ns and vary J_{min} in the range [-15,15] rad./μs^{-1}. After a complete loop, we perform a Ramsey-like measurement by projecting the final state to $(1/\sqrt{2}\,|h\rangle + 1/\sqrt{2}\,|\psi_\pm\rangle)$ and extracting the accumulated phase. The final pulse sweeps the angle in the range $[0, 2\pi]$, creating a sine wave with phase and contrast information, Fig. 3.13b. The phase and the contrast are extracted for each J_{min} value. Figure 3.13c shows the contrast of the interference, where projection on $|\psi_+\rangle$ (solid lines) has higher contrast around J_{min}, where the two exceptional points are located. We observe that projection on the state $|\psi_+\rangle$ is higher. This path follows the Riemann sheet topology, and around $J_{\text{min}} = 0$ gives the highest contrast.

In Fig. 3.13d, the probability of the state transfer is provided for each of these projections. in this case, the initial state is not a superposition with $|h\rangle$. We can observe that even though, in the CW direction, the population in $|\psi_+\rangle$ is smaller than $|\psi_-\rangle$, the contrast is higher near J_{min}. We can conclude that due to the higher contrast, the path following the Riemann sheets is coherent in nature.

Finally, in Fig. 3.13(e, f), we measure the accumulated phase over this process. The total phase consists of two parts: the dynamical phase and the geometric phase:

$$\chi = \int_0^T E(t) + \chi_{\text{geometric}}. \tag{3.16}$$

The first term is the dynamical phase, which depends on the energy and the time it takes for the system to evolve. The second term is the geometric phase which depends on the path the parameters take during this evolution. If we take a closed loop in the parameter space, we have two possibilities. First, if the system follows the Riemann sheets and spends half of the evolution time on one sheet and the second half on the other sheet: in this case, the dynamical phase is canceled because the energies are opposite to each other. Second, the system stays in one sheet: in this case, the dynamical phase is accumulating over time. Figure 3.13e depicts the case where the final state is projected on the initial state, where the state evolves on only one Riemann sheet. The two directions have similar dynamical phase accumulation for the given J_{min} range. Figure 3.13f depicts the case where the final state is projected on the orthogonal state, where the state evolves on both Riemann sheets. The two directions have similar about zero dynamical phase accumulation for the given J_{min} range. However, we can see that these two directions are different by π, which is a chiral geometric phase that was predicted in [43, 44, 45, 46, 47, 48].

3.6.3 Fast driving limit

The objective of this section is to investigate the dependence and efficiency of the state transfer on the rate of the parameter change and proximity to the EP. Since the closed loop we use for this study is a periodic Hamiltonian, we draw a connection between the Floquet

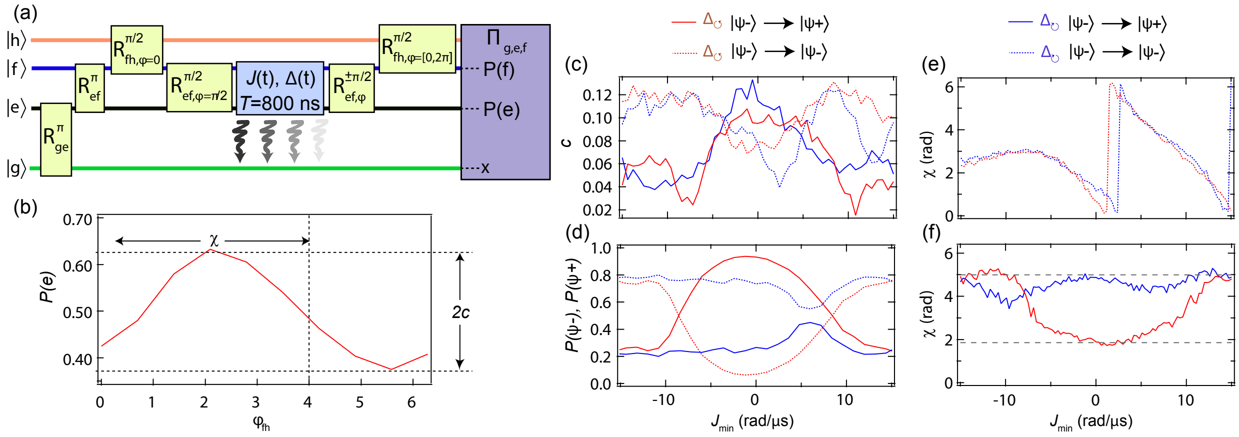

Fig. 3.13: (a) Pulse sequence for phase measurement experiment, R^{π}_{ge} brings the state to excited state, R^{π}_{ef} brings the state to $|f\rangle$ state, $R^{\pi/2}_{hf}$ and $R^{\pi/2}_{ef}$ creates the superposition state. $R^{\pm\pi}_{ef}$ projects the state on $|\pm\rangle$. (b) Interference contrast results from $R^{\pi/2}_{fh,\phi=[0,2\psi]}$, with oscillation amplitude of c and phase χ. (c) The contrast of interference is shown as a function of $J_{\min}$. (d) State transfer probability is shown as a function of $J_{\min}$. (e) The accumulated phase is when the state is projected on $|+\rangle$. (f) The accumulated phase is when the state is projected on $|-\rangle$.

picture and our Hamiltonian. The parameter loop follows Eqs. 3.14 and 3.15. In this study, we vary both $J_{\min}$ and the duration T, while keeping $\Delta_{\pm} = \pm 10\pi$.

In Fig. 3.14(a,b), we show the probability of state transfer $P(\psi_{-})$ at the end of each loop as we vary $J_{\min}$ in the range [-30,30] rad./μs and the duration of the loop $T \in$ [0.1,2] μs. In CCW direction, Fig. 3.14a, the state transfer happens with high probability in a region between [-5,5] rad./μs, which is a larger area as the region between the two exceptional points. Moreover, this state transfer happens even for shorter times. However, this plot does not give us any information about how the system evolves within the evolution time. A cut at a constant $J_{\min}$ of 6 rad./μs is shown in Fig. 3.14c in red, which is shown with a dashed line in Fig. 3.14a. We can see that there are small oscillations present with changes in the duration.

In the CW direction, shown in Fig. 3.14b, we can observe a different behavior where for most parameters, the state transfer does not occur. For shorter durations, there is a higher chance of state transfer, while this probability decreases over a longer time. The role of dissipation becomes more prominent in longer durations, which results in a lower chance of state transfer in this direction. The finer features and oscillations are present in this direction as well. A cut from his plot at a constant $J_{\min}$ of 6 rad./μs is shown in Fig. 3.14c in blue and indicated in Fig. 3.14b with a dashed line. The oscillation amplitudes are larger in this case.

To understand the state transfer under parameter variation of the loop, we compare the state transfer at the end of the loop with the relevant eigenvalues $\epsilon_{\pm}$ and eigenstates $|\phi_{\pm}(t)\rangle = |\phi_{\pm}(t+T)\rangle$ of the Floquet Hamiltonian. This Hamiltonian is defined as follows:

$$G(T+t,t)|\phi_{\pm}(t)\rangle = \eta_{\pm}|\phi_{\pm}(t)\rangle, \tag{3.17}$$

where $G(T+t,t) = \exp\left[-i\int_t^{T+t} H(t')dt'\right]$ and $\epsilon_\pm = i\ln\eta_\pm/T$ are two Floquet quasi-energies.

Our typical experimental parameters are ($\gamma = 7/\mu$s, $J_{\max} = 30$ rad./μs, and $\Delta = 10\pi$ rad./μs). Figure 3.14d shows normalized difference of Floquet exponents, $\Delta\eta \equiv (|\eta_+| - |\eta_-|)/(|\eta_+| + |\eta_-)|$. The boundary between $\Delta\eta = 0$ and $\Delta\eta > 0$ marks the Floquet EP contours; they only occur for $J_{\min} < -\gamma/4$ and, at larger Δ are pushed further down. The non-orthogonality of the Floquet eigenvectors, $|\langle\phi_+|\phi_-\rangle|$ 3.14e and the mode-switch probability $P(\psi_-)$ Fig. 3.14f, on the other hand, track each other. The CCW direction in Fig. 3.14a has qualitatively similar features with Fig. 3.14e, while smaller features in both Fig. 3.14(a,b) have good agreement with Fig. 3.14e.

Dynamical study of the non-Hermitian systems and their corresponding Reimann sheet topology allow us to explore topological invariants [49, 50]. We can further extend this study to higher order Hamiltonian and invistigate eigenvalues braiding and exotic topological classes[51, 52]. Moreover, study the dynamical features can reveal interesting and unique features in Floquet non-Hermitian systems [53], opening an avenue to study periodic behavior of these systems.

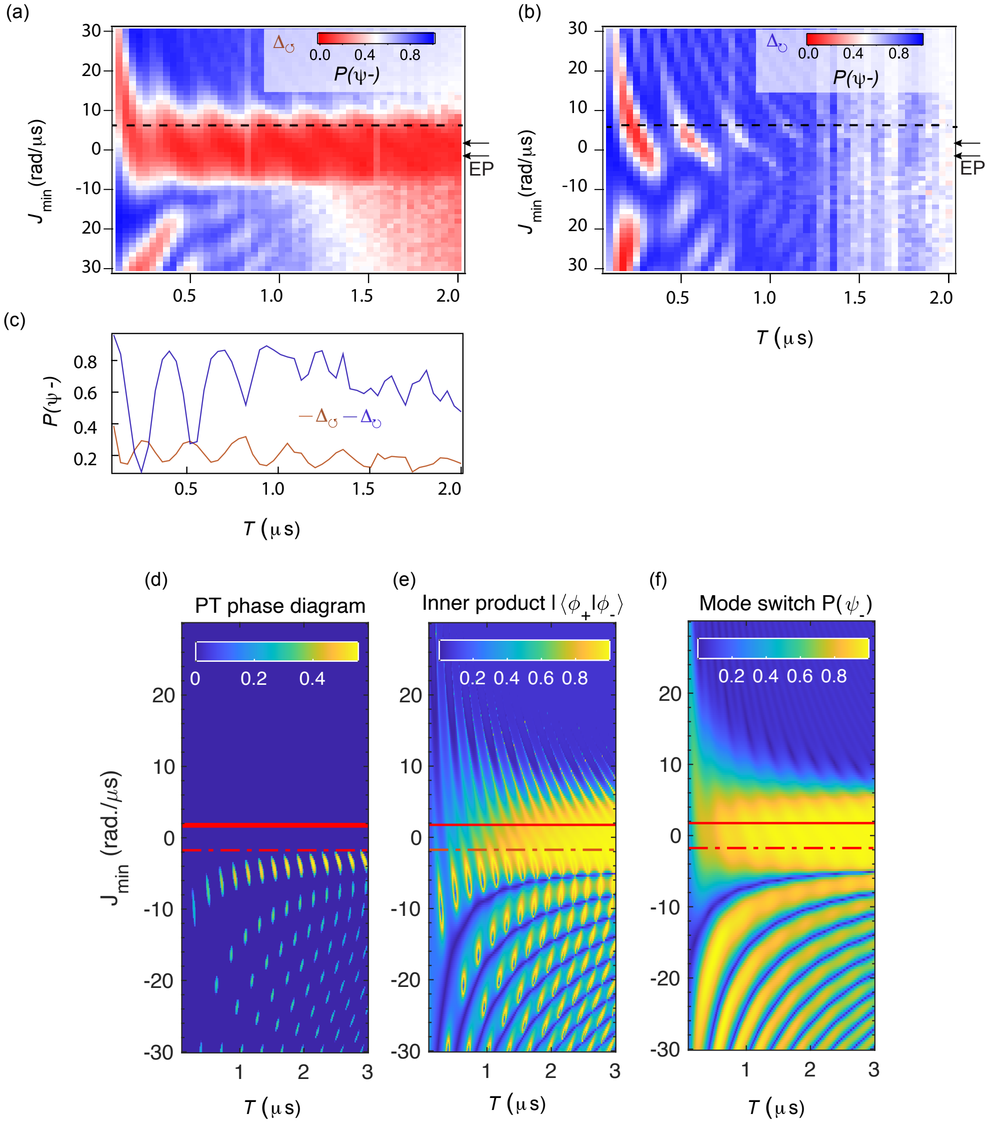

Fig. 3.14: (a) Final projection on the $|-\rangle$ in CCW direction, as the duration and min value of J_{min} varies for each loop. (b) Final projection on the $|\psi_{-}\rangle$ in CW direction, as the duration and min value of J_min varies for each loop. (c) A cut (dashed lines) from panel a(b) for a constant J_min and different T for CCW(CW) direction is shown in red(blue). (d) Theoretical calculation of energy eigenvalues of the floquet Hamiltonian. (e) Theoretical calculation of the overlap between the eigenstates of the floquet Hamiltonian. (f) Theoretical calculation of final projection on the $|-\rangle$ in CCW direction.

3.6.4 Quantum jumps

So far, we considered the decay from $|f\rangle$ to be negligible; however, this decay can be an essential factor for a longer duration in predicting the dynamics of the system. Moreover, the dissipative qutrit undergoes dephasing in both transitions. Here, we characterized the non-unitary dynamics and the effect of quantum jumps and dephasing on the dynamics of our effective non-Hermitian dynamics.

We used the Lindblad master equation to look at the dynamics of the effective non-Hermitian Hamiltonian in the previous section of this chapter. The master equation is described in the following form:

$$\frac{\partial \rho_{\text{tot}}}{\partial t} = -i[H_{\text{c}}, \rho_{\text{tot}}] + \sum_{k=e,f} [L_k \rho_{\text{tot}} L_k^\dagger - \frac{1}{2}\{L_k^\dagger L_k, \rho_{\text{tot}}\}], \tag{3.18}$$

where ρ_{tot} is the 3×3 density operator. The Lindblad dissipators $L_e = \sqrt{\gamma_e}\,|g\rangle\,\langle e|$ and $L_f = \sqrt{\gamma_f}\,|e\rangle\,\langle f|$ corresponding to the decoherence from $|e\rangle$ to $|g\rangle$ and from $|f\rangle$ to $|e\rangle$, respectively. The drive is applied only in the $\{|e\rangle, |f\rangle\}$ sub-manifold with Hamiltonian $H_{\text{c}} = J(|e\rangle\,\langle f| + |f\rangle\,\langle e|) + \Delta/2(|e\rangle\,\langle e| - |f\rangle\,\langle f|)$—where Δ is the frequency detuning of the drive frequency from the $|e\rangle$–$|f\rangle$ transition and J is the coupling rate.

Post-selection allows us to isolate the dynamics of the $|e\rangle$–$|f\rangle$ and describe the system with the following form:

$$\frac{\partial \rho}{\partial t} = -i(H_{\text{eff}}\rho - \rho H_{\text{eff}}^\dagger) + L_f \rho L_f^\dagger, \tag{3.19}$$

where $H_{\text{eff}} = H_{\text{c}} - iL_e^\dagger L_e/2 - iL_f^\dagger L_f/2$. If $L_f = 0$, we can ignore the effect of quantum jumps from $|f\rangle$ state, which makes the dynamics unitary under H_{eff}. The non-zero γ_f has a small impact on the dynamics of the encircling process with short evolution time $T = 1.5\ \mu\ \text{s}^{-1}$. The spectrum of the effective non-Hermitian Hamiltonian with γ_f is shown in Fig. 3.15(b,c).

Comparison to the non-zero γ_f is shown in Fig. 3.15f, where the location of the EP is shifted to $J = (\gamma_e + \gamma_f)/4$ compared to Fig. 3.15b. However, this picture does not account for the last term in Eqn. 3.19, which is the quantum jumps effect.

To capture the effect of quantum jumps, we use a hybrid-Liouvillian approach [54, 34, 55, 56]. we define two Liouvillian superoperators and describe the dynamics through the superoperators:

$$\frac{\partial \rho}{\partial t} = (\mathcal{L}_0 + \mathcal{L}_1)\rho, \tag{3.20}$$

where $\mathcal{L}_0\rho \equiv -i(H_{\text{eff}}\rho - \rho H_{\text{eff}}^\dagger)$ and $\mathcal{L}_1\rho \equiv L_f \rho L_f^\dagger$. To solve for the eigenvalues of the hybrid-Liouvillian superoperator, we bring the superoperators of the Eqn.3.20 to the matrix form, where the dimension of Liouville space is $N^2 = 4$:

$$\mathcal{L}_0 = \begin{pmatrix} -\gamma_e & iJ & -iJ & 0 \\ iJ & -(\gamma_e+\gamma_f)/2 & 0 & -iJ \\ -iJ & 0 & -(\gamma_e+\gamma_f)/2 & iJ \\ 0 & -iJ & iJ & -\gamma_f \end{pmatrix}. \tag{3.21}$$

$$\mathcal{L}_1 = \begin{pmatrix} 0 & 0 & 0 & \gamma_f \\ 0 & 0 & 0 & 0 \\ 0 & 0 & 0 & 0 \\ 0 & 0 & 0 & 0 \end{pmatrix}. \tag{3.22}$$

where $H_{\text{c}} = J(|e\rangle\langle f| + |f\rangle\langle e|) + \Delta/2(|e\rangle\langle e| - |f\rangle\langle f|)$. In this formalism, the density matrix is a 4 × 1 vector:

$$\rho = \begin{pmatrix} \rho_{ee} & \rho_{ef} \\ \rho_{fe} & \rho_{ff} \end{pmatrix} \to \begin{pmatrix} \rho_{ee} \\ \rho_{ef} \\ \rho_{fe} \\ \rho_{ff} \end{pmatrix}. \tag{3.23}$$

First, we start with the eigenvalues of the $\mathcal{L}_0$ which corresponds to the evolution under H_{eff}:

$$\lambda_{0,1} = -(\gamma_e + \gamma_f)/2, \tag{3.24}$$

$$\lambda_{2,3} = -(\gamma_e + \gamma_f)/2 + 1/2\sqrt{(\gamma_e - \gamma_f)^2 - 16J^2}, \tag{3.25}$$

where this superoperator has a third-order hLEP (Hybrid-Liouvillian Exceptional Point) degeneracy at $J = (\gamma_e + \gamma_f)/4$. The imaginary and real parts of the eigenvalues of the Hybrid-Liouvillian Matrix $\mathcal{L}_0$ are shown in Fig. 3.15a and Fig. 3.15c, respectively. Since Eqn.3.20 does not have an i as opposed to Eqn.3.19, we compare the real part of the H_{eff} eigenvalues to the imaginary part of the Liouvillian superoperators, and vice versa. Another difference is that the second-order EP corresponds to the third-order hLEP in this formalism.

If we add the effect of $\mathcal{L}_1$ in the hL picture, the eigenvalues become:

$$\lambda_0 = -(\gamma_e + \gamma_f)/2 - \frac{M}{6N^{1/3}} + \frac{1}{6}N^{1/3}, \tag{3.26}$$

$$\lambda_1 = -(\gamma_e + \gamma_f)/2 \tag{3.27}$$

$$\lambda_{2,3} = -(\gamma_e + \gamma_f)/2 + \frac{(1 \pm i\sqrt{3})M + (-1 \pm i\sqrt{3})N^{2/3}}{12N^{1/3}}, \tag{3.28}$$

where $M = 48J^2 - 3(\gamma_e - \gamma_f)^2$ and $N = 216\gamma_f J^2 - \sqrt{(216\gamma_f J^2)^2 + M^3}$. We observe that the third-order hLEP is lifted. The spectra are shown in the presence of γ_f, where the degeneracy is lifted. The splitting of the eigenvalue's real and imaginary parts leads to enhancement of the decoherence rate, which can be understood by looking at the eigenvalues difference:

$$Re[\lambda_0 - \lambda_{2,3}] = 3/4(\gamma_e^2\gamma_f)^{1/3}, \tag{3.29}$$

as well as enhancement in oscillatory behavior:

$$Im[\lambda_{2,3}] = \sqrt{3}/4(\gamma_e^2\gamma_f)^{1/3}. \tag{3.30}$$

These two effects occur due to the cube-root topology of hLEP, Fig. 3.16b.

Now we turn to the experimental observation of the hybrid-Liouvillian picture, where the quantum jumps and gain and loss effect compete, Fig. 3.16a. Similar to the method we used in Sec.3.5.1 to extract the oscillation frequency, we prepare the system at state $|f\rangle$ and drive the system with the rate J. By extracting the oscillation frequency and damping rate for 3 μs evolution time, we can achieve real and imaginary parts of the hybrid-Liouvillian spectra. Figure 3.16c shows excellent agreement between the theoretical prediction of the Liouvillian superoperator eigenvalues and the experimental values. Moreover, we observe the rapid enhancement of the decoherence rate in the vicinity of the hLEP.

To study the broken PT-symmetric region and the role of quantum jumps in this region, we investigate the evolution to the stationary state. The H_{eff} has two eigenstate $|+\rangle$ and $|-\rangle$, where decoherence rate of $|+\rangle$ is faster than $|-\rangle$. So the non-Hermitian dynamics favor the state with less loss, as shown in the exceptional point's encircling. The $\mathcal{L}_0$ eigenmatrices are the constructed with the same state $\rho_0 = |+\rangle\langle+|$ and $\rho_3 = |-\rangle\langle-|$. In the presence of quantum jumps $\mathcal{L}_1$, ρ_0 falls on the steady state of the H_{eff}. We can experimentally observe this behavior by preparing the state at $|-\rangle$ and let the system reach the steady state with

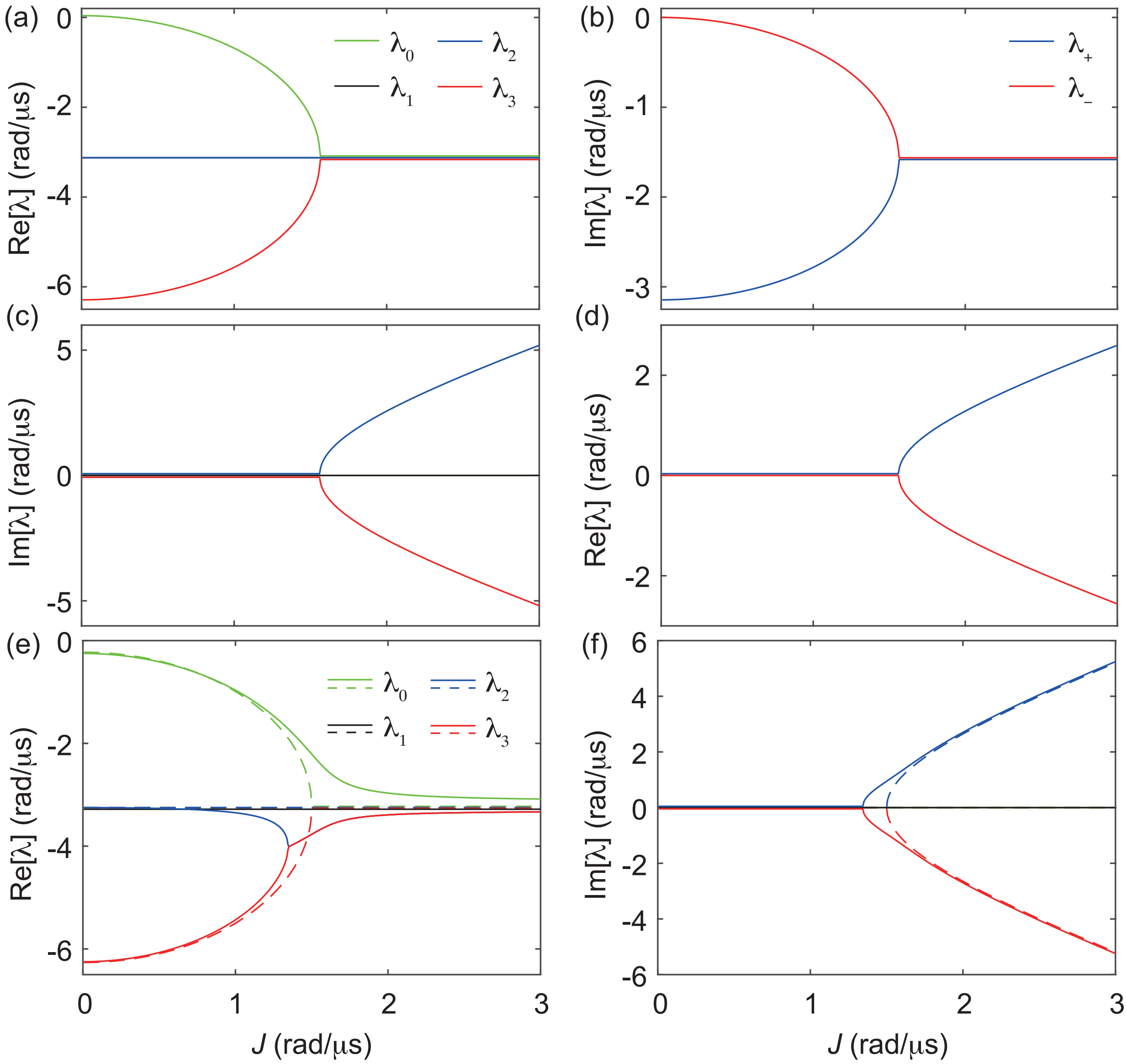

Fig. 3.15: Left panels show the Hybrid-Liouvillian spectrum, and right panels show the effective non-Hermitian Hamiltonian spectrum. At $\gamma_f = 0$, the imaginary (a) and real (c) parts of the hybrid-Liouvillian eigenvalues are compared to the real (b) and imaginary (d) parts of the effective non-Hermitian Hamiltonian. At $\gamma_f = 0.25\mu s^{-1}$, the imaginary part of the hybrid-Liouvillian eigenvalues is compared to the real part of effective non-Hermitian Hamiltonian.

the drive at $J = 0.85$ rad/μs^{-1}—which puts the system in the broken region. Figure 3.16e depicts the 2 μs evolution of the state with non-exponential decay to the steady state in a shorter time-scale than γ_f suggests. This is the consequence of the quantum jump, which then creates a non-zero overlap $\langle -|f\rangle$. In this case, the population of $|+\rangle$ grows and results in non-exponential decay to steady-state. We can confirm this by looking at the entropy, which increases as a result of quantum jumps, creating a mixed state. It's shown in Fig. 3.16f that the entropy increased at a point around $t \approx 0.6$ μs.

Finally, we study the slow driving limit, where the qubit's parameters change in a way that satisfies $T|\lambda_+ - \lambda_-|$. The parameter path is constructed with changes in detuning in a closed path with a function $-30\pi \sin(2\pi t/T)$ rad/μs while keeping $J = 30$ rad/μs and $T = 4$ μs, shown in Fig. 3.17. We observe that in the first half of the evolution, the eigenstate shown in Fig. 3.17b evolves on the Riemann surface with lower loss (marked as red) and returns to the initial state. However, in the second half of the evolution, the state crosses the imaginary surface branch cut and enters the surface with more loss (marked as blue). The quantum state tomography of this evolution is shown in Fig. 3.17c. To confirm the occurrence of the quantum jump, we look at the entropy change again. Figure 3.17d shows an increase in entropy in the second half.

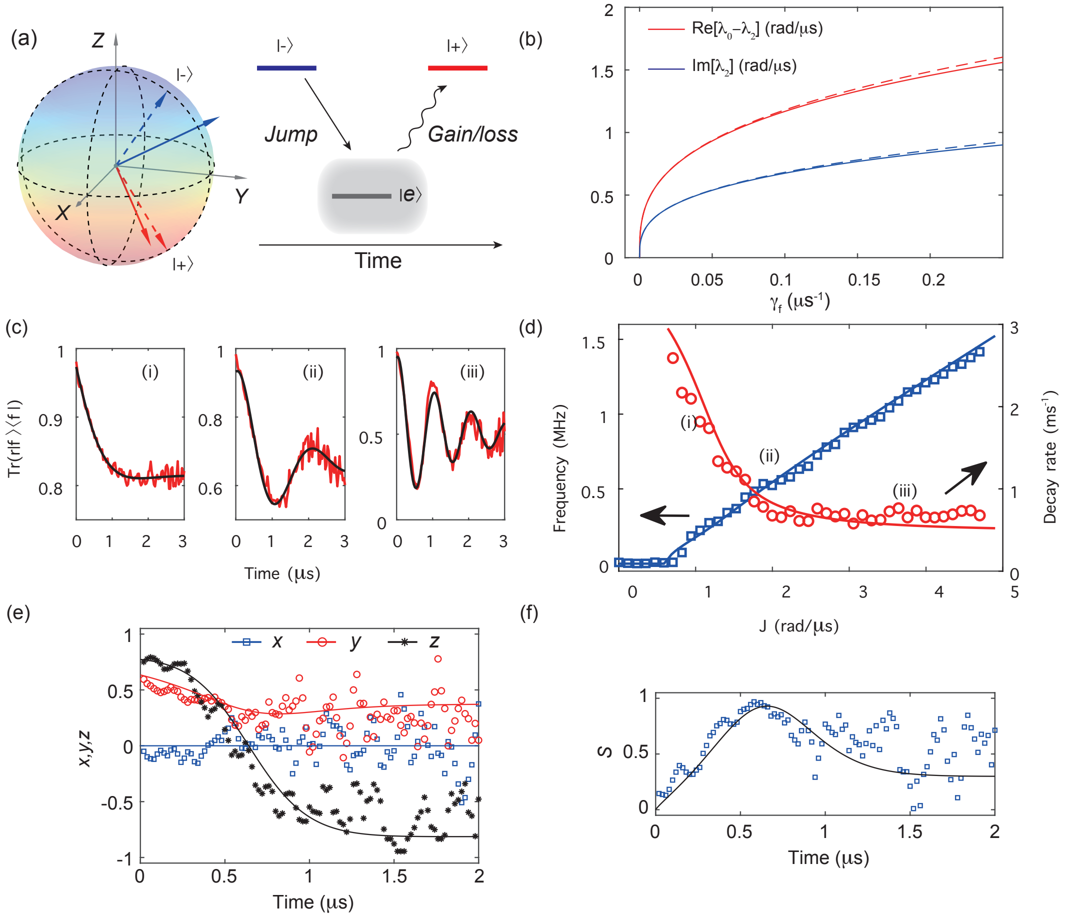

Fig. 3.16: (a) The competition between quantum jumps and the gain and loss effect results in mixed states shown on the Bloch sphere. (b) The enhancement of the decoherence rate and oscillatory behavior near EP. (c) The dynamics of the system under three different drive amplitudes. (d) The extracted oscillation frequency (blue) and decoherence rate (red) in terms of J values. The solid lines are theoretical predictions using Liouvillian spectra. (e) The evolution of the qubit prepared at the state with more loss. (f) Entropy changes during the evolution of the lossy state.

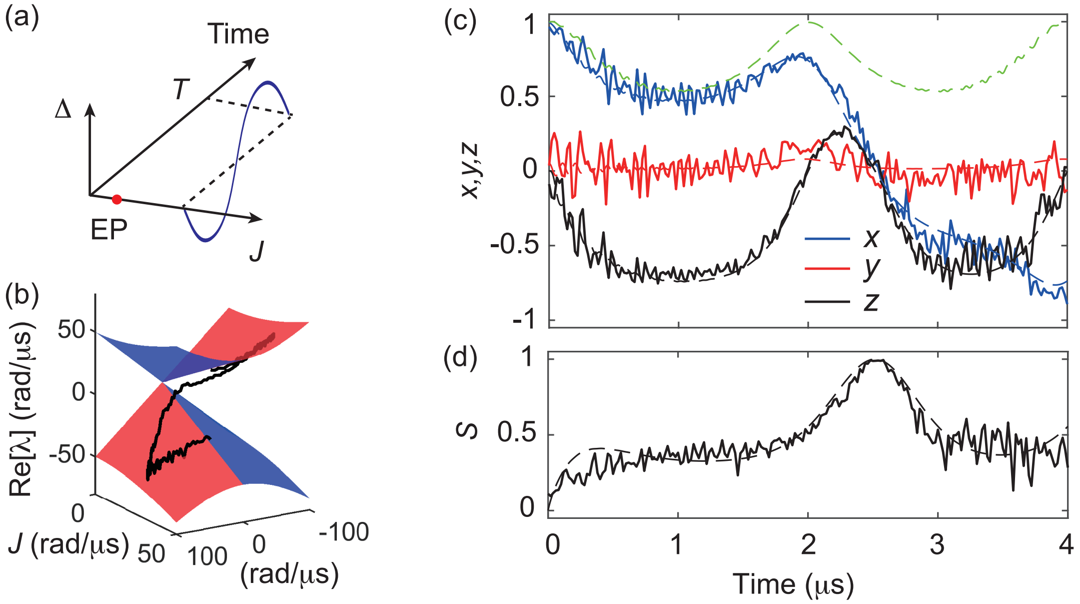

Fig. 3.17: (a) The drive detuning is changed in a closed loop with a sine function while the drive strength is kept constant. (b) The quantum state evolution is shown on the Riemann surfaces. (c) Quantum state tomography of the evolution under the drive in panel (a). (d) Entropy changes during evolution.

3.6.5 Decoherence-induced exceptional points

In this section, we focus on capturing the effect of decoherence within the manifold of the qubit and its impact on the dynamics of open quantum system from the perspective of Liouvillian Superoperators [57, 58]. This formalism allows us to investigate the non-unitary effect of the dissipation, which is not captured by effective non-Hermitian Hamiltonian. We will see that these systems possess EPs known as LEPs and can exhibit state transfer.

Here, we consider a Hamiltonian with two control parameters in $|g\rangle$–$|e\rangle$ manifold: Coupling rate J and detuning of the drive from the transition frequency Δ. The following form describes this:

$$H_\mathrm{c} = J(|g\rangle\langle e| + |e\rangle\langle g|) + \Delta/2(|g\rangle\langle g| - |e\rangle\langle e|). \tag{3.31}$$

The system undergoes spontaneous emission from $|e\rangle$ with the rate γ_e and dephasing rate γ_ϕ, Fig. 3.18. We can capture the dynamics of this dissipative qubit by a Liouvillian superoperator $\mathcal{L}$:

$$\dot{\rho} = -i[H_c, \rho] + \sum_{k=e,\phi} [L_k \rho L_k^\dagger - \frac{1}{2}\{L_k^\dagger L_k, \rho\}] \equiv \mathcal{L}\rho, \tag{3.32}$$

where $L_{e,\phi}$ are the jump operators, defined as $L_e = \sqrt{\gamma_e}\,|g\rangle\,\langle e|$ and $L_\phi = \sqrt{\gamma_\phi/2}\sigma_z$, and $H_\mathrm{c} = J(|g\rangle\langle e| + |e\rangle\langle g|) + \Delta/2(|g\rangle\langle g| - |e\rangle\langle e|)$. By bringing the superoperator into matrix form, we can extract its eigenvalues and eigenvectors:

$$\mathcal{L}_\mathrm{qubit}^\mathrm{matrix} = \begin{pmatrix} 0 & iJ & -iJ & \gamma_e \\ iJ & -i\Delta - \gamma_e/2 - \gamma_\phi & 0 & -iJ \\ -iJ & 0 & i\Delta - \gamma_e/2 - \gamma_\phi & iJ \\ 0 & -iJ & iJ & -\gamma_e \end{pmatrix}. \tag{3.33}$$

Where the eigenmodes are:

$$\rho_0 \propto \frac{1}{\gamma_e^2 + 8J^2} \begin{pmatrix} \gamma_e^2 + 4J^2 & 2i\gamma_e J \\ -2i\gamma_e J & 4J^2 \end{pmatrix}, \tag{3.34}$$

$$\rho_1 \propto \begin{pmatrix} 0 & 1 \\ 1 & 0 \end{pmatrix}, \tag{3.35}$$

$$\rho_{2,3} \propto \begin{pmatrix} -\gamma_e \mp \sqrt{\gamma_e^2 - 64J^2} & 8iJ \\ -8iJ & \gamma_e \pm \sqrt{\gamma_e^2 - 64J^2} \end{pmatrix}, \tag{3.36}$$

ρ_0 corresponds to the zero eigenvalue and ρ_1 is not an eigenvector leading to LEP since both of them are real eigenvalues. The two other eigenvectors can coalesce and create a second-order LEP at $J_{LEP} = \gamma_e/8 - \gamma_\phi/4$. At $\Delta = 0$, four eigenvalues of $\mathcal{L}$ and the LEP are shown in Fig. 3.18b.

To understand the emergence of exceptional point degeneracy in the two modes of the Liouvillian superoperator $\rho_{2,3}$, we can bring the Lindblad equation into Bloch equation form:

$$\begin{pmatrix} \dot{x} \\ \dot{y} \\ \dot{z} \end{pmatrix} = - \begin{pmatrix} \frac{\gamma_e}{2} + \gamma_\phi & \Delta & 0 \\ -\Delta & \frac{\gamma_e}{2} + \gamma_\phi & 2J \\ 0 & -2J & \gamma_e \end{pmatrix} \begin{pmatrix} x \\ y \\ z \end{pmatrix} + \begin{pmatrix} 0 \\ 0 \\ \gamma_e \end{pmatrix}. \tag{3.37}$$

It's evident that y and z components are coupled with the rate $2J$ and different losses, which makes the system a passive parity-time symmetric, Fig. 3.18c. To observe the LEP in experiment, the system is prepared at $|e\rangle$ and evolves under a drive strength J at $\Delta = 0$. 3 μs evolution of $|e\rangle$ to its steady state with different J is shown in Fig. 3.18d. The qubit exhibit transition from damped oscillation (red trace in Fig. 3.18e) to damped evolution

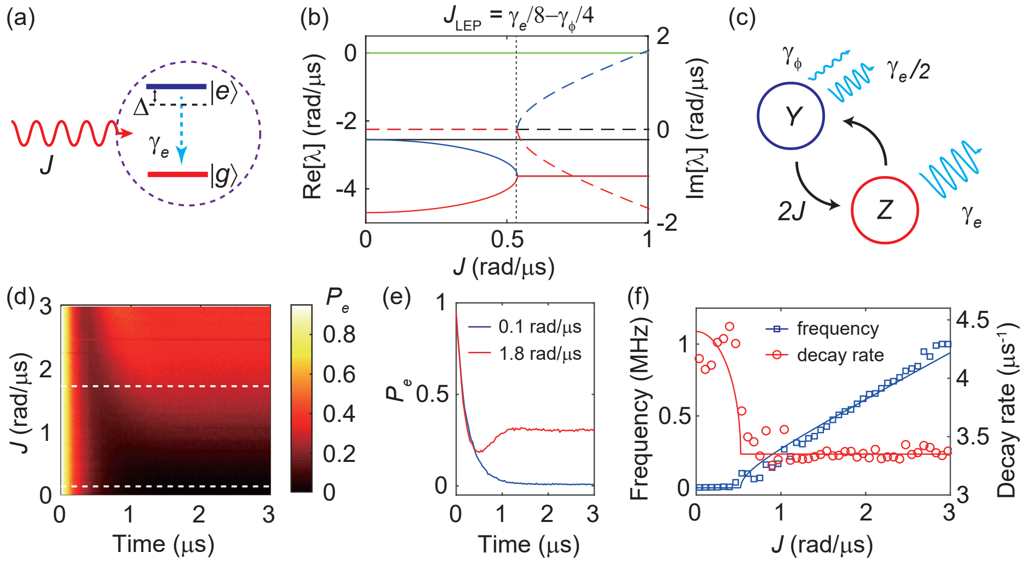

Fig. 3.18: (a) Schematic of the $|g\rangle$—$|e\rangle$ manifold with the relaxation rate of $|e\rangle$. (b) The real (solid lines) and imaginary (dashed lines) parts of the eigenvalues of the Liouvillian superoperator. The vertical dashed line indicates the LEP (c) Y and Z are the two components of Pauli's matrices which can be considered a two-level system with PT symmetry. (d) The color plot of the 3 μs evolution for different J values. (e) Two cuts from panel e are shown with dashed lines, where one is in the unbroken region (red) and one in the broken region (blue). (f) extracted decay rate (red) and frequency (blue) from panel d, which shows good agreement with the theoretical prediction (solid lines).

(blue trace in Fig. 3.18e) as J is varied in the range [0,3] rad/μs. The frequency and decay rate are extracted from Fig. 3.18d, which marks the location of LEP at $J = \gamma_e/8$, Fig. 3.18f.

The presence of the exceptional point corresponds to the Riemann sheet topology and the chiral state transfer phenomena. We can form a parameter loop similar to Sec.3.6.1.1 to explore this topology. In this experiment we choose a parameter loop with $J(t) = 16\cos^2(\pi t/T) rad./\mu\text{s}^{-1}$ and $\Delta(t) = \pm 10\pi \sin(2\pi t/T) rad./\mu\text{s}^{-1}$, where $T = 2$ μs, Fig. 3.19e. However, for a non-zero detuning, the Liouvillian superoperator has an LEP structure that consists of two third-order LEPs and triangular LEP lines, Fig. 3.19h. So the loop we have chosen encircles this structure rather than a single LEP.

We prepare the state at the eigenstates of the Hamiltonian at $t = 0$, which are $|\pm\rangle$. First, we look at the evolution of $|+\rangle$ in two different directions: In the Counter-Clockwise (CCW) direction, the state evolves to the $|-\rangle$ (Fig. 3.19a), while in Clockwise (CW) direction it comes back to the same state $|+\rangle$ (Fig. 3.19b). On the other hand, if we start with $|-\rangle$, the CCW direction comes back to the initial state $|-\rangle$ (Fig. 3.19c) and CW direction evolves into $|+\rangle$ (Fig. 3.19d).

This state transfer can be understood by averaging over an ensemble of trajectories (Fig. 3.19g) that undergo quantum jumps. The emergence of directionality arises from the quantum jump favoring $|g\rangle$. One example of a trajectory where a quantum jump occurs and brings the state to $|g\rangle$, in the beginning, is shown in Fig. 3.19f.

By introducing another energy state, we can explore a new and different type of LEP purely due to decoherence. Adding the $|f\rangle$ to our system changes the Liouvillian superoperator into 9×9 matrix:

$$\mathcal{L}_{\text{qutrit}}^{\text{matrix}} = \begin{pmatrix} 0 & iJ & 0 & -iJ & \gamma_e & 0 & 0 & 0 & 0 \\ iJ & -\gamma_e/2 & 0 & 0 & -iJ & 0 & 0 & 0 & 0 \\ 0 & 0 & 0 & 0 & 0 & -iJ & 0 & 0 & 0 \\ -iJ & 0 & 0 & -\gamma_e/2 & iJ & 0 & 0 & 0 & 0 \\ 0 & -iJ & 0 & iJ & -\gamma_e & 0 & 0 & 0 & 0 \\ 0 & 0 & -iJ & 0 & 0 & -\gamma_e/2 & 0 & 0 & 0 \\ 0 & 0 & 0 & 0 & 0 & 0 & \boldsymbol{0} & \boldsymbol{iJ} & 0 \\ 0 & 0 & 0 & 0 & 0 & 0 & \boldsymbol{iJ} & \boldsymbol{-\gamma_e/2} & 0 \\ 0 & 0 & 0 & 0 & 0 & 0 & 0 & 0 & 0 \end{pmatrix}, \tag{3.38}$$

where J is still drive in $|g\rangle$—$|e\rangle$ manifold. The bold elements in the matrix correspond to

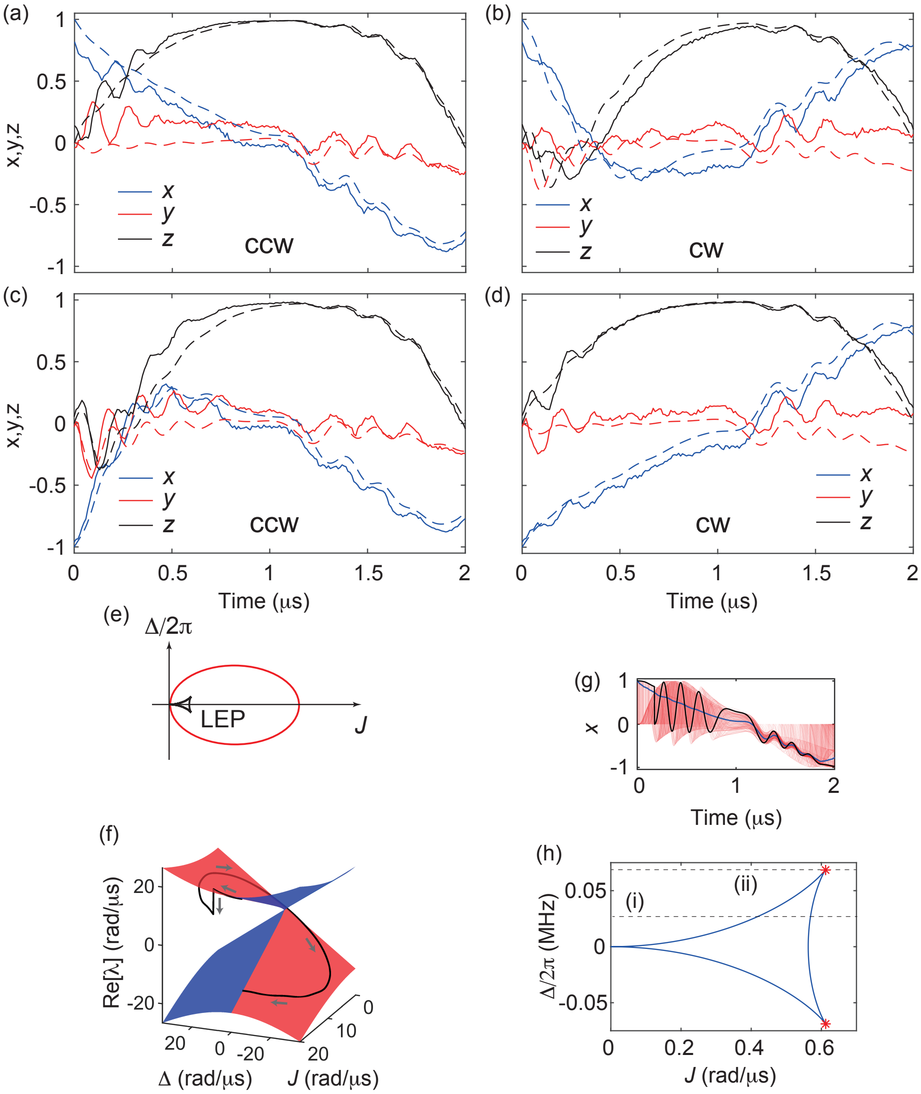

Fig. 3.19: (a,b) Quantum state tomography during the evolution of the state $|-\rangle$ under the encircling loop in CCW direction (a) and CW direction (b). (c,d) Quantum state tomography during the evolution of the state $|+\rangle$ under the encircling loop in CCW direction (c) and CW direction (d). (e) Schematic of the parameter loop encircling the LEP. (f) The projection of a trajectory undergoing one quantum jump on the Riemann sheet. (g) The solid black line shows an average of 1000 trajectories (red traces). (h) The structure of LEP, when detuning, is non-zero.

the LEP. The real and imaginary parts of the eigenvalues of this matrix are shown in Fig. 3.20(c,d). In this spectra, there are two types of LEP, where type-I LEP has been studied so far. Type-II LEP (at $J = \gamma_e/4$) arises from the coupling between the two coherence term of the density matrix ρ_{gf} and $\rho_{\rho_{ef}}$.

We can observe type II LEP if we prepare our state in a superposition of $1/\sqrt{2}(|g\rangle + |f\rangle)$, and then apply a constant drive in $|g\rangle$–$|e\rangle$ manifold. The system transition from the damped oscillation to exponential decay is measured by 4μs evolution of the ρ_{gf} element of the density matrix, Fig. 3.20a. The frequency and decoherence rate are extracted from Fig. 3.20a and shown in Fig. 3.20b as blue and red circles, respectively. The experimental result in Fig. 3.20b exhibits good agreement with the theoretical simulation, shown as solid lines in Fig. 3.20b. This exceptional point is interesting because it is non-local, i.e., it only depends on initial coherence between $|f\rangle$ and $|g\rangle$.

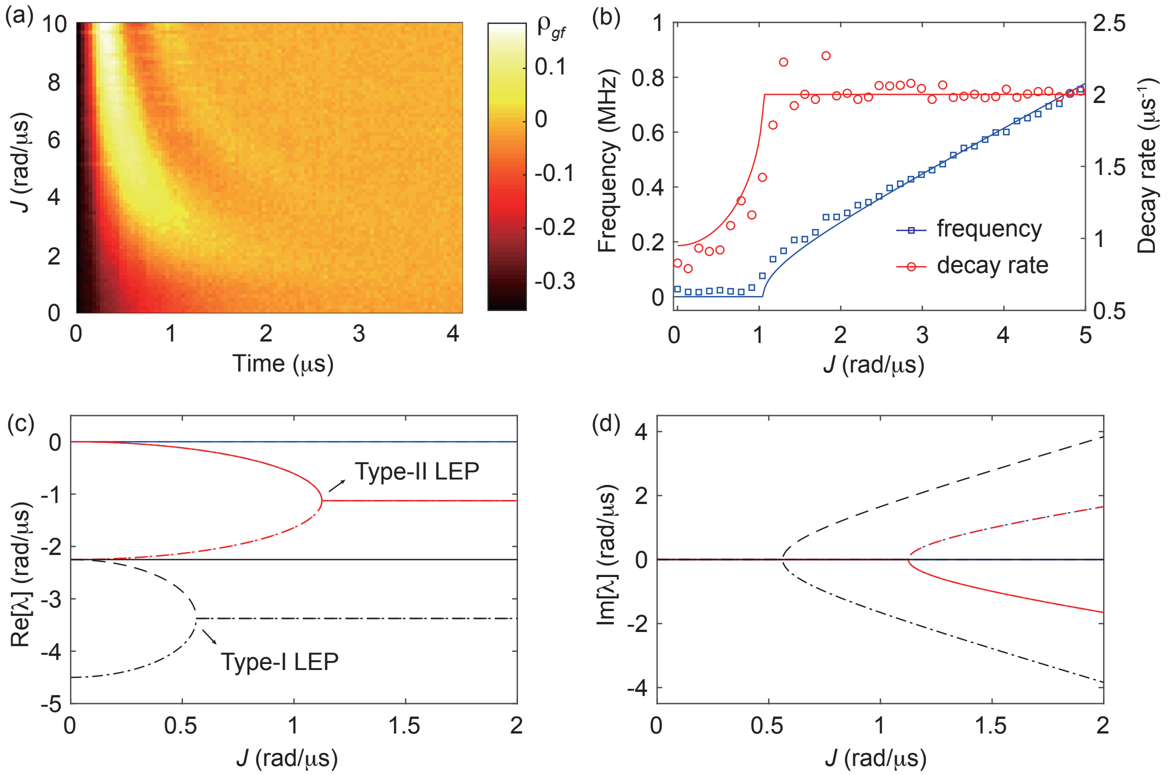

Fig. 3.20: (a) The system's evolution with different J measured with ρ_{gf}. (b) Frequency and decay rate extracted from panel a. (c) The imaginary part of the eigenvalues of the superoperator in Eq. 3.38. Two types of LEP are marked. (d) The real part of the eigenvalues of the superoperator in Eq. 3.38.

Chapter 4

Higher-Order exceptional points and shortcuts to adiabaticity

In this section, I will concentrate on presenting theoretical proposals and exploring possible avenues for further research. Initially, I will examine the four-level superconducting circuit introduced earlier, focusing on introducing a drive on the $|h\rangle$–$|f\rangle$ transition. Subsequently, I will investigate methods to accelerate the adiabatic process within these systems. Lastly, I will provide a brief overview of potential experiments involving exceptional rings in this context.

4.1 Introduction

In Sec. 3.6.1.1, we focused on dynamically encircling the EP through time-dependent parameter changes. The time dependence imposes limits on adiabatic evolution due to the presence of dissipation. The ideal behavior is expected to follow the instantaneous eigenvalues on the Riemann surfaces. To see what the topology suggests for the evolution of the system, we choose a parameter loop that encircles the EP, Fig. 4.1a. Then at a different point on this loop, we find the eigenvalues and eigenstates of the static Hamiltonian. The real and

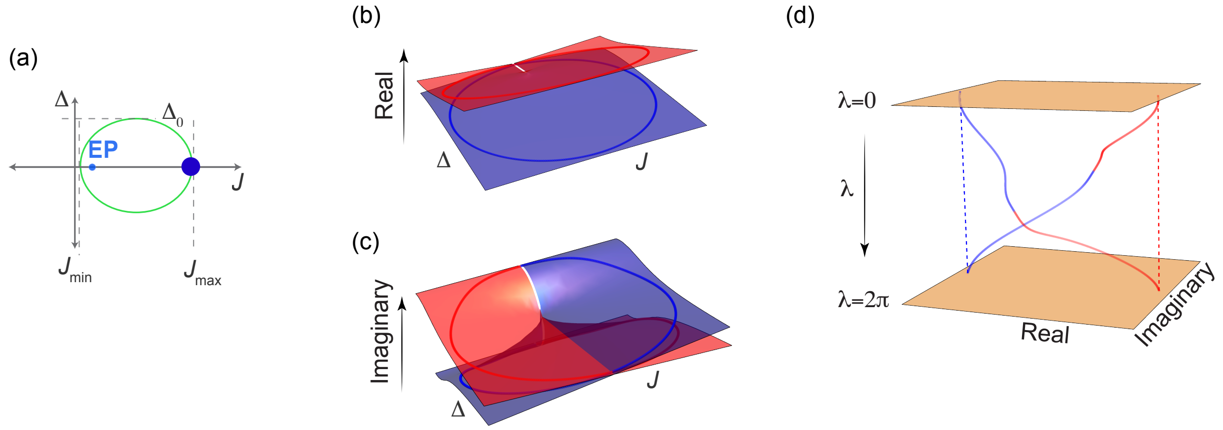

Fig. 4.1: (a) Schematics of encircling an EP. (b,c). The real (b) and imaginary (b) parts of the instantaneous eigenvalues of the Hamiltonian are plotted in terms of J and Δ. (d) State transfer shown as real and imaginary parts of the eigenvalues change with the loop in panel (a).

imaginary parts of the eigenvalues on the Riemann surfaces are shown in Fig. 4.1(b,c). The imaginary part is an extra degree of freedom that allows the eigenstates to switch without intersecting, Fig. 4.1d. In Fig. 4.1d, the two eigenvalues are color-coded with blue and red, and the dashed line represent the two eigenvalues at the beginning $\lambda = 0$ and end of the cycle $\lambda = 2\pi$, where each of the eigenvalues are smoothly transferred to the other at some point in the middle. However, realizing these processes is challenging, as we have seen in Sec. 3.6.1.1, where the eigenstates do not fully transfer to instantaneous eigenstates and show oscillations. Moreover, the mode switch only occurs in one direction and is not symmetric. However, since we need to continuously change the parameters in time as opposed to statically changing the parameters, we can employ methods including reverse engineering techniques, which we will introduce in the following sections. If we can address these challenges, we can harness more exciting phenomena by accessing to higher dimensional non-Hermitian systems. This chapter will focus on higher-order EP and the reserve engineering technique to harness them.

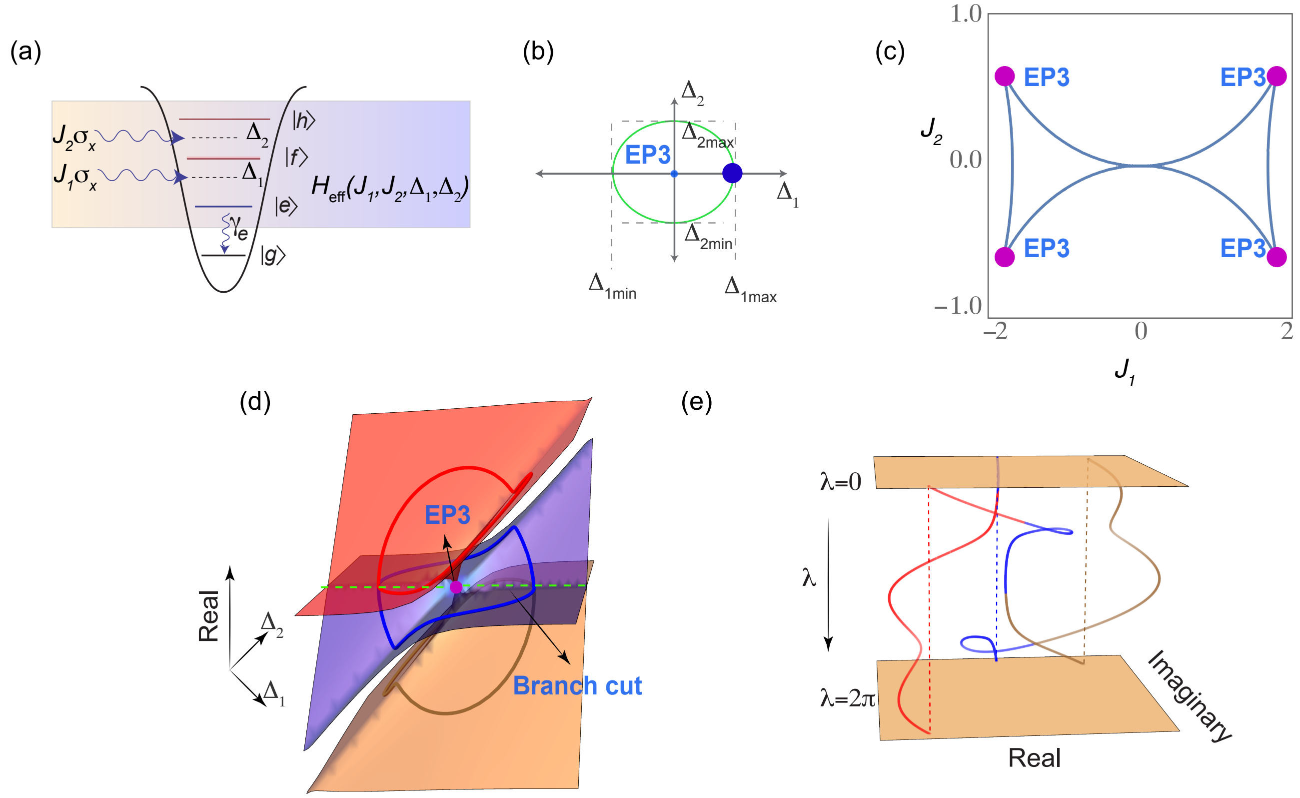

Fig. 4.2: (a) Schematics of the quantum system consisting of four energy states. (b) Schematics of encircling an EP3. (c) EP2 lines structure around EP3. (d) Riemann sheet topology around EP3, and two branch cuts that connect two pairs of sheets. (e) The eigenvalue braiding as a result of parametric change of the static parameters around EP3.

4.2 Higher dimensional non-Hermitian systems

The presence of exceptional points and complex energies allows us to study interesting and non-trivial topology [51]. One of these features is the study of different braid groups that braids different eigenstates while smoothly connecting them together. In two dimensional case, there are only 0-dimensional exceptional points, where a closed loop around this point smoothly connects the two eigenstates. However, by moving to a higher-dimensional system, we have structures of exceptional point, e.g., in a 3-dimensional case, the topology is a trefoil knot degeneracy [51]. These structures define different braid groups, where within that braid group, any close loop can be transformed to the other and result in the same eigenstate braiding. By increasing the number of energy states in the non-Hermitian Hamiltonian, we can permute more states by harnessing the topology of Riemann sheets. In this section, we harness the fourth level of the transmon qubit marked as $|h\rangle$ to observe higher dimensional degeneracies and EP2 structures. As it's shown in Fig. 4.2a, by post-selecting on the $\{|e\rangle, |f\rangle, |h\rangle\}$ manifold and allowing the first excited state $|e\rangle$ to have faster loss rate than $|f\rangle$ and $|h\rangle$, we have a 3×3 dimensional effective non-Hermitian Hamiltonian. We introduce an extra drive into the $\{|f\rangle, |h\rangle\}$ manifold where we achieve the following Hamiltonian:

$$H_0 = \begin{pmatrix} -i\gamma/2 + \Delta_1 & J_1 & 0 \\ J_1^* & \Delta_2 & J_2 \\ 0 & J_2^* & 0 \end{pmatrix} \tag{4.1}$$

where J_1 and J_2 are the coupling rate between $|e\rangle$–$|f\rangle$ and $|f\rangle$–$|h\rangle$ transition and Δ_1 and Δ_2 are the detuning of the drive from $|e\rangle$–$|f\rangle$ and $|f\rangle$–$|h\rangle$ transition, respectively. If we set $\gamma_e = 7$, this Hamiltonian has a third-order EP at $J_1 = \pm 7\sqrt{2/3}/3$, $J_2 = \pm 7/(6\sqrt{3})$, $\Delta_1 = 0$ and $\Delta_2 = 0$. The EP3s are shown with respect to variation of J_1 and J_2 in Fig. 4.1c as purple circles. These EP3s are connected by EP2 lines.

To locate the EP2 lines and EP3s, we can harness differential methods presented in [59]. To find the degeneracies of a differential equation of the form $\dddot{x} + p\ddot{x} + q\dot{x} + rx = 0$, we can first bring it to the matrix form below:

$$\frac{d}{dt}\begin{pmatrix} y_1 \\ y_2 \\ y_3 \end{pmatrix} = \begin{pmatrix} 0 & 1 & 0 \\ 0 & 0 & 1 \\ -r & -q & -p \end{pmatrix} \begin{pmatrix} y_1 \\ y_2 \\ y_3 \end{pmatrix}, \tag{4.2}$$

where $y_1 = x$, $y_2 = \dot{x}$, and $y_3 = \ddot{x}$. The characteristic equation is $\lambda^3 + p\lambda^2 + q\lambda + r = 0$. We can eliminate the λ^2 term without loss of generality:

$$\lambda'^3 + A\lambda' + B = 0. \tag{4.3}$$

Any perturbation to A and B will result in lifting the degeneracies of the Hamiltonian. For this matrix, if both $A = 0$ and $B = 0$, we have a three-fold degeneracy. And if the discriminant of the Matrix is zero, we have lines of two-fold degeneracies. Note that for a third-order polynomial, the discriminant is $4A^3 - 27B^2$.

Following the same method, we can transform the Hamiltonian in Eq. 4.1 into the form of Eq. 4.3 and find the EP3 and EP2 lines. In order to do that we solve for the eigenvalues of the Hamiltonian and write the characteristic equation:

$$\lambda^3 + (\frac{7i}{2} - \Delta_1 - \Delta_2)\lambda^2 + (-J_1^2 - J_2^2 - 7i\frac{\Delta_2}{2} + \Delta_1\Delta_2)\lambda - \frac{7iJ_2^2}{2} + J_2^2\Delta_1, \tag{4.4}$$

where we extract the coefficient of the characteristic equation and find A and B for this Hamiltonian:

$$A = -J_1^2 - J_2^2 - \frac{7i\Delta_2}{2} + \Delta_1\Delta_2 - \frac{1}{12}(-7i + 2\Delta_1 + 2\Delta_2)^2, \tag{4.5}$$

and

$$B = \frac{1}{108}(-18J_1^2(-7i + 2\Delta_1 + 2\Delta_2) + (-7i + 2\Delta_1 - \Delta_2)(49 + 36J_2^2 \\ - 4\Delta_1^2 - 14i\Delta_2 + 8\Delta_2^2 + 4\Delta_1(7i + \Delta_2))). \quad (4.6)$$

After finding exceptional point structure in Fig. 4.2c, we can start by encircling one of the EP3s. The EP3 can be encircled by choosing a parameter loop around it. However, any loop enclosing this degeneracy in J_1 and J_2 parameter space would necessarily intersect with an EP2 line. So, the simplest choice of parameter loop is by changing Δ_1 and Δ_2 at fixed $J_1 = \pm((7\sqrt{2/3})/3)$, $J_2 = \pm(7/(6\sqrt{3}))$, Fig. 4.2b. The form of the loop is:

$$\Delta_1(\lambda) = 3\sin(2/9\pi + 2\pi\lambda/T), \quad (4.7)$$

$$\Delta_2(\lambda) = 3\cos(2/9\pi + 2\pi\lambda/T), \quad (4.8)$$

where λ is a parameter that changes the loop. Note that we need to make sure there is no degeneracy in the loop other than the select EP3. For real detuning values, there are no EP2 lines or EP3 in this parameter space. We can look at the instantaneous eigenvalues of the loop on the Riemann surfaces surrounding this degeneracy, Fig 4.2d. The Riemann topology is associated with the three eigenvalues of this Hamiltonian. Here, there are two branch cuts that connect two pairs of Riemann sheets and allow for a smooth transition between the eigenstates over a loop. By looking at the evolution of the real and imaginary parts of the instantaneous eigenvalues as λ is evolving, we can observe that three states permute. Figure 4.2e shows the starting and final points of the closed loop with two orange planes; each eigenvalue is color-coded similar to the Riemann surface in Fig. 4.2d. We can see that none of the colors return to the initial state—the initial state is shown with dashed lines.

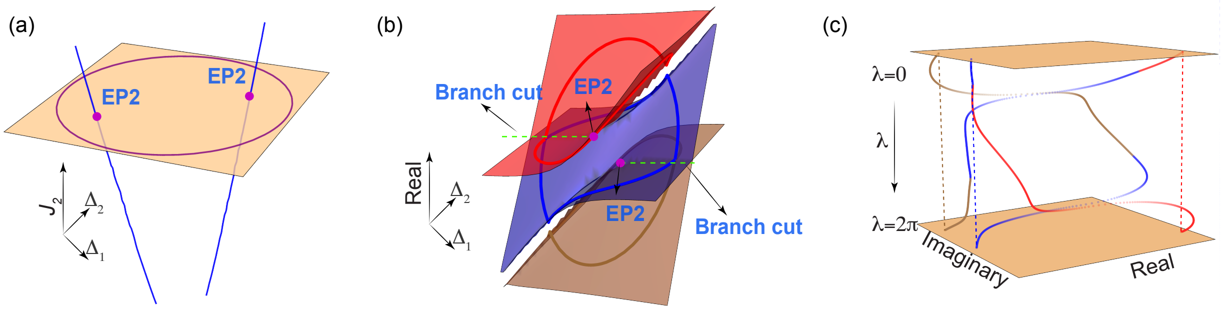

Fig. 4.3: (a) Parameter loop around two EP2 lines, when $J_1 = 7\sqrt{2/3}/3$ and $J_2 = 2$. The EP2 lines are shown in the space of Δ_1, Δ_2 and J_2. (b) Riemann topology for a different Δ_1, Δ_2 and constant $J_1 = 7\sqrt{2/3}/3$ and $J_2 = 2$. The blue sheet intersects with two different sheets where the EP2 is located. (c) The eigenvalue braiding is a result of a parametric change of the static parameters around two EP2.

Braiding the eigenvalues can be done with EP2 lines as well. The EP2 lines allow us to select the eigenstates we want to braid. Figure 4.3 is an example of encircling two EP2s. Here, I chose a fixed value for $J_1 = 7\sqrt{2/3}/3$, and vary the three parameters Δ_1, Δ_2 and J_1 to find the regions where the discriminant is zero. Figure 4.3a shows two EP2 lines intersecting with a plane with constant $J_2 = 2$. To encircle both EP2s, the following loop can be employed:

$$\Delta_1(\lambda) = 8\sin\left(2/9\pi + 2\pi\lambda/T\right). \tag{4.9}$$

$$\Delta_2(\lambda) = 8\cos\left(2/9\pi + 2\pi\lambda/T\right). \tag{4.10}$$

The instantaneous eigenvalues of the Hamiltonian for this parameter loop are shown on Riemann topology, Fig. 4.3b. The two EP2s are connecting two different sheets and different points. The braiding of the eigenvalues as a result of this encircling is shown in Fig. 4.3c, where all three eigenvalues permute similarly to the EP3 encircling.

By choosing a different loop in Fig. 4.3a, we can encircle only one of the EP2 lines. This

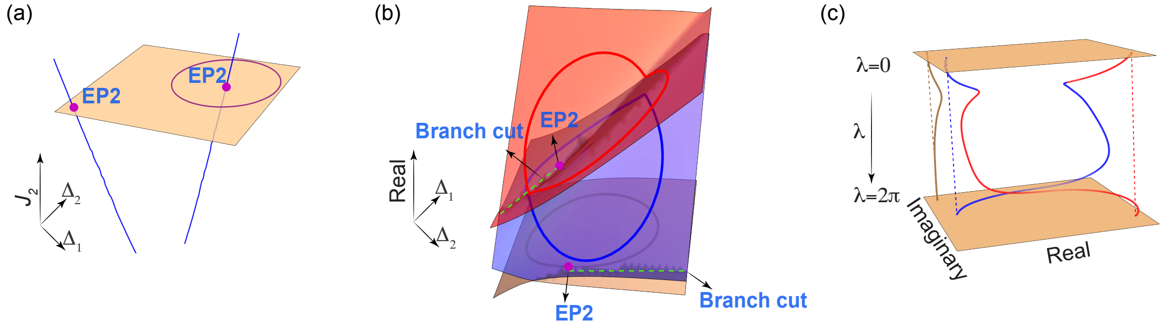

Fig. 4.4: (a) Parameter loop around one EP2 line, when $J_1 = 7\sqrt{2/3}/3$ and $J_2 = 2$. The EP2 lines are shown in the space of Δ_1, Δ_2, and J_2. (b) Riemann topology for a variable Δ_1, Δ_2 and constant $J_1 = 7\sqrt{2/3}/3$ and $J_2 = 2$. The blue sheet intersects with two different sheets where the EP2 is located. (c) The eigenvalue braiding as a result of a parametric change of the static parameters around one EP2.

loop is shown in Fig. 4.4a, where:

$$\Delta_1(\lambda) = 4\sin\left(2/9\pi + 2\pi\lambda/T\right) + 4. \tag{4.11}$$

$$\Delta_2(\lambda) = 4\cos\left(2/9\pi + 2\pi\lambda/T\right) + 4. \tag{4.12}$$

The instantaneous eigenvalues corresponding to the loop are shown on the Riemann topology for fixed values of $J_1 = 7\sqrt{2/3}/3$ and $J_2 = 2$. Only blue and red traces cross the branch cut and the brown trace stays on the same sheet. The evolution of the three eigenvalues over this parametric loop is shown in Fig. 4.4c, where only two eigenvalues are exchanged. We can choose our loop in a way that exchanges blue and brown or brown and red eigenvalues by properly encircling the EP2 of interest. Moreover, if we choose an area in Fig. 4.4a that does not encircle any EP2 lines, we observe that none of the eigenvalues evolve into another.

4.2.1 Experimental feasibility

Harnessing the topology discussed above is challenging due to the presence of dissipation. We have only studied the parametric change of the Hamiltonian so far, where no evolution has been considered. In the case of EP2 in $|e\rangle$–$|f\rangle$ manifold, we experimentally observed the difference between the instantaneous eigenvalues and the adiabatic evolution under the time-dependent Hamiltonian.

4.3 Counterdiabatic drive

So far, we have explored adiabatic processes, where the presence of dissipation imposes limitations on their efficiency. Due to dissipation, we have seen that the system cannot follow the instantaneous eigenstates, which results in non-adiabatic coupling and deviation from the desired adiabatic path. This means that we cannot harness the interesting topology of non-Hermitian systems. To overcome this challenge, we take a different approach toward adiabaticity that allows faster evolution in shorter durations that mimics the behavior of an adiabatic process. We look at a reverse engineering method to introduce an additional drive, known as a counter-diabatic drive. This process is also known as a shortcut to adiabaticity [60, 61]. These methods still allow us to use the invariants associated with adiabatic processes, such as Berry phase. In this chapter, I follow the paper [61] Consider a Hamiltonian with the time-dependant parameters $H_0(t)$, that undergoes adiabatic processes. We aim to find additional terms to this Hamiltonian $H_1(t)$ that speed up $H_0(t)$ evolution. We have a total Hamiltonian:

$$H(t) = H_0(t) + H_1(t), \tag{4.13}$$

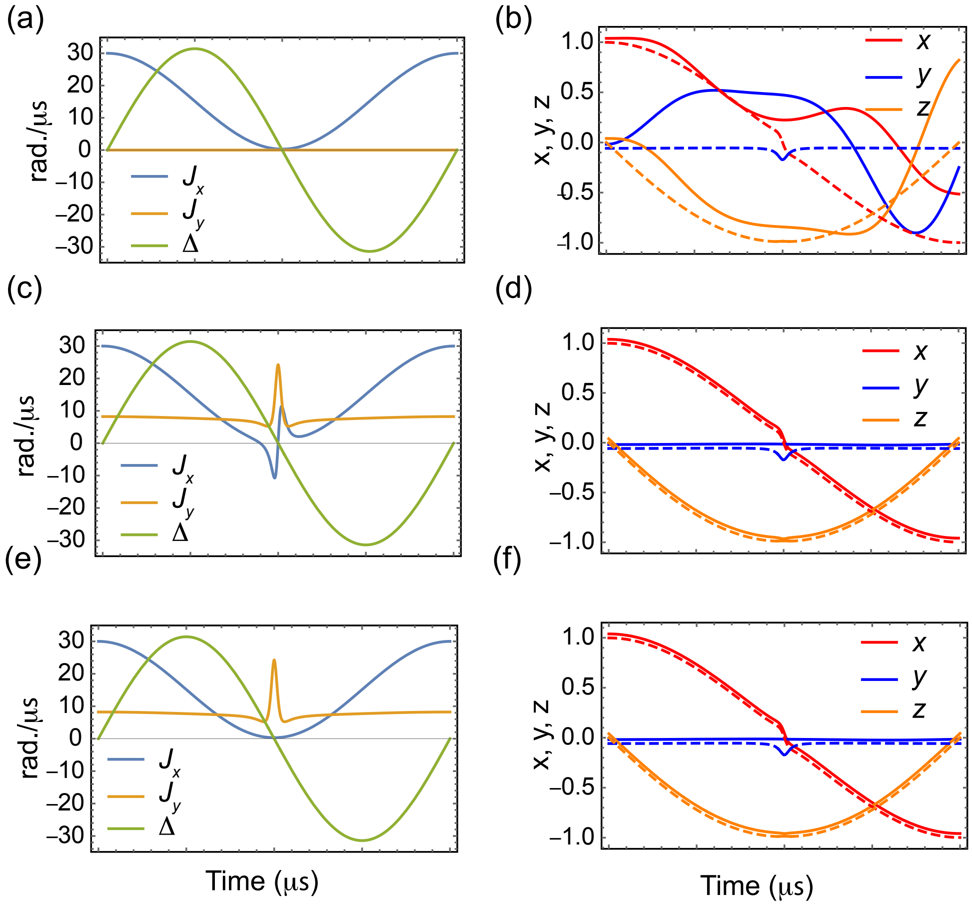

Fig. 4.5: (a) The encircling loop for $H_0(t)$, where Δ and J_x are varied in 0.2 μs. (b) The resulted evolution of encircling an EP with the loop in panel (a). (c) The parameter change in total Hamiltonian after adding H_1. (d) The evolution resulted from encircling an EP with the loop in panel (c). (e) The parameter change in total Hamiltonian after adding H_1 and eliminating the non-Hermitian terms. (f) The evolution resulted from encircling an EP with the loop in panel (e).

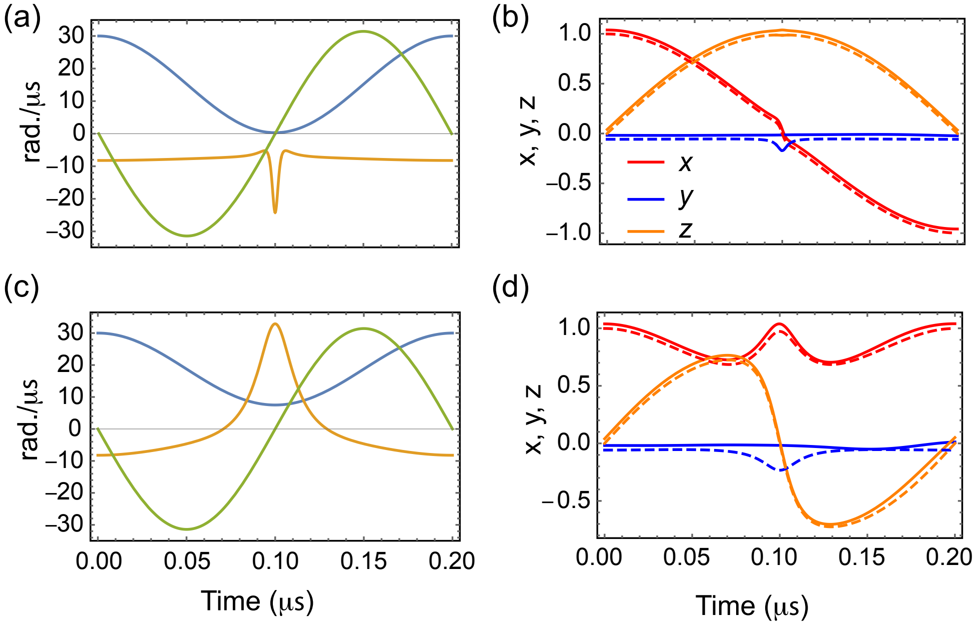

Fig. 4.6: (a) The parameter change in total Hamiltonian after adding H_1 and eliminating the non-Hermitian terms for encircling loop in the opposite direction. (b) The evolution resulted from encircling an EP with the loop in panel (a). (c) The parameter change in total Hamiltonian after adding H_1 and eliminating the non-Hermitian terms for a closed loop in the opposite direction with no EP inside the loop. (d) The evolution resulted from a closed loop with no EP is shown in panel (c).

where

$$H_1(t) = i\sum_n [|\partial_t n(t)\rangle\langle\hat{n}(t)| - \langle\hat{n}(t)|\partial_t n(t)\rangle|n(t)\rangle\langle\hat{n}(t)|], \tag{4.14}$$

where $|n(t)\rangle$ are the instantaneous eigenstates of the $H_0(t)$.

Let's consider encircling an EP2 for an effective non-Hermitian system in $|e\rangle$–$|f\rangle$ manifold. In this case, we have:

$$H_0(t) = \begin{pmatrix} i\gamma/2 + \Delta(t) & J(t) \\ J(t) & 0 \end{pmatrix}. \tag{4.15}$$

Where $\gamma = 7$ rad./μs, $J(t) = (30 - 0.3)\cos(2\pi t/T) + 0.3$ $\Delta(t) = \pm 30\sin(2\pi t/T)$, Fig. 4.5a. Under $H_0(t)$, the 2 μs evolution is shown in Fig. 4.5b, which does not follow the instantaneous eigenstate (shown in dashed lines). So, we introduce $H_1(t)$ to this Hamiltonian, which changes the parameters variation by adding a $J_y(t)$ variation as well as a deformation in $\Delta(t)$ variation near EP, Fig. 4.5c[1]. The evolution under the total Hamiltonian is shown in Fig. 4.5d, which closely follows the instantaneous eigenstates and undergoes a perfect state transfer as suggested by Riemann's topology. However, after $H_1(t)$ addition, the Hamiltonian has some non-Hermitian contribution that cannot be realized in the experiment. To eliminate the non-Hermitian contribution, I substitute $H_1(t)$ with $(H_1(t) + H_1^\dagger(t))/2$, which results in a different parameter loop that is purely Hermitian, Fig. 4.5e. This change does not affect the evolution since the non-Hermitian contribution is not large, Fig. 4.5f. Another interesting effect is that the state transfer does not depend on the direction of evolution anymore. The parameter change for the opposite direction of detuning is shown in Fig. 4.6a, along with its corresponding evolution in Fig. 4.6b. Finally, if we do not encircle the EP, we expect the system to return to the initial state. Figure 4.6c is an example of a loop that does not encircle

---

[1] Note that H_1 includes non-Hermitian contributions, which result in the upper off-diagonal elements not being the complex conjugates of the lower off-diagonal elements. In the remainder of this section, I will primarily concentrate on examining the upper off-diagonal elements.

the EP with $J(t) = (30 - 7.25)\cos(\pi t/T) + 7.25$. The evolution under this closed loop is shown in Fig. 4.6d, where the state returns to the initial state. Note that the expectation values are shifted by a slight amount from the instantaneous eigenstate for clarity.

We learned that a counter-diabatic drive works for EP2 in a two-level non-Hermitian system. Here, we apply this counter-diabatic method to EP3. Let's consider a non-Hermitian Hamiltonian of this form:

$$H_0 = \begin{pmatrix} -i\gamma/2 + \Delta_1 & J_1 & 0 \\ J_1^* & \Delta_2 & J_2 \\ 0 & J_2^* & 0 \end{pmatrix}, \tag{4.16}$$

where $J_1 = \pm 7\sqrt{2/3}/3$, $J_2 = \pm 7/(6\sqrt{3})$ and $\Delta_1(t) = 20\sin(2\pi t/T + \phi_0)$ and $\Delta_2(t) = 20\cos(2\pi t/T + \phi_0)$, Fig. 4.7a. By adding $H_1(t)$ to this Hamiltonian, we observe that some time-dependent contribution is added to J_{1x} as shown in Fig. 4.7 as well as J_{1y} and J_{2y} as shown in Fig. 4.7c. The evolution of the system in 0.2 μs is shown in Fig. 4.7d,e,f for different eigenstates of the Hamiltonian at $t = 0$. The evolution is then projected on the instantaneous eigenstates of $H_0 t$. The three plots in panel (d,e,f) show that the state evolves on the instantaneous eigenstates and go through branch cuts at points where the color of the evolution changes to another eigenstate. For example, for panel d, the system starts at the eigenstate that is color-coded in blue and evolves until it reaches a branch cut and moves to the eigenstate color-coded with brown. For all these three cases, the starting points are the same, but the initial states are different.

However, the evolution in Fig. 4.7(b,c) has non-Hermitian contributions which can be eliminated by substituting $H_1(t)$ with $(H_1(t) + H_1^\dagger(t))/2$. The result of the parameter variation after adding this contribution is shown in Fig. 4.8(b,c), where the original parameter variation stays comparatively intact, while J_{1y} and J_{2y} (shown in Fig. 4.8c) have the same form as the case with the non-Hermitian contribution in Fig. 4.8c. The evolution under this

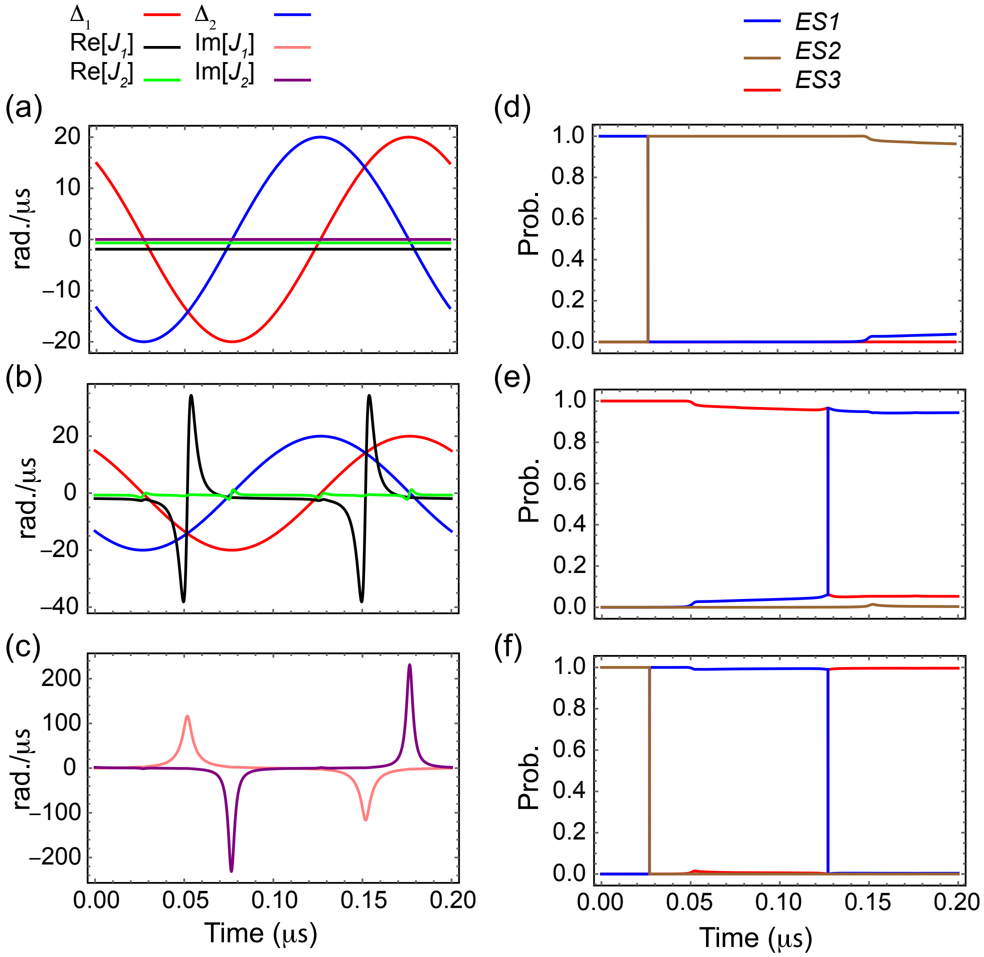

Fig. 4.7: (a) The encircling loop for $H_0(t)$, where Δ_1 and Δ_2 are varied in 0.2 μs. (b) The parameter variation in total Hamiltonian after adding $H_1(t)$ in J_{1x}, J_{2x}, Δ_1, Δ_2. (c) The parameter variation in total Hamiltonian after adding $H_1(t)$ in J_{1y}, J_{2y}. (d,e,f). The evolution under parameter change in panels (b,c) with three initial eigenstates. The evolution is projected on instantaneous eigenstates of the total Hamiltonian.

Hamiltonian is not completely following the instantaneous eigenstates and has some extra features and lower fidelity.

This study simulates the experimental setup used in the non-Hermitian circuit with four-level and shows promising results for experimental observation. Some aspects of this work need further study, including the study of invariants, such as the Berry phase and its dependence on noise from the environment with counter-diabatic drive. Moreover, the potential application of this topology with short-time evolution is an important part of this study that needs further exploration.

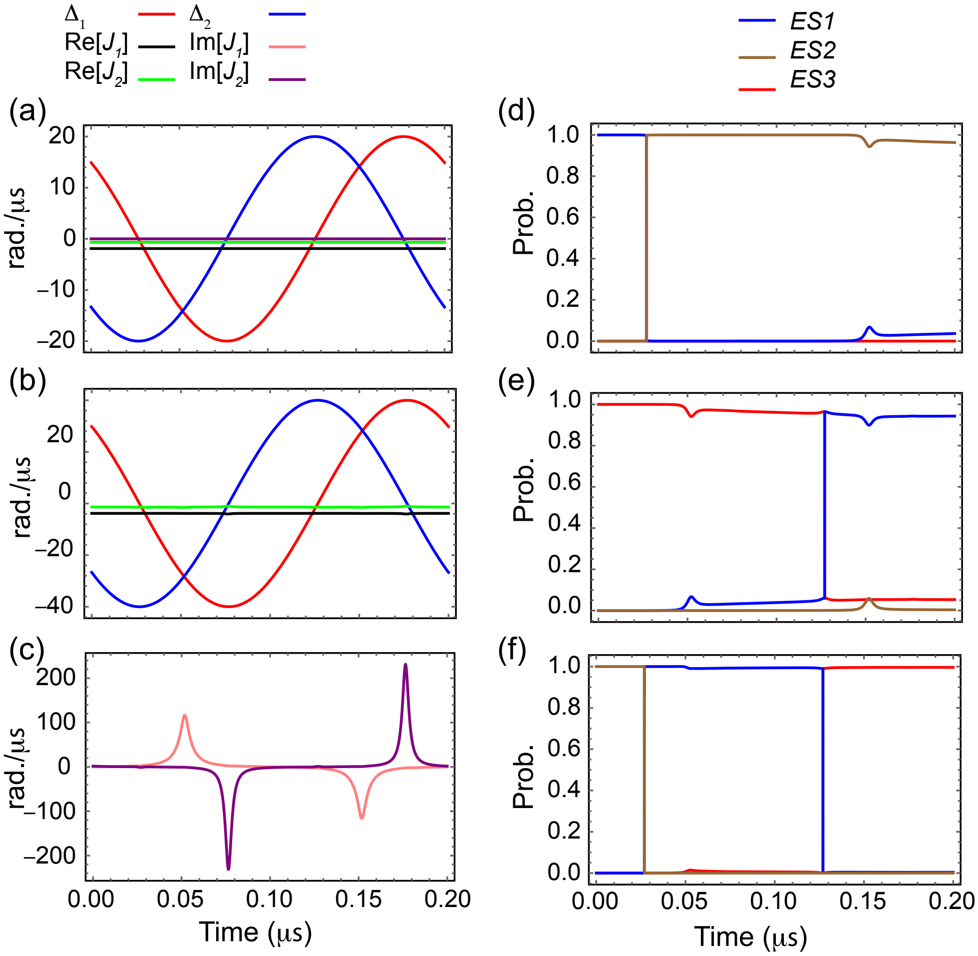

Fig. 4.8: (a) The encircling loop for $H_0(t)$, where Δ_1 and Δ_2 are varied in 0.2 μs. (b) The parameter variation in total Hamiltonian after adding $H_1(t)$ in J_{1x}, J_{2x}, Δ_1, Δ_2. (c) The parameter variation in total Hamiltonian after adding $H_1(t)$ in J_{1y}, J_{2y}. (d,e,f). The evolution under parameter change in panels (b,c) with three initial eigenstates. The evolution is projected on instantaneous eigenstates of the total Hamiltonian.

4.4 Exceptional ring

In the previous section, we learned that the exceptional point has a structure in higher-dimensional spaces. However, in two-dimensional space, we can still create a space of exceptional points. One example of this case is the exceptional ring that has been studied in [62]. In this work, they discuss the adiabatic transport of the system on an exceptional ring and study the accumulated phase. They show that the accumulated phase on the eigenstate of the system grows as a square root dependence in time and accumulates a π Berry phase.

The Hamiltonian describes the exceptional ring:

$$H_{\mathbf{ring}} = \begin{pmatrix} i\gamma/4 & Je^{-i\phi} \\ Je^{i\phi} & -i\gamma/4 \end{pmatrix}, \tag{4.17}$$

where ϕ is in the range $[0,2\pi]$. Setting $J = \gamma/4$ makes this Hamiltonian describing an exceptional ring. [62]. The eigenstate of this Hamiltonian is:

$$|v\rangle = \begin{pmatrix} 1 \\ -ie^{i\phi} \end{pmatrix}. \tag{4.18}$$

We can transport this state on the exceptional ring by varying the phase ϕ linearly in time:

$$\phi(t) = 2\pi t/T, \tag{4.19}$$

where T is the period of the loop. By measuring the phase at the end of the loop and varying the period T, we acquire a phase of the form:

$$\chi = \sqrt{-i\pi\gamma T/2} - \pi, \tag{4.20}$$

where the first term is the dynamical phase and the second is the Berry phase.

This system can be realized experimentally by either varying the phase of the drive linearly with time or use the following equality:

$$Je^{i2\pi t/T} = J\sin(2\pi t/T) + iJ\cos(2\pi t/T), \tag{4.21}$$

which can be interpreted as addition of the two pulse modulated with a sine-shaped amplitude. Since J_x and J_y components of the drive have $\pi/2$ phase difference, the desired pulse can be constructed by adding $J_x = J$ modulated with $\sin(2\pi t/T)$ and $J_y = iJ$ modulated with $\cos(2\pi t/T)$.

This work can reveal the interesting topological features of the exceptional points and harness their potential robustness in the presence of noise. However, this experiment needs to examine long time evolution, which makes the success rate low. To observe the square root behavior and fit the data, the short time duration resembles linear dependence, and only in longer time durations the asymptotic behavior reveals the square root dependence.

4.5 Future Work

The study of non-Hermitian systems and their exceptional points can be extended to systems with more qubits. We can engineer coupled non-Hermitian qubits to realize quantum bath engines and higher-order exceptional points. In multi-qubit systems, the non-Hermiticity can have effects on the entanglement generation as well. In the paper [63], in collaboration with Prof. Brigitta Whaley's group, we showed that by proximity to the exceptional point, the entanglement could be established in time scales much faster than Hermitian systems. Moreover, understanding the thermodynamics of these systems can give us insight into the quantum thermodynamics in open quantum systems. Moreover, future works will benefit from a 2D design where the number of qubits can be easily scaled, and more robust and controllable bath engineering techniques can be implemented.

APPENDICES

Appendix A

Mathematica Simulations

In this appendix I included an example of solving non-Hermitian evolution when encircling an exceptional point. First, I define the variables and Hamiltonian and its corresponding eigenvalues and eigenstates. Then plot the time-dependent parameters. Next, I solve the Lindblad master equation and extract the state of the qubit from the density matrix solution. finally I plotted the evolution and the Riemann surface corresponding to the eigenvalues.

Encircling the exceptional point:

Variables :

```
In[1]:= δ = -10 Pi;
        γ = 6.2;
        p = 1.5;
        x = 1;
        j = 1;
        a = 30;
        δ0 = 0;
        Clear[J];
        γ2 = 0.35;
        b = 1 * (1 + .01);
        h = 1;
```

General density matrix:

```
In[2]:= ρ[t_] :=
          {{ρ11[t], ρ12[t], ρ13[t]}, {ρ21[t], ρ22[t], ρ23[t]}, {ρ31[t], ρ32[t], ρ33[t]}};
```

Hamiltonian at $t = 0$:

```
In[3]:= Hc[t_] := {{0, 0, 0}, {0, -ⅈ γ / 2 + x * δ * Sin[0 * 2 * h * Pi * 1 / p + δ0],
           J * ((2 - b) * Cos[0 * 2 * Pi * 1 / p + δ0] + b) / 2},
          {0, J * ((2 - b) * Cos[0 * 2 * Pi * 1 / p + δ0] + b) / 2, -x * δ * Sin[0 * 2 * Pi * 1 / p + δ0] + 0}}
```

Find eigenvalues and eigenstates :

```
In[4]:= {vals, vecs} = Eigensystem[Hc[t]];
```

Normalize the eigenvalues and eigenstates :

```
In[5]:= vecs[[3]] = Normalize[vecs[[3]]];
        vecs[[2]] = Normalize[vecs[[2]]];
```

Time – dependent Hamiltonian :

```
In[7]:= Hc[t_] := {{0, 0, 0},
           {0, x * δ / 2 * Sin[t * 2 * Pi * 1 * h / p + δ0], J * ((2 - b) * Cos[t * 2 * Pi * 1 / p + δ0] + b) / 2},
           {0, J * ((2 - b) * Cos[t * 2 * Pi * 1 / p + δ0] + b) / 2, -x * δ / 2 * Sin[t * 2 * Pi * 1 / p + δ0]}};
```

Non – Hermitian Time – dependent Hamiltonian :

```
In[8]:= Hc22[t_] := {{0, 0, 0}, {0, -ⅈ γ / 2 + x * δ / 2 * Sin[t * 2 * Pi * 1 / p + δ0],
            J * ((2 - b) * Cos[t * 2 * Pi * 1 / p + δ0] + b) / 2},
           {0, J * ((2 - b) * Cos[t * 2 * Pi * 1 / p + δ0] + b) / 2, -x * δ / 2 * Sin[t * 2 * Pi * 1 / p + δ0]}};
```

Eigenvalues and Eigenstates of the non – Hermitian Time – dependent Hamiltonian :

```
In[9]:= {vals22, vecs22} = Eigensystem[Hc22[t]] /. J → a /. δ → 5 Pi;
```

Eigenvalues and Eigenstates of the Time – dependent Hamiltonian :

```
In[10]:= {vals1, vecs1} = Eigensystem[Hc[t]] /. J → a /. δ → 5 Pi;
         vecs1[[3]] = Normalize[vecs1[[3]]];
         vecs1[[2]] = Normalize[vecs1[[2]]];
```

Parameter loop :

```
In[13]:= delta = x * δ / 2 * Sin[t * h * Pi * 1 * 2 / p + δ0];
         jey = a * ((2 - b) * Cos[t * 2 * Pi * 1 / p + δ0] + b) / 2;
```

Exceptional point location for comparison with different points during the loop :

```
In[14]:= γf = γ / 4 * t / t; γf2 = -γ / 4 * t / t;
```

Plotting the parameters and comparing with *J* value of the EP :

```
In[15]:= Plot[{delta, jey, γ / 4, γf2}, {t, 0, p}, PlotRange → All]
```

Out[15]=

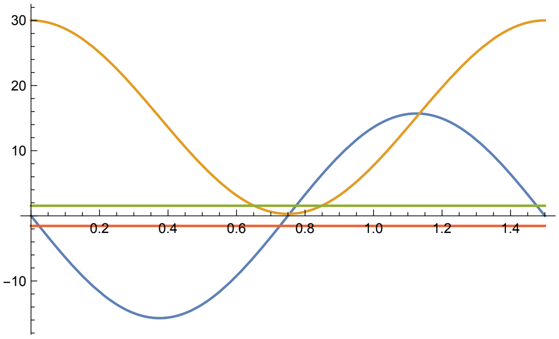

Visualizing the parameter loop :

```
In[16]:= ListPlot[{Table[{jey, delta}, {t, 0, p, 0.001}], Table[{γf, 0}, {t, 0, p, 0.01}],
           Table[{γf2, 0}, {t, 0, p, 0.01}]}, PlotRange → All, Axes → False, PlotStyle →
           {{Blue, PointSize[Small]}, {Red, PointSize[Large]}, {Black, PointSize[Large]}}]
```

Out[16]=

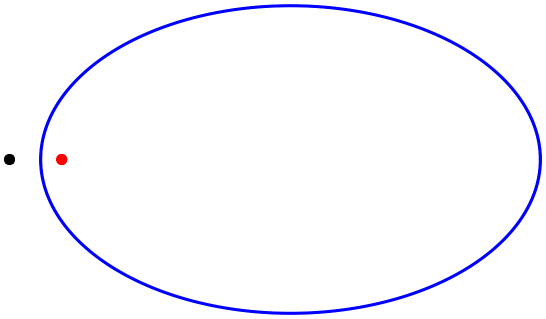

Defining the two Lindblad dissipators γ_e and γ_f :

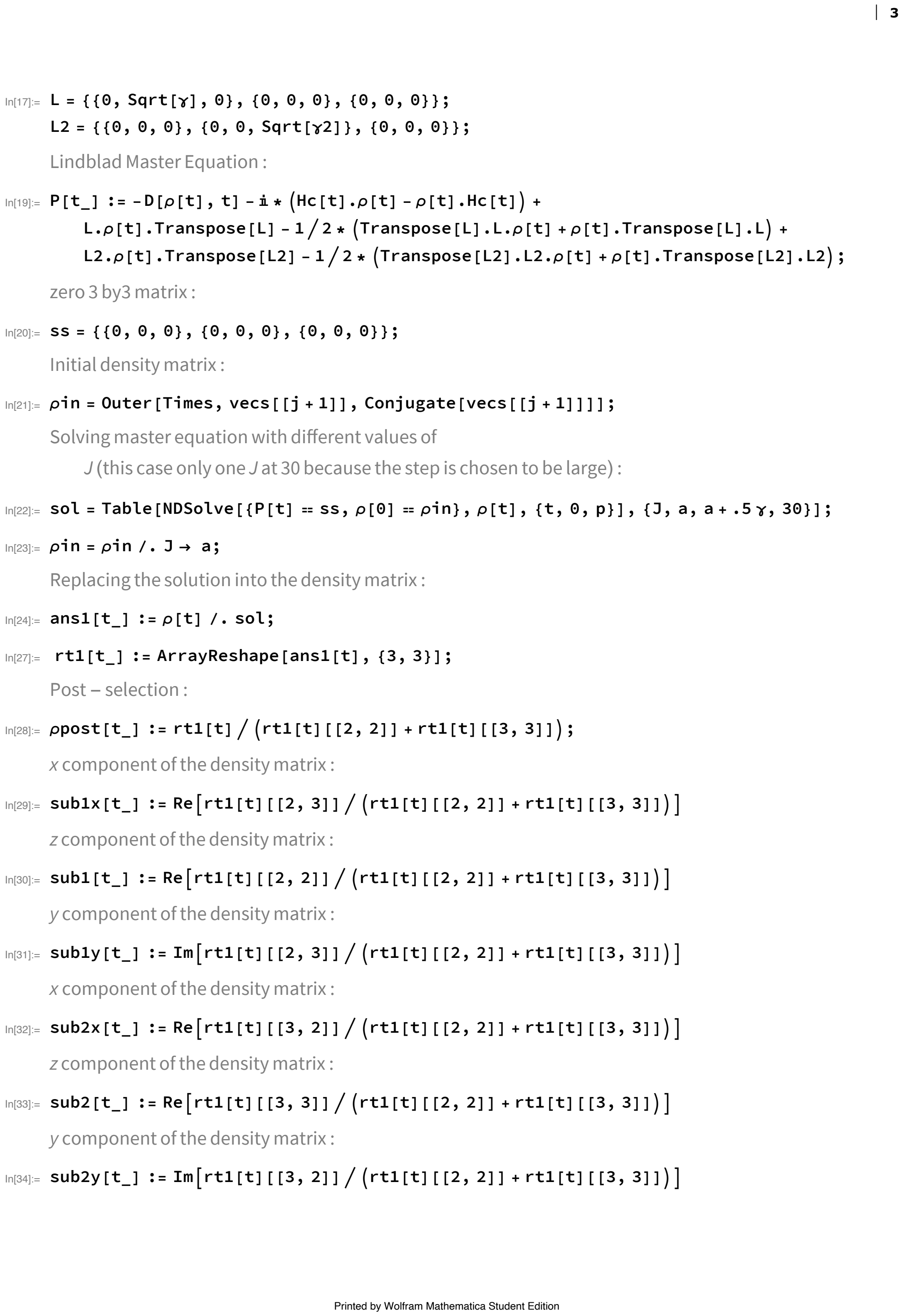

```
In[17]:= L = {{0, Sqrt[γ], 0}, {0, 0, 0}, {0, 0, 0}};
         L2 = {{0, 0, 0}, {0, 0, Sqrt[γ2]}, {0, 0, 0}};
```

Lindblad Master Equation :

```
In[19]:= P[t_] := -D[ρ[t], t] - ⅈ * (Hc[t].ρ[t] - ρ[t].Hc[t]) +
            L.ρ[t].Transpose[L] - 1 / 2 * (Transpose[L].L.ρ[t] + ρ[t].Transpose[L].L) +
            L2.ρ[t].Transpose[L2] - 1 / 2 * (Transpose[L2].L2.ρ[t] + ρ[t].Transpose[L2].L2);
```

zero 3 by3 matrix :

```
In[20]:= ss = {{0, 0, 0}, {0, 0, 0}, {0, 0, 0}};
```

Initial density matrix :

```
In[21]:= ρin = Outer[Times, vecs[[j + 1]], Conjugate[vecs[[j + 1]]]];
```

Solving master equation with different values of *J* (this case only one *J* at 30 because the step is chosen to be large) :

```
In[22]:= sol = Table[NDSolve[{P[t] == ss, ρ[0] == ρin}, ρ[t], {t, 0, p}], {J, a, a + .5 γ, 30}];

In[23]:= ρin = ρin /. J → a;
```

Replacing the solution into the density matrix :

```
In[24]:= ans1[t_] := ρ[t] /. sol;

In[27]:=  rt1[t_] := ArrayReshape[ans1[t], {3, 3}];
```

Post – selection :

```
In[28]:= ρpost[t_] := rt1[t] / (rt1[t][[2, 2]] + rt1[t][[3, 3]]);
```

x component of the density matrix :

```
In[29]:= sub1x[t_] := Re[rt1[t][[2, 3]] / (rt1[t][[2, 2]] + rt1[t][[3, 3]])]
```

z component of the density matrix :

```
In[30]:= sub1[t_] := Re[rt1[t][[2, 2]] / (rt1[t][[2, 2]] + rt1[t][[3, 3]])]
```

y component of the density matrix :

```
In[31]:= sub1y[t_] := Im[rt1[t][[2, 3]] / (rt1[t][[2, 2]] + rt1[t][[3, 3]])]
```

x component of the density matrix :

```
In[32]:= sub2x[t_] := Re[rt1[t][[3, 2]] / (rt1[t][[2, 2]] + rt1[t][[3, 3]])]
```

z component of the density matrix :

```
In[33]:= sub2[t_] := Re[rt1[t][[3, 3]] / (rt1[t][[2, 2]] + rt1[t][[3, 3]])]
```

y component of the density matrix :

```
In[34]:= sub2y[t_] := Im[rt1[t][[3, 2]] / (rt1[t][[2, 2]] + rt1[t][[3, 3]])]
```

```
In[35]:= zex = sub1[t] - sub2[t];
         xex = sub1x[t] + sub2x[t];
         yex = - sub1y[t] + sub2y[t];
```

Quantum state tomography during the evolution :

```
In[36]:= Plot[{Evaluate[sub1[t] - sub2[t]],
           Evaluate[sub1x[t] + sub2x[t]], Evaluate[-sub1y[t] + sub2y[t]]},
          {t, 0, p}, PlotRange → All, AxesLabel → {time, prob}, PlotLegends →
           Placed[{"sigma_z", "sigma_x", "sigma_y"}, {Scaled[{0, .8}], {0, 0.5}}]]
```

Out[36]=

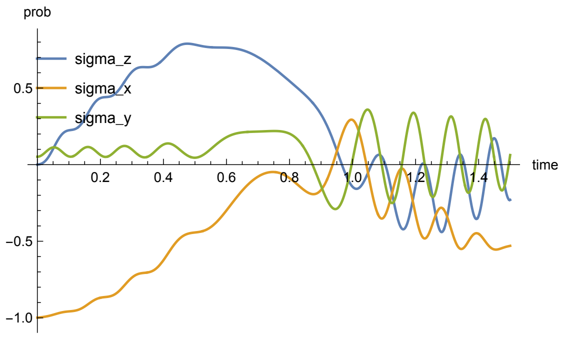

Defining *a* static non – Hermitian Hamiltonian :

```
In[•]:= Hc3[t_] := {{0, 0, 0}, {0, δp - ⅈ γ/2, Jp}, {0, Jp, 0 - δp}};
```

```
In[37]:= {eval, evec} = Eigensystem[Hc3[t]];
```

Riemann surface of the real part of the eigenvalues of the static non – Hermitian Hamiltonian in terms of *J* and Δ :

```
In[40]:= Plot3D[{Re[eval[[2]]], Re[eval[[3]]]}, {Jp, 0, a}, {δp, -12 Pi, 12 Pi},
          PlotStyle → {Directive[Yellow, Specularity[White, 20], Opacity[0.6]],
            Directive[Blue, Specularity[White, 20], Opacity[0.6]]}, Mesh → None]
```

Out[40]=

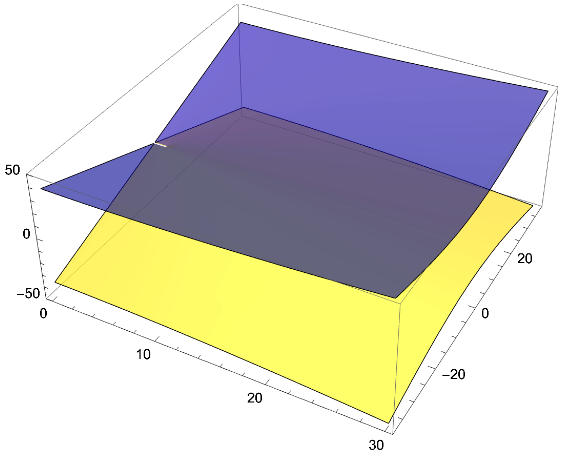

Riemann surface of the Imaginary part of the eigenvalues of the static non − Hermitian Hamiltonian in terms of *J* and Δ :

```
In[41]:= Plot3D[{Im[eval[[2]]], Im[eval[[3]]]}, {Jp, -3, a + 3}, {δp, -12 Pi, 12 Pi},
          PlotStyle → {Directive[Yellow, Specularity[White, 20], Opacity[0.6]],
            Directive[Blue, Specularity[White, 20], Opacity[0.6]]}, Mesh → None]
```

Out[41]=

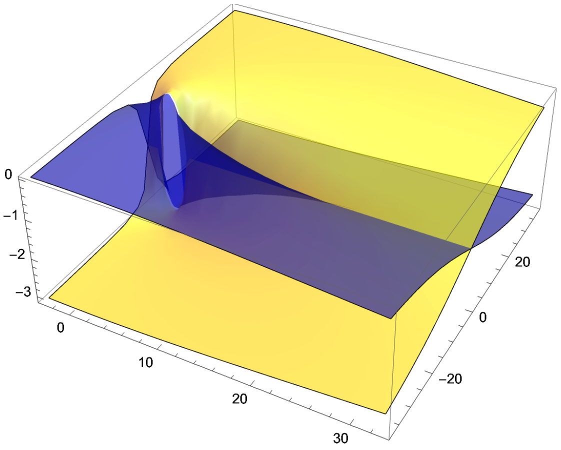

Bibliography

[1] Breuer, H. P. & Petruccione, F. *The theory of open quantum systems* (Oxford University Press, Great Clarendon Street, 2002).

[2] Lidar, D. A. Lecture Notes on the Theory of Open Quantum Systems (2019).

[3] Quantum Theory Of Radiation Interactions. *MIT Open Course* (2012).

[4] Qiskit contributors. Qiskit: An Open-source Framework for Quantum Computing (2023).

[5] Bender, C. M. & Boettcher, S. Real Spectra in Non-Hermitian Hamiltonians Having PT–Symmetry. *Physical Review Letters* **80**, 5243–5246 (1998).

[6] Guo, A. *et al.* Observation of $\mathcal{PT}$-Symmetry Breaking in Complex Optical Potentials. *Phys. Rev. Lett.* **103**, 093902 (2009).

[7] Rüter, C. E. *et al.* Observation of parity—time symmetry in optics. *Nature physics* **6**, 192 (2010).

[8] Peng, B. *et al.* Parity-time-symmetric whispering-gallery microcavities. *Nature Physics* **10**, 394–398 (2014).

[9] Hodaei, H., Miri, M.-A., Heinrich, M., Christodoulides, D. N. & Khajavikhan, M. Parity-time-symmetric microring lasers. *Science* **346**, 975–978 (2014).

[10] Zeuner, J. M. *et al.* Observation of a Topological Transition in the Bulk of a Non-Hermitian System. *Phys. Rev. Lett.* **115**, 040402 (2015).

[11] Li, J. *et al.* Observation of parity-time symmetry breaking transitions in a dissipative Floquet system of ultracold atoms. *Nature Communications* **10**, 855 (2019).

[12] Xiao, L. *et al.* Observation of topological edge states in parity-time-symmetric quantum walks. *Nature Physics* **13**, 1117–1123 (2017).

[13] Bender, C. M. *et al.* *PT Symmetry* (WORLD SCIENTIFIC (EUROPE), 2019).

[14] Regensburger, A. *et al.* Parity–time synthetic photonic lattices. *Nature* **488**, 167–171 (2012).

[15] Peng, B. *et al.* Parity-time-symmetric whispering-gallery microcavities. *Nature Physics* **10**, 394 EP – (2014). Article.

[16] Weimann, S. *et al.* Topologically protected bound states in photonic parity-time-symmetric crystals. *Nature Materials* **16**, 433 EP – (2016). Article.

[17] Feng, L., El-Ganainy, R. & Ge, L. Non-Hermitian photonics based on parity-time symmetry. *Nature Photonics* **11**, 752–762 (2017).

[18] El-Ganainy, R. *et al.* Non-Hermitian physics and PT symmetry. *Nature Physics* **14**, 11 EP – (2018). Review Article.

[19] Bender, C. M., Berntson, B. K., Parker, D. & Samuel, E. Observation of PT phase transition in a simple mechanical system. *American Journal of Physics* **81**, 173–179 (2013).

[20] Li, J. *et al.* Observation of parity-time symmetry breaking transitions in a dissipative Floquet system of ultracold atoms (2016). `arXiv:1608.05061`.

[21] Xu, H., Mason, D., Jiang, L. & Harris, J. G. E. Topological energy transfer in an optomechanical system with exceptional points. *Nature* **537**, 80–83 (2016).

[22] Dogra, S., Melnikov, A. A. & Paraoanu, G. S. Quantum simulation of parity–time symmetry breaking with a superconducting quantum processor. *Communications Physics* **4** (2021).

[23] Wu, Y. *et al.* Observation of parity-time symmetry breaking in a single-spin system. *Science* **364**, 878–880 (2019).

[24] Liu, W., Wu, Y., Duan, C.-K., Rong, X. & Du, J. Dynamically encircling an exceptional point in a real quantum system (2020). `arXiv:2002.06798`.

[25] Yu, S. *et al.* Experimental Investigation of Quantum $\mathcal{PT}$-Enhanced Sensor. *Phys. Rev. Lett.* **125**, 240506 (2020).

[26] Koch, J. *et al.* Charge-insensitive qubit design derived from the Cooper pair box. *Phys. Rev. A* **76**, 042319 (2007).

[27] Paik, H. *et al.* Observation of High Coherence in Josephson Junction Qubits Measured in a Three-Dimensional Circuit QED Architecture. *Phys. Rev. Lett.* **107**, 240501 (2011).

[28] Houck, A. A. *et al.* Controlling the Spontaneous Emission of a Superconducting Transmon Qubit. *Physical Review Letters* **101** (2008).

[29] Harrington, P. Measurement, Dissipation, and Quantum Control with Superconducting Circuits (2020).

[30] Harrington, P. M., Mueller, E. J. & Murch, K. W. Engineered dissipation for quantum information science. *Nature Reviews Physics* **4**, 660–671 (2022).

[31] Naghiloo, M. Introduction to Experimental Quantum Measurement with Superconducting Qubits (2019).

[32] Hatridge, M., Vijay, R., Slichter, D. H., Clarke, J. & Siddiqi, I. Dispersive magnetometry with a quantum limited SQUID parametric amplifier. *Phys. Rev. B* **83**, 134501 (2011).

[33] Castellanos-Beltran, M. A., Irwin, K. D., Hilton, G. C., Vale, L. R. & Lehnert, K. W. Amplification and squeezing of quantum noise with a tunable Josephson metamaterial. *Nature Physics* **4**, 929–931 (2008).

[34] Minganti, F., Miranowicz, A., Chhajlany, R. W. & Nori, F. Quantum exceptional points of non-Hermitian Hamiltonians and Liouvillians: The effects of quantum jumps. *Physical Review A* **100**, 062131 (2019).

[35] Naghiloo, M., Abbasi, M., Joglekar, Y. N. & Murch, K. W. Quantum state tomography across the exceptional point in a single dissipative qubit. *Nature Physics* **15**, 1232–1236 (2019).

[36] Mølmer, K., Castin, Y. & Dalibard, J. Monte Carlo wave-function method in quantum optics. *Journal of the Optical Society of America B* **10**, 524 (1993).

[37] Lau, H.-K. & Clerk, A. A. Fundamental limits and non-reciprocal approaches in non-Hermitian quantum sensing. *Nature Communications* **9**, 4320 (2018).

[38] Zhang, M. *et al.* Quantum Noise Theory of Exceptional Point Sensors (2018). `arXiv: 1805.12001`.

[39] Chen, C., Jin, L. & Liu, R.-B. Sensitivity of parameter estimation near the exceptional point of a non-Hermitian system (2018). `arXiv:1809.05719`.

[40] Abbasi, M., Chen, W., Naghiloo, M., Joglekar, Y. N. & Murch, K. W. Topological Quantum State Control through Exceptional-Point Proximity. *Physical Review Letters* **128** (2022).

[41] Chen, W., Abbasi, M., Joglekar, Y. N. & Murch, K. W. Quantum Jumps in the Non-Hermitian Dynamics of a Superconducting Qubit. *Physical Review Letters* **127** (2021).

[42] Chen, W. *et al.* Decoherence-Induced Exceptional Points in a Dissipative Superconducting Qubit. *Physical Review Letters* **128** (2022).

[43] Dembowski, C. *et al.* Experimental Observation of the Topological Structure of Exceptional Points. *Phys. Rev. Lett.* **86**, 787–790 (2001).

[44] Dembowski, C. *et al.* Encircling an exceptional point. *Physical Review E* **69**, 056216 (2004).

[45] Gao, T. *et al.* Observation of non-Hermitian degeneracies in a chaotic exciton-polariton billiard. *Nature* **526**, 554–558 (2015).

[46] Heiss, W. Phases of wave functions and level repulsion. *The European Physical Journal D - Atomic, Molecular and Optical Physics* **7**, 1–4 (1999).

[47] Mailybaev, A. A., Kirillov, O. N. & Seyranian, A. P. Geometric phase around exceptional points. *Physical Review A* **72**, 014104 (2005).

[48] Mehri-Dehnavi, H. & Mostafazadeh, A. Geometric phase for non-Hermitian Hamiltonians and its holonomy interpretation. *Journal of Mathematical Physics* **49**, 082105 (2008).

[49] Yao, S. & Wang, Z. Edge States and Topological Invariants of Non-Hermitian Systems. *Phys. Rev. Lett.* **121**, 086803 (2018).

[50] Kunst, F. K., Edvardsson, E., Budich, J. C. & Bergholtz, E. J. Biorthogonal Bulk-Boundary Correspondence in Non-Hermitian Systems. *Phys. Rev. Lett.* **121**, 026808 (2018).

[51] Patil, Y. S. S. *et al.* Measuring the knot of non-Hermitian degeneracies and non-commuting braids. *Nature* **607**, 271–275 (2022).

[52] Höller, J., Read, N. & Harris, J. G. E. Non-Hermitian adiabatic transport in spaces of exceptional points. *Physical Review A* **102** (2020).

[53] Gunderson, J., Muldoon, J., Murch, K. W. & Joglekar, Y. N. Floquet exceptional contours in Lindblad dynamics with time-periodic drive and dissipation. *Physical Review A* **103** (2021).

[54] Hatano, N. Exceptional points of the Lindblad operator of a two-level system. *Molecular Physics* **117**, 2121–2127 (2019).

[55] Minganti, F., Miranowicz, A., Chhajlany, R. W., Arkhipov, I. I. & Nori, F. Hybrid-Liouvillian formalism connecting exceptional points of non-Hermitian Hamiltonians and Liouvillians via postselection of quantum trajectories. *Phys. Rev. A* **101**, 062112 (2020).

[56] Arkhipov, I. I., Miranowicz, A., Minganti, F. & Nori, F. Quantum and semiclassical exceptional points of a linear system of coupled cavities with losses and gain within the Scully-Lamb laser theory. *Phys. Rev. A* **101**, 013812 (2020).

[57] Dalibard, J., Castin, Y. & Mølmer, K. Wave-function approach to dissipative processes in quantum optics. *Physical Review Letters* **68**, 580–583 (1992).

[58] Plenio, M. B. & Knight, P. L. The quantum-jump approach to dissipative dynamics in quantum optics. *Reviews of Modern Physics* **70**, 101 (1998).

[59] Gilmore, R. Catastrophe Theory (2007).

[60] Zhang, Z. *et al.* Measuring the Berry phase in a superconducting phase qubit by a shortcut to adiabaticity. *Physical Review A* **95** (2017).

[61] Ibáñez, S., Martínez-Garaot, S., Chen, X., Torrontegui, E. & Muga, J. G. Shortcuts to adiabaticity for non-Hermitian systems. *Physical Review A* **84** (2011).

[62] Höller, J., Read, N. & Harris, J. G. E. Non-Hermitian adiabatic transport in spaces of exceptional points. *Phys. Rev. A* **102**, 032216 (2020).

[63] Li, Z.-Z., Chen, W., Abbasi, M., Murch, K. W. & Whaley, K. B. Speeding up entanglement generation by proximity to higher-order exceptional points (2022).